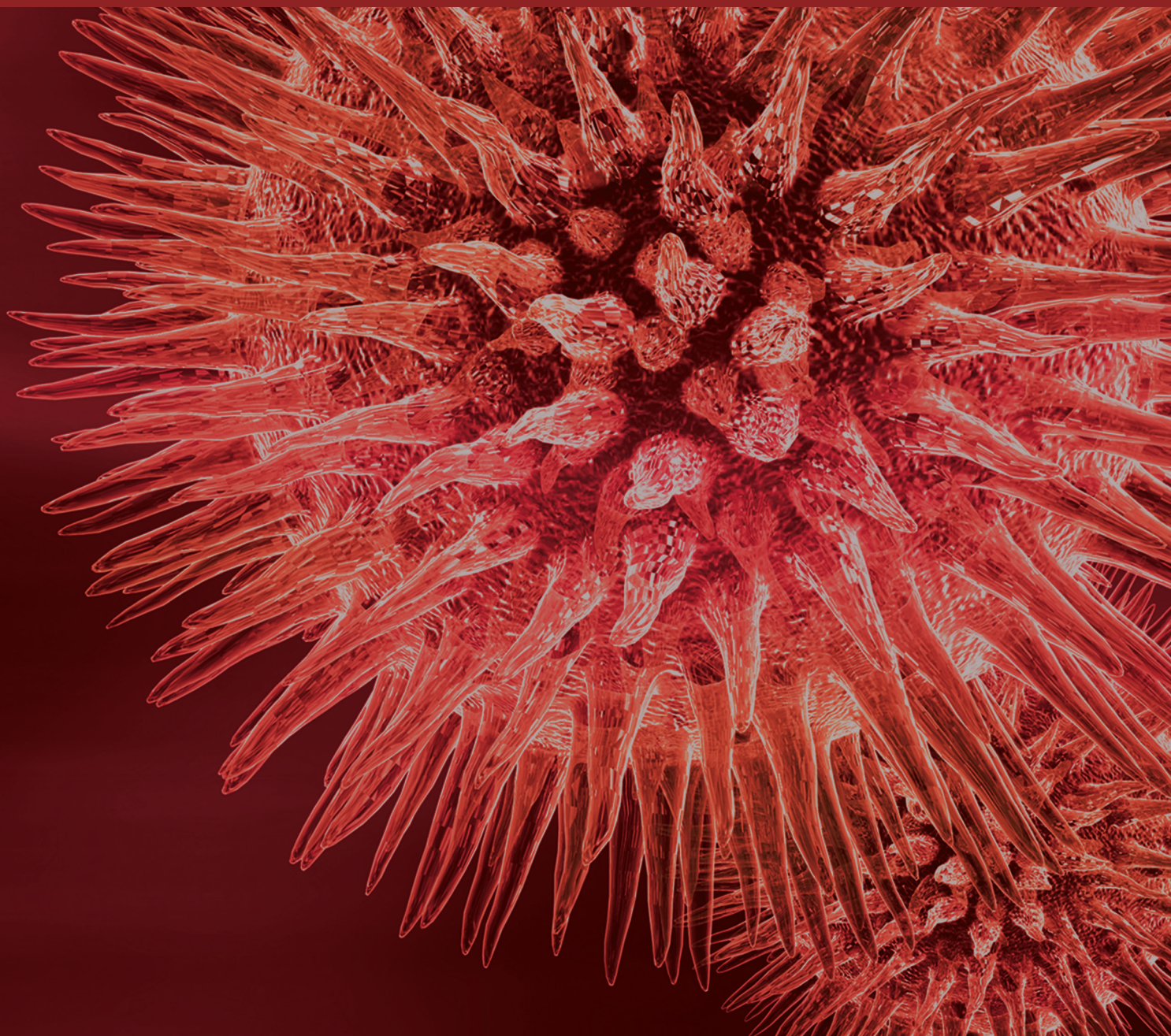


# Bone Tissue Engineering: Scaffolds with Osteoinductivity for Bone Regeneration

Guest Editors: Shen Liu, Changmin Hu, and Zheng Ren





---

# **Bone Tissue Engineering: Scaffolds with Osteoinductivity for Bone Regeneration**

BioMed Research International

---

# **Bone Tissue Engineering: Scaffolds with Osteoinductivity for Bone Regeneration**

Guest Editors: Shen Liu, Changmin Hu, and Zheng Ren



---

Copyright © 2017 Hindawi. All rights reserved.

This is a special issue published in “BioMed Research International.” All articles are open access articles distributed under the Creative Commons Attribution License, which permits unrestricted use, distribution, and reproduction in any medium, provided the original work is properly cited.

# Contents

---

**Bone Tissue Engineering: Scaffolds with Osteoinductivity for Bone Regeneration**

Shen Liu, Changmin Hu, and Zheng Ren  
Volume 2017, Article ID 1038476, 1 page

**Fabrication and Evaluation of Electrospun, 3D-Bioplotting, and Combination of Electrospun/3D-Bioplotting Scaffolds for Tissue Engineering Applications**

Liliana F. Mellor, Pedro Huebner, Shaobo Cai, Mahsa Mohiti-Asli, Michael A. Taylor, Jeffrey Spang, Rohan A. Shirwaiker, and Elizabeth G. Lobo  
Volume 2017, Article ID 6956794, 9 pages

**Management of Hepple Stage V Osteochondral Lesion of the Talus with a Platelet-Rich Plasma Scaffold**

Wenqi Gu, Tanzhu Li, Zhongmin Shi, Guohua Mei, Jianfeng Xue, Jian Zou, Xiaokang Wang, Haotong Zhang, and Hongwei Xu  
Volume 2017, Article ID 6525373, 6 pages

**Maxillary Sinus Augmentation with Decellularized Bovine Compact Particles: A Radiological, Clinical, and Histologic Report of 4 Cases**

Antonio Scarano  
Volume 2017, Article ID 2594670, 6 pages

**In Vitro Studies on the Degradability, Bioactivity, and Cell Differentiation of PRP/AZ31B Mg Alloys Composite Scaffold**

Jian Zou, Zhongmin Shi, Hongwei Xu, and Xiaolin Li  
Volume 2017, Article ID 5763173, 8 pages

**In Vitro and In Vivo Evaluation of Commercially Available Fibrin Gel as a Carrier of Alendronate for Bone Tissue Engineering**

Beom Su Kim, Feride Shkembi, and Jun Lee  
Volume 2017, Article ID 6434169, 10 pages

**Analysis of the Osteogenic Effects of Biomaterials Using Numerical Simulation**

Lan Wang, Jie Zhang, Wen Zhang, Hui-Lin Yang, and Zong-Ping Luo  
Volume 2017, Article ID 6981586, 7 pages

**Periosteal Distraction Osteogenesis: An Effective Method for Bone Regeneration**

Danyang Zhao, Yu Wang, and Dong Han  
Volume 2016, Article ID 2075317, 10 pages

## Editorial

# Bone Tissue Engineering: Scaffolds with Osteoinductivity for Bone Regeneration

Shen Liu,<sup>1</sup> Changmin Hu,<sup>2</sup> and Zheng Ren<sup>2</sup>

<sup>1</sup>Department of Orthopedics, Shanghai Jiao Tong University Affiliated Sixth People's Hospital, Shanghai, China

<sup>2</sup>Institute of Materials Science, University of Connecticut, Connecticut, USA

Correspondence should be addressed to Shen Liu; liushensjtu@126.com

Received 10 April 2017; Accepted 10 April 2017; Published 2 May 2017

Copyright © 2017 Shen Liu et al. This is an open access article distributed under the Creative Commons Attribution License, which permits unrestricted use, distribution, and reproduction in any medium, provided the original work is properly cited.

Biological mechanism of bone repair mainly involves both osteoconductivity and osteoinductivity. Scaffolds with osteoinductivity can give biological signals to stimulate the proliferation and differentiation of bone marrow mesenchymal stem cells and osteoblast-like cells to promote bone regeneration. Although most scaffolds for bone tissue engineering demonstrate osteoconductivity, they lack osteoinductivity to stimulate cell differentiation and bone regeneration, which impedes their wide applications. Our initial aim was to illustrate the continuing efforts of scaffolds with osteoinductivity for bone regeneration.

PRP is considered as a bioactivator of growth factors and has been used as bone and tissue biomaterials in two papers. It is reported by Dr. J. Zou and coworkers that PRP can promote the rat mesenchymal stem cells attachment, proliferation, and differentiation on the surface of Mg alloys with higher expression of OPN and OCN. According to the study of W. Gu et al., PRP combined with cancellous bone graft can successfully promote the complete regeneration of subchondral bone and cartilage with improved clinical scores in 13 patients suffered from the osteochondral lesion of the talus.

A clinical histomorphometrical evaluation of Re-Bone® after 6 months from sinuses has been conducted by A. Scarano, and he reported that newly formed bone was about  $36 \pm 1.6\%$ .

L. Wang and coworkers described an optimal algorithm for determining the effects of implanted biomaterials on bone growth with crucial insights into the development of implanted biomaterials for both clinical medicine and materials science.

Dr. L. Mellor and his team fabricated 3D printed/electrospun scaffold architectures to mimic the native architecture of heterogenous tissue. This scaffold can mimic physiological thickness of different tissues but also resembled the diverse framework of ECM with great potential for tissue engineering and regenerative medicine applications.

Alendronate-loaded fibrin gel was reported by B. S. Kim et al. to promote the osteogenic differentiation of mesenchymal stem cells and improve in vivo new bone regeneration with biological signals.

An interesting review of periosteal distraction osteogenesis (PDO) related to the osteogenicity of periosteum has been conducted by D. Zhao et al. This review elucidates the availability of PDO in the aspects of mechanisms, devices, strategies, and measures as well as the future prospects of PDO.

All seven papers have shown the interest of the investigators of various aspects of continuing efforts to provide osteoinductivity for bone regeneration using novel architecture of scaffolds, biomaterials, and techniques. With the advances in topics of the osteoinductivity for bone regeneration, potential application will be combined to the experimental research and the clinical treatment of bone defects in bone tissue engineering.

Shen Liu  
Changmin Hu  
Zheng Ren

## Research Article

# Fabrication and Evaluation of Electrospun, 3D-Bioplotting, and Combination of Electrospun/3D-Bioplotting Scaffolds for Tissue Engineering Applications

Liliana F. Mellor,<sup>1</sup> Pedro Huebner,<sup>2</sup> Shaobo Cai,<sup>1</sup> Mahsa Mohiti-Asli,<sup>1</sup> Michael A. Taylor,<sup>1</sup> Jeffrey Spang,<sup>3</sup> Rohan A. Shirwaiker,<sup>1,2</sup> and Elizabeth G. Lobo<sup>4</sup>

<sup>1</sup>Joint Department of Biomedical Engineering, University of North Carolina at Chapel Hill and North Carolina State University, Raleigh, NC 27695, USA

<sup>2</sup>Edward P. Fitts Department of Industrial and Systems Engineering, North Carolina State University, Raleigh, NC 27695, USA

<sup>3</sup>Department of Orthopaedics, University of North Carolina School of Medicine, Chapel Hill, NC 27599, USA

<sup>4</sup>College of Engineering, University of Missouri, W1051 Thomas & Nell Lafferre Hall, Columbia, MO 65211, USA

Correspondence should be addressed to Rohan A. Shirwaiker; [rashirwaiker@ncsu.edu](mailto:rashirwaiker@ncsu.edu) and Elizabeth G. Lobo; [egloboa@missouri.edu](mailto:egloboa@missouri.edu)

Received 6 December 2016; Revised 20 March 2017; Accepted 2 April 2017; Published 27 April 2017

Academic Editor: Changmin Hu

Copyright © 2017 Liliana F. Mellor et al. This is an open access article distributed under the Creative Commons Attribution License, which permits unrestricted use, distribution, and reproduction in any medium, provided the original work is properly cited.

Electrospun scaffolds provide a dense framework of nanofibers with pore sizes and fiber diameters that closely resemble the architecture of native extracellular matrix. However, it generates limited three-dimensional structures of relevant physiological thicknesses. 3D printing allows digitally controlled fabrication of three-dimensional single/multimaterial constructs with precisely ordered fiber and pore architecture in a single build. However, this approach generally lacks the ability to achieve submicron resolution features to mimic native tissue. The goal of this study was to fabricate and evaluate 3D printed, electrospun, and combination of 3D printed/electrospun scaffolds to mimic the native architecture of heterogeneous tissue. We assessed their ability to support viability and proliferation of human adipose derived stem cells (hASC). Cells had increased proliferation and high viability over 21 days on all scaffolds. We further tested implantation of stacked-electrospun scaffold versus combined electrospun/3D scaffold on a cadaveric pig knee model and found that stacked-electrospun scaffold easily delaminated during implantation while the combined scaffold was easier to implant. Our approach combining these two commonly used scaffold fabrication technologies allows for the creation of a scaffold with more close resemblance to heterogeneous tissue architecture, holding great potential for tissue engineering and regenerative medicine applications of osteochondral tissue and other heterogeneous tissues.

## 1. Introduction

Tissue engineering is a growing field that aims to create living biological substitutes to restore, repair, or regenerate native tissue or organ function that may be affected by disease or injury. The main components of engineered tissues include cells, scaffolds, and chemical and/or mechanical cues to replicate or mimic the physiological conditions of the target tissue [1]. The individual characteristics of each of these components and their interactions have a significant impact on the quality and functionality of engineered tissues [2]. As

such, it is important to determine the optimum combination of relevant characteristics for any target tissue to be engineered.

The most commonly used strategies in tissue engineering involve seeding a uniform or homogenous scaffold with a single cell type. But, in reality, most tissues are composed of several cell types and a diverse and heterogenic extracellular matrix (ECM) framework [3, 4]. Failure to replicate the physiological and native conditions can have negative results in engineered tissue integration and function when implanted in an organism [1, 5]. Scaffold design in tissue engineering

is particularly important, as the scaffold should not only provide an optimal 3D network to support cell adhesion and proliferation but also appropriately guide cell differentiation, when stem cells are used, to generate the desired tissue(s) [6, 7]. Osteochondral tissue engineering has proven to be very complex due to the presence of different cell types, ECM heterogeneity, and the multiple three-dimensional materials which characterize an articular joint including the following: porous subchondral bone, a transitional dense cartilage framework, and a tidemark separating the layers [4, 8]. Most scaffold fabrication techniques cannot recapitulate the heterogeneous multiphasic porous architecture that is native to an articular joint.

The goal of this study was to combine two commonly used fabrication techniques—electrospinning and 3D printing—to develop a simple and reproducible scaffold that incorporates both nano- and microscale fibrous architecture and more closely mimic heterogeneous tissues. We evaluated a combined 3D printed/electrospun scaffold architecture mimicking heterogeneous tissues such as the osteochondral complex, in comparison to solely 3D printed microfibrillar or solely electrospun nanofibrous scaffolds, for their ability to support viability and proliferation of human adipose-derived stem cells (hASC). Further, we also tested and compared the feasibility and efficacy of implanting full-thickness (6 mm) combined 3D printed/electrospun versus stacked electrospun scaffolds in an ex vivo porcine model using a clinically relevant procedure for osteochondral defect repair. The results show the ability to successfully engineer a scaffold that resembles the physiological thickness as well as a multiscale heterogeneous fibrous architecture of osteochondral tissue. This combined 3D printing/electrospinning approach could be extended to other tissues with heterogeneous ECM framework and/or transitional tissues like ligament and tendon bone insertions in the future.

## 2. Materials and Methods

**2.1. 3D-Bioplotting Microfibrillar Scaffolds.** Thin disc-shaped scaffolds ( $\varnothing$  14.5 mm  $\times$  2 mm) (Figure 1(a)) were fabricated using polycaprolactone (PCL,  $M_w = 80$  K, Sigma-Aldrich Co., St. Louis, MO) on a 3D-Bioplotter (4th-Generation Developer Series, EnvisionTEC GmbH, Gladbeck, Germany). The scaffolds and their CAD model (Solidworks 2014) were designed to facilitate the fitting and culturing of finished constructs in standard 24-well cell culture plates. Previously determined optimal bioplotting process parameters were used [9–11]. In brief, PCL was extruded at an extrusion pressure of 0.5 N/mm<sup>2</sup> and extrusion temperature of 180°C through a 0.4 mm inner diameter nozzle with a printing speed of 0.4 mm/s following a 45-minute preheat interval for stabilization and air removal from the melt. The scaffold design featured a separation of 1.5 mm between the axes of adjacent strands, which kept constant through all the layers, and a strand lay-down pattern of 0°/120°/240° between adjacent layers, yielding a highly interconnected pore network.

**2.2. Electrospinning Nanofibrous Scaffolds.** PCL was dissolved in chloroform and dimethylformamide (Sigma) at a ratio of 3:1 to create an 11% solution. The solution was mixed continuously at 80°C for at least 4 hours. The PCL solution was electrospun using an internal nozzle diameter of 0.508 mm on a static collector covered with aluminum for 3 hours immediately after preparation at a feed rate of 0.7  $\mu$ L/hr and spinning distance of 13–15 cm using 15 kV. The electrospun nanofibrous scaffolds were detached from the aluminum surface prior to being used.

Stacked scaffolds (6 mm thick) used for implantation were generated by stacking together multiple electrospun layers using collagen type I gel in between the layers, at a concentration of 3 mg/mL (Vitrogen, Angiotech BioMaterials Corporation, Palo Alto, CA) [12]. Collagen was first neutralized to pH 7.0, pipetted between the layers, and allowed to polymerize for 2 hours at 37°C.

**2.3. Combined 3D-Bioplotting Microfibrillar/Electrospun Nanofibrous Scaffolds.** The integrated micro- and nanofibrous PCL scaffolds were fabricated using a combination of 3D-bioplotting and electrospinning. The electrospun layers were cut into 14.5 mm diameter circles to match the size of the 3D scaffolds. First, a 2 mm basal section of 3D-bioplotting scaffold was printed as mentioned above. We then placed the circular electrospun layer directly over the basal layer and continued printing another 2 mm section on top of the electrospun layer to generate a final 4 mm thick scaffold with an electrospun layer in the middle (Figure 1). These scaffolds were used for testing hASC viability and proliferation. The full thickness (6 mm) scaffolds evaluated for implantation techniques were fabricated using the same procedure but with 4 mm basal section and 2 mm top section 3D bioplotting.

**2.4. Isolation and Expansion of Human Adipose-Derived Stem Cells.** Excess adipose tissue was collected from five female premenopausal donors (ages 24 to 36) in accordance with an approved IRB protocol at UNC Chapel Hill (IRB 04-1622) [13]. Human ASC were isolated from the tissue as previously described by our lab and others [14–16]. Cells were expanded in complete growth medium (CGM) comprised of  $\alpha$ -modified minimal essential medium ( $\alpha$ -MEM with L-glutamine) (Invitrogen, Carlsbad CA), 10% fetal bovine serum (FBS) (Premium Select, Atlanta Biologicals, Lawrenceville GA), 200 mM L-glutamine, and 100 I.U. penicillin/100  $\mu$ g/mL streptomycin (Mediatech, Herndon VA). The cells were cultured at 37°C in 5% CO<sub>2</sub> until reaching 80% confluency and then passaged using trypsin-EDTA (Invitrogen). A superlot was generated by pooling equal numbers of cells from the five individual donor cell lines into a single culture vessel and characterized for multilineage differentiation potential, ensuring the cells differentiated representative of an average of the five cell lines [13].

**2.5. Seeding of Scaffolds.** The 3D-bioplotting, electrospun, and combined bioplotting/electrospun disc scaffolds ( $\varnothing$  14.5 mm) were designed and fabricated to fit in 24-well plates (well  $\varnothing$  15.6 mm), limiting any space between the walls of the well

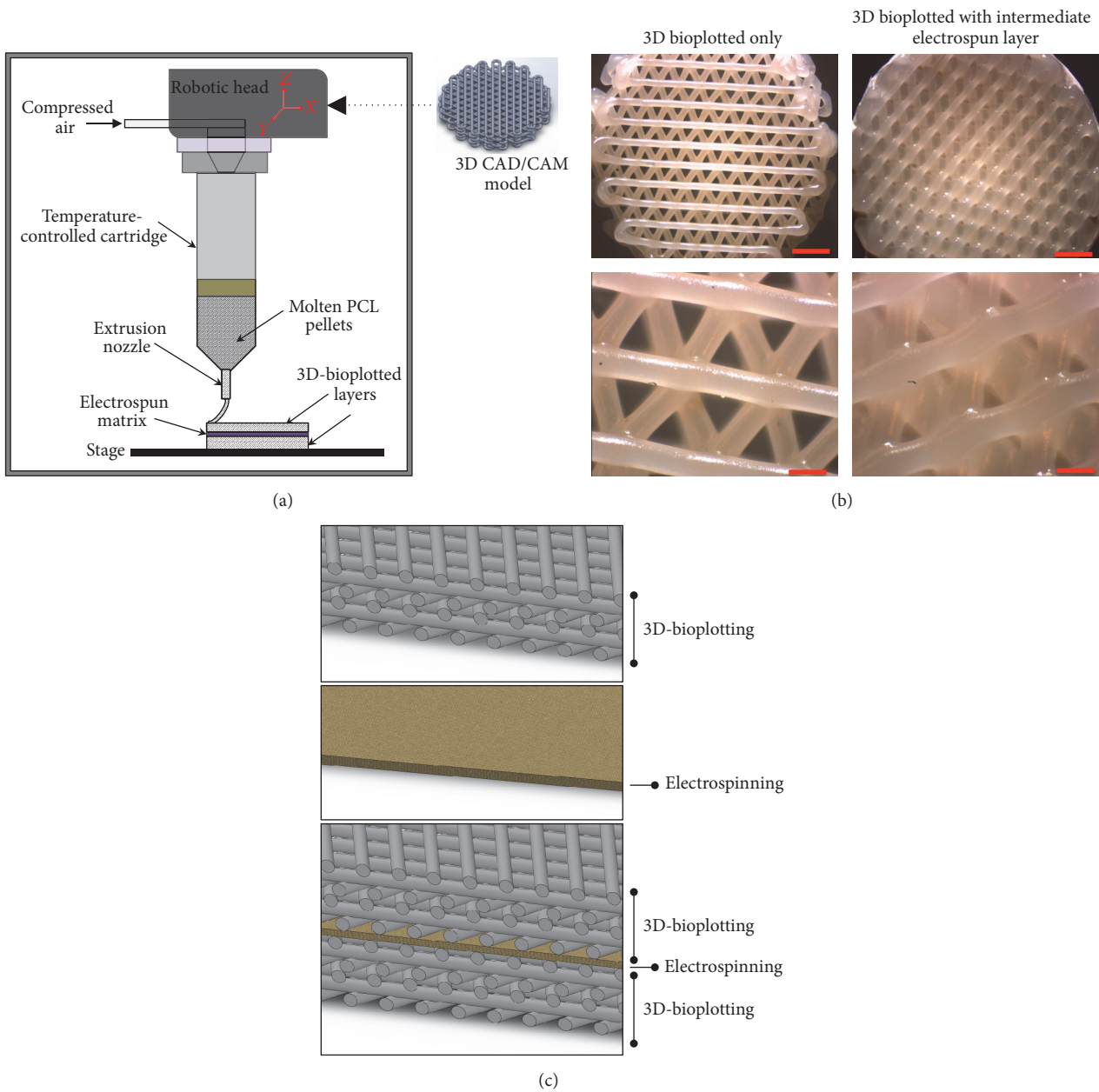


FIGURE 1: Fabrication of combined micro- and nanofibrous scaffold by sandwiching an electrospun layer between 3D-bioplotted layers. (a) Schematic of technical approach. (b) 3D-bioplotted scaffold with and without an electrospun layer (scale bars top = 2 mm; bottom = 500  $\mu\text{m}$ ). (c) Cross-sectional CAD representation of three different scaffolds created and evaluated. Top: microfibrinous scaffold fabricated using 3D bioplotting technique only. Middle: nanofibrinous scaffold fabricated using electrospinning only. Bottom: alternating micro- and nanosized fibers by combining 3D bioplotting and electrospinning techniques. Colors and textures for visualization purposes only.

and the periphery of the scaffold where cells could potentially migrate towards the bottom of the wells. Prior to seeding, scaffolds were sterilized for 30 minutes in 70% ethanol, rinsed three times with sterile phosphate buffered saline (PBS) and once with CGM. Due to the difference in thickness between the scaffold designs (electrospun = 200  $\mu\text{m}$ , 3D-bioplotted = 2 mm, and combined scaffolds = 4.2 mm.), a total of 100,000 cells were seeded in each 3D scaffold and 20,000 cells in each

electrospun scaffold over a two-day period. On the first day, half of the total amount of cells (50,000 cells for 3D scaffolds and 10,000 cells for electrospun scaffolds) were resuspended in 1 mL of CGM and added to each well containing a scaffold. The cells/scaffolds were incubated overnight while gently rocking to allow cell distribution and adhesion throughout the scaffolds. On the second day, each scaffold was overturned and seeded with the remaining cells to allow adhesion of cells

on both sides of the scaffolds. Once again, the scaffolds were incubated overnight while gently rocking. The scaffolds were then transferred to a new well for performance of all assays.

**2.6. Cell Viability Analyses.** Seeded scaffolds were cultured in CGM for 21 days to promote growth and proliferation. After 21 days of culture, a LIVE/DEAD viability assay (Life Technologies) was performed per the manufacturer's instructions on all scaffolds to assess hASC viability within the scaffolds. Briefly, hASC-seeded scaffolds were gently washed with sterile PBS three times, and then 500  $\mu\text{L}$  of 2  $\mu\text{M}$  calcein AM and 4  $\mu\text{M}$  EthD-1 solution was added to each scaffold and incubated for 30 minutes. Scaffolds were visualized using a Leica DM5500B Fluorescent Microscope and the compatible LAS-AF software. Two consecutive images per section were taken to visualize live cells (green) and dead cells (red), and a composite overlaid image was generated to visualize both channels in the same frame. To optimize exposure, gain, and intensity parameters, the LUT function of the software was used. All images were taken at 10x magnification.

**2.7. Cell Proliferation Analyses.** Cell proliferation was assessed ( $n = 4$  scaffolds per time point) at days 1, 4, 7, 11, and 20 after seeding using the AlamarBlue colorimetric assay (Life Technologies). Acellular scaffolds were also analyzed as controls, and all data was normalized to the appropriate acellular control scaffold. At each time point, a 1:10 ratio of AlamarBlue:CGM solution was added to each scaffold and incubated at 37°C and 5%  $\text{CO}_2$  for 3 hours. After incubation, absorbance was measured at wavelengths of 570 nm and 600 nm using a Microplate reader (Tecan Group Ltd., Männedorf, Switzerland) and the Magellan Data Analysis Software (Tecan Group Ltd.).

**2.8. Implantation of Scaffolds in a Porcine Model.** Cadaveric porcine knees were utilized to create a suitable ex vivo environment in a large animal model that resembles the human knee. This model has been used extensively in vivo to evaluate articular cartilage repair techniques [17, 18]. Using current human surgical techniques and currently utilized hardware (COR Osteochondral Autograft Transfer System, DePuy Mitek, Raynham, MA), stacked electrospun scaffolds and a single 3D-bioplotting scaffold were implanted into osteochondral defects created via drilling to evaluate scaffold-handling characteristics in the surgical setting. Osteochondral Autograft Transfer techniques commonly employed for human patients were utilized [19–21]. Briefly, a power reamer was used to create an osteochondral defect to a depth of 8 mm with an 8 mm diameter. Using the donor cutting tool from the COR system, an 8 mm diameter section of the osteochondral stacked scaffold was cut from a 14.5 mm diameter scaffold (typical size created using our approach). The scaffold was then implanted into the recipient hole per the recommended COR Osteochondral Autograft Transfer System technique (DePuy Mitek, Raynham, MA), consistent with current human surgical procedures. Optimal scaffold depth was selected based on the handling ability of the

scaffold and successful implantation of the scaffolds to fill the created defect.

**2.9. Statistical Analysis.** Statistical analysis was performed using Prism (version 6.07, GraphPad Software). Bar graphs are represented as mean  $\pm$  SEM. Differences were determined using a one-way ANOVA with Tukey post hoc test. A level of  $p < 0.05$  was considered significant.

### 3. Results

**3.1. Cell Viability, Migration, and Proliferation in Scaffolds.** Scanning electron microscopy (SEM) images show the different fiber size and arrangement between 3D-bioplotting and electrospun scaffolds (Figures 2(a) and 2(b)), as well as the combined nano/microfibrous scaffold (Figure 2(c)). Cells can also be observed on the surface of all three seeded scaffolds (Figures 2(d)–2(f)).

To ensure cells could grow and proliferate throughout individual nano- and microfibrous scaffolds, we first measured and compared hASC proliferation and viability after 21 days in culture in both electrospun and 3D-bioplotting scaffolds. Cells were able to adhere and proliferate in both micro- and nanofibrous scaffolds, with minimal dead cells observed after 21 days in culture. However, the hASC exhibited higher proliferation and more uniform spreading in electrospun scaffolds when compared to 3D-bioplotting scaffolds (Figure 3).

We then compared cell proliferation and migration in all three scaffolds (Figure 4). Cells were visible on the superficial layers of all three scaffolds (Figure 4(a)) and throughout the scaffolds (Figure 4(b)). Cells seeded on 3D scaffolds only had significantly increased proliferation after 14 days in culture, with a decrease at day 21. Electrospun scaffolds had significant increase in proliferation after 14 days in culture, and the combined scaffold had a steady proliferation without a decline over the 21-day culture period (Figure 4(c)).

**3.2. Comparison of Implantation of Micro- and Nanofibrous Scaffolds in a Porcine Ex Vivo Model.** Standard human operative techniques were used to implant both stacked nanofibrous scaffolds and combination of 3D-bioplotting/electrospun scaffolds into a cadaveric porcine knee model, to determine the translational applicability of these scaffolds in a relevant in vivo model for osteochondral tissue engineering. Due to the limited thickness of each electrospun layer (approximately 200  $\mu\text{m}$ ), 30 different electrospun layers (each  $\varnothing$  14.5 mm) were stacked using collagen I in between each layer as previously described [22], to create a 6 mm thick scaffold. A 3D-bioplotting/electrospun scaffold (6 mm thick; 14.5 mm diameter) was also fabricated for implantation into an osteochondral defect and to compare to the implantation technique of the electrospun stacked scaffold. The COR Osteochondral Autograft Transfer System technique was compatible for sizing and implanting both stacked electrospun and 3D-bioplotting scaffolds. However, we found that stacked electrospun scaffolds easily delaminated when using the plug harvest system and needed to be frozen prior to implantation to prevent delamination. The 3D-bioplotting

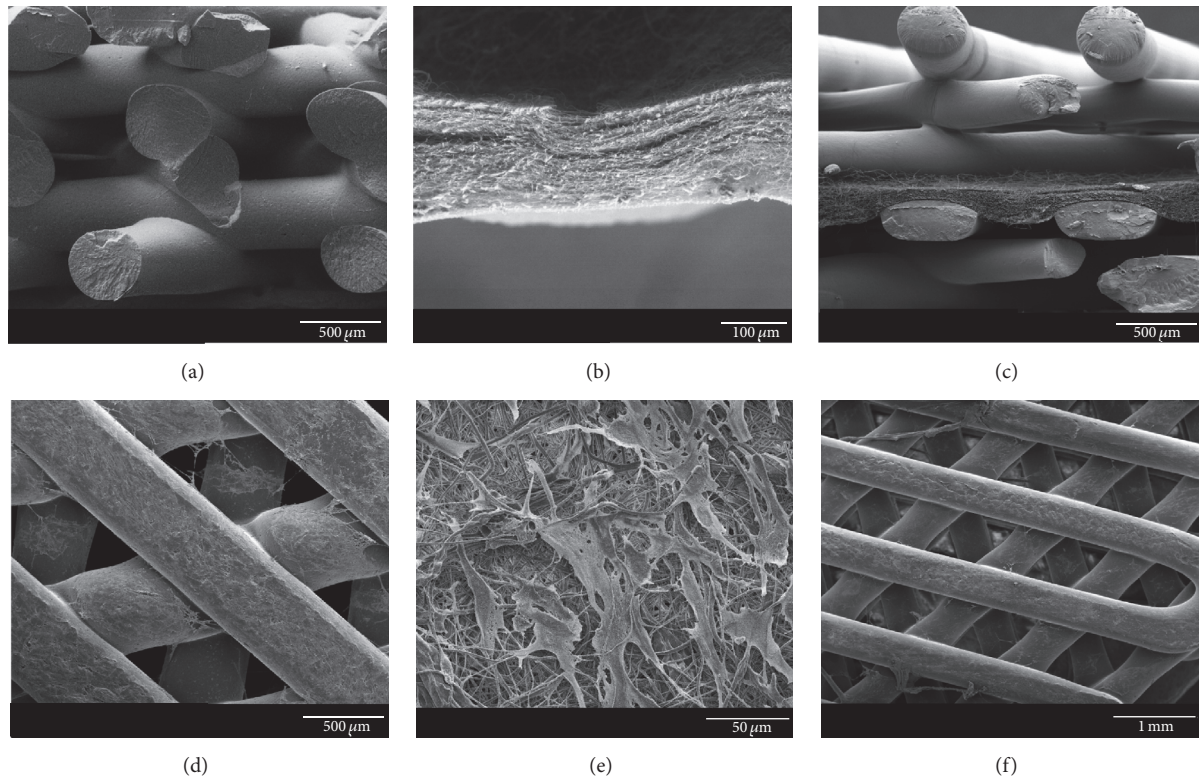


FIGURE 2: Scanning electron microscopy of (a) 3D-bioplotted scaffold; (b) electrospun nanofibers; (c) combined 3D-bioplotted and electrospun scaffolds (electrospun layer in middle); (d) cells growing on 3D-bioplotted scaffold; (e) cells growing on electrospun nanofibers; and (f) cells growing on combined 3D and electrospun scaffold (scale bars (a), (c), (d) = 500  $\mu\text{m}$ ; (b) = 100  $\mu\text{m}$ ; (e) = 50  $\mu\text{m}$ ; (f) = 1 mm).

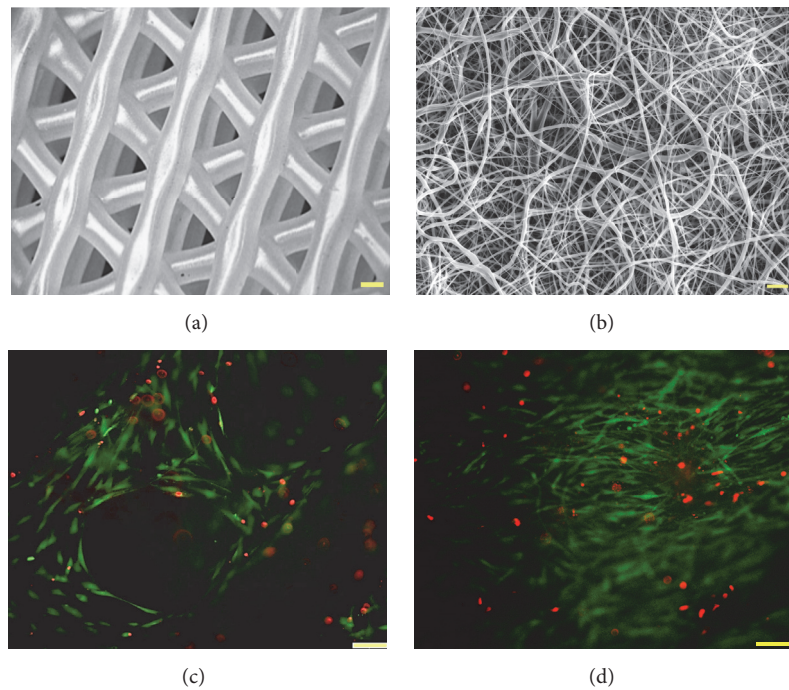


FIGURE 3: Cell viability and proliferation of human adipose-derived stem cells seeded on (a, c) 3D-bioplotted scaffolds and (b, d) electrospun scaffolds (green = live cells; red = dead cells).

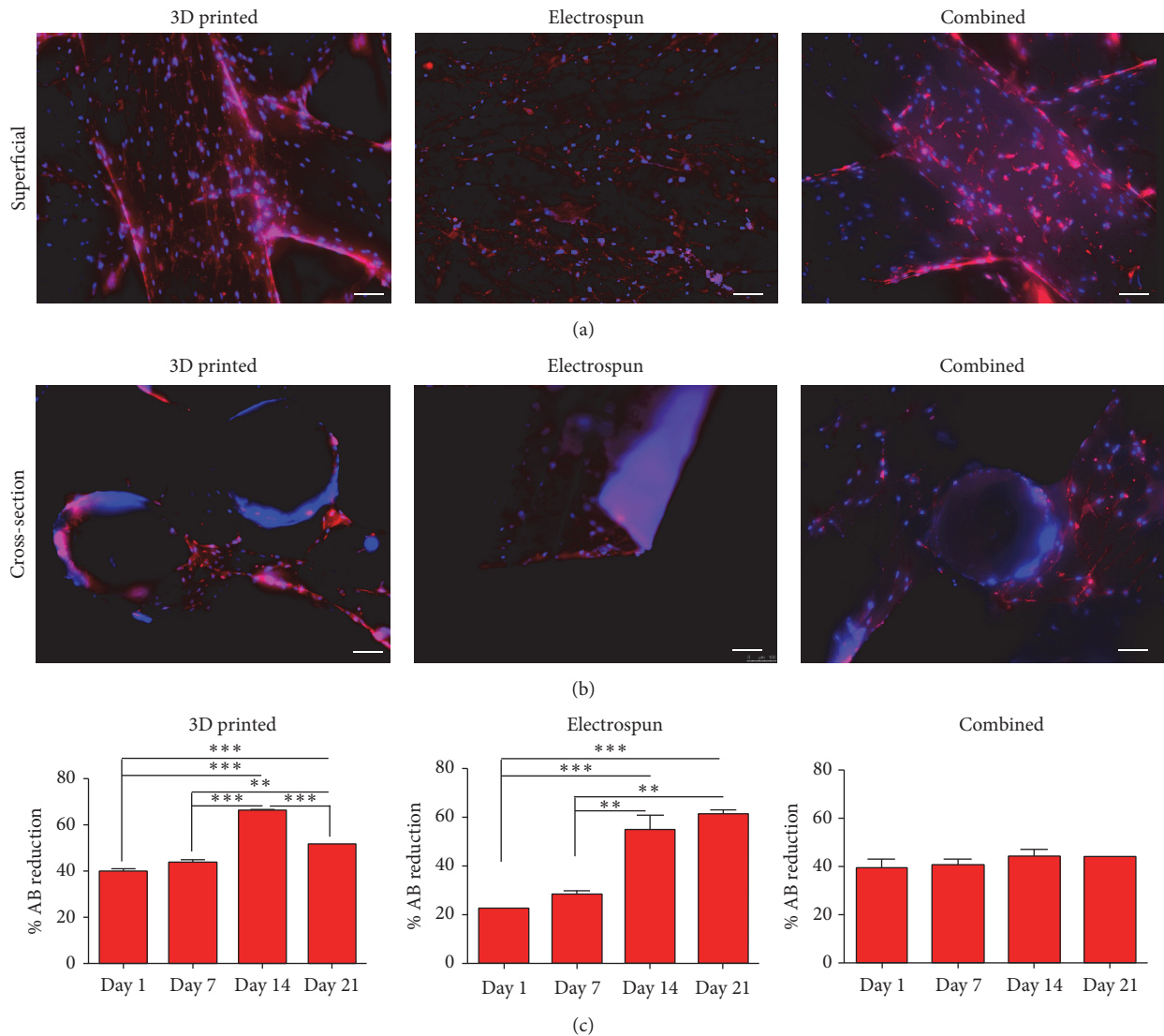


FIGURE 4: Cell spreading and proliferation of human adipose-derived stem cells throughout scaffolds. Cells were cultured for 21 days in 3D-bioplotting, electrospun, or combination of 3D-bioplotting/electrospun scaffolds, fixed, and stained (actin = red; nuclei = blue). Superficial and cross-sectional views show cells present both on the surfaces of the scaffolds (superficial) and throughout the centers of the scaffolds (cross-section). Human ASC exhibited steady proliferation over 21 days of culture on all scaffold types as indicated by AlamarBlue (% AB reduction). Bars indicate mean  $\pm$  SEM (\*\* $p < 0.005$ ; \*\*\* $p < 0.0001$ ).

scaffolds and the combined 3D-bioplotting/electrospun scaffolds were easily inserted using the COR system and successfully implanted into the cadaveric porcine knee without delamination (Figure 5).

#### 4. Discussion

Electrospinning is a commonly used technique in tissue engineering allowing for production of a dense framework of fibers with pore sizes and fiber diameters that closely resemble the architecture of native ECM [23–25]. However, this technique has limitations in generating three-dimensional structures of relevant physiological thicknesses. 3D-printing processes such as 3D-bioplotting have emerged in the last

decade as alternative techniques to generate scaffolds of physiologically relevant thicknesses and morphologies that are biomimetic to different tissues and organs [5, 26]. Although these techniques have better three-dimensional geometrical flexibility, they are limited to generation of microsized fibers and larger pore sizes than those of electrospun scaffolds. Our goal here was to develop a methodology to create a multiscale scaffold design using a combination of electrospinning and 3D-bioplotting in order to better match the architecture of heterogeneous tissue, using osteochondral tissue as a sample model.

Previous investigators have also attempted to combine micro- and nanofibrous architecture into a single scaffold for different tissue engineering applications. For example,

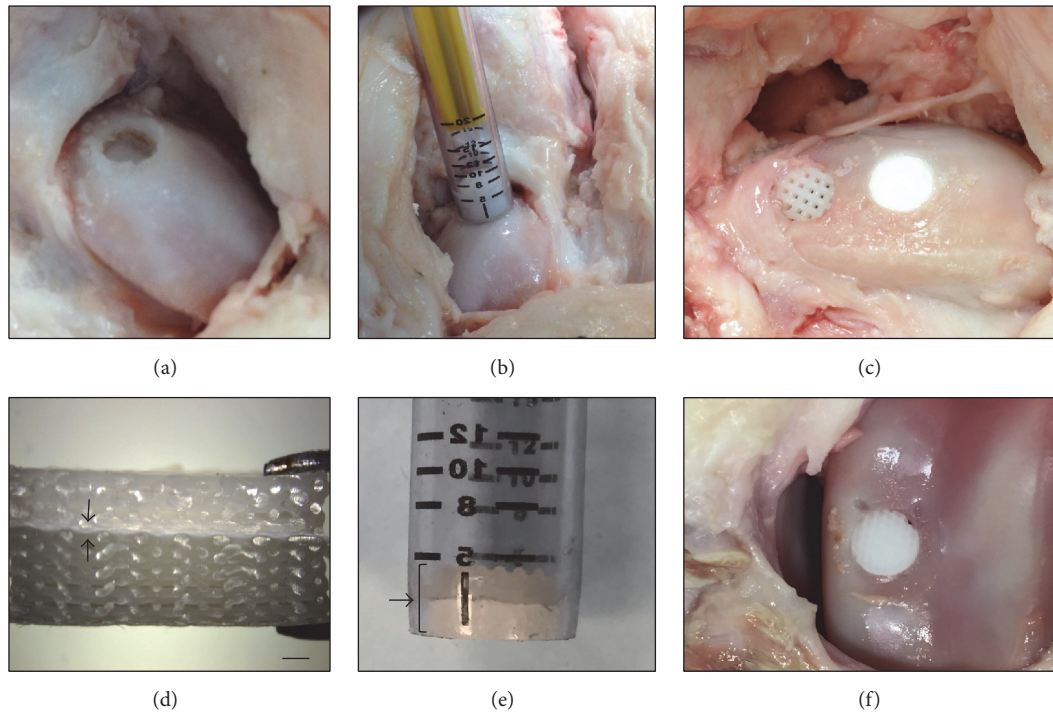


FIGURE 5: Implantation technique of 3D-bioplotted, electrospun, and combined 3D-bioplotted/electrospun scaffolds into a cadaveric porcine knee. (a) A power reamer was used to create an osteochondral defect to a depth of 8 mm and 8 mm diameter. (b) The COR system was used to implant the scaffolds into the osteochondral defect. (c) View of 3D-bioplotted scaffold (left) and electrospun scaffold (right) after implantation. (d) Combined 3D-bioplotted/electrospun scaffold prior to implantation (black arrows indicate electrospun layer, scale bar = 1 mm). (e) Combined 3D-bioplotted/electrospun scaffold inserted into the COR system for implantation (bracket and arrow pointing at scaffold inside the device). (f) Combined 3D-bioplotted/electrospun scaffold after implantation.

Yeo and Kim created cell-laden hierarchical scaffolds that incorporated microsized fibers for support, combined with electrospun nanofibers to enhance cell proliferation and distribution [27]. Their approach incorporated cell-laden alginate struts of osteoblast-like cells (MG63) to obtain homogenous cell distribution within the scaffold. Although they successfully achieved homogenous cell proliferation throughout the scaffold, their complex fabrication procedure required repetition of three different techniques including melt-dispensing, followed by electrospinning, and cell-dispensing in order to obtain cell-laden alginate struts. Their goal was to create a homogenous tissue with even cell distribution that could be used as a promising scaffold for regeneration of soft and hard tissue, but not necessarily a heterogenous tissue.

In this study, we present a facile and reproducible technique to develop an integrated approach combining both electrospun nanofibers and 3D-plotted microfibers to recapitulate the heterogenous architecture of native tissue. In the first approach, we electrospun nanofibers over a 3D-bioplotted scaffold. Although we successfully coated the 3D-bioplotted scaffold with electrospun nanofibers, the two layers delaminated during culture of the combined micro/nanofibrous scaffold in cell culture medium (data not shown). Such delamination would likely be a greater problem *in vivo*; therefore we believe this technique is not appropriate for generating a combined nano/microfibrous scaffold.

We therefore evaluated an alternative approach by 3D-bioplotting directly on an electrospun scaffold. An electrospun nanofibrous layer was placed directly over a freshly printed 3D scaffold, and then another 3D scaffold was printed on top of this electrospun layer (Figure 1(a)). This combined micro/nanofibrous scaffold did not delaminate during culture. It is possible that the heat from the printed microfibers facilitated binding of the nanofibers to the printed microfibers; however, as observed in the SEM images of the combined scaffold (Figure 2(c)), the heat did not seem to impact the fiber morphology. Increased thickness can be achieved by continued layering of the materials, alternating between electrospun nanofibers and 3D-bioplotted microfibers, to create a multilayered micro/nanofibrous scaffold as needed. Based on our findings, the best approach to fabricate a combined micro/nanofibrous scaffold was to 3D print over electrospun layers. This combined technique produced single scaffolds that more closely resembled the native heterogenous architecture.

Cell proliferation was significantly increased over time in both 3D-bioplotted and electrospun scaffolds. Although proliferation did not significantly increase over time in the combined scaffolds, we still observed a steady proliferation with no decline over time. Although cell proliferation and viability were higher in the electrospun scaffolds, this technique has thickness and 3-dimensional limitations, typically resulting in creation of a ~200-micron scaffold after hours of

electrospinning using conventional electrospinning systems. In addition, stacking several electrospun layers to create a thicker scaffold not only is time consuming but can also limit the migration of cells throughout the layers (data not shown). We first tested hASC cell viability and migration throughout micro- and nanofibers by seeding cells on scaffolds with either the electrospun layer on top or underneath the 3D-bioplotted layer. We observed that when cells were seeded on the 3D-bioplotted scaffold, the cells proliferated and migrated down to the electrospun layer. However, if the cells were seeded over the electrospun layer, the nanofiber acted as a barrier and prevented cells from migrating down into the 3D-bioplotted layer.

With our technique, the electrospun membrane can be used to separate layers that require different cell types in heterogenous tissues, like bone and cartilage in osteochondral tissue. This way, the chondrocytes, for instance, will not migrate into the underlying subchondral bone layer or vice versa, while providing a natural framework that resembles the tight collagen network in that area.

Ex vivo handling of 3D-bioplotted, stacked electrospun, and combined 3D-bioplotted/electrospun constructs confirmed that they morphologically approximated the current human tissue utilized for autologous osteochondral transfer within human joints. Using clinically relevant surgical techniques and commercially available hardware, acellular scaffolds comprised of all three designs were successfully implanted in situ using a porcine cadaveric knee. However, the stacked electrospun nanofibrous scaffolds generated by collagen binding of multiple single electrospun layers easily delaminated when implanted in the porcine knee. These stacked scaffolds needed to be frozen prior to implantation in order to prevent delamination. This could be a critical factor when dealing with seeded scaffolds and can affect cell viability. The 3D-bioplotted and combined 3D-bioplotted/electrospun scaffolds allowed for creation of clinically relevant thicknesses (5–7 mm) and were easily implanted using standard surgical procedures without delamination or breakage. This suggests a facile implementation of current autograft human osteochondral techniques to implant such multiphasic osteochondral scaffolds, indicating the immediate potential clinical translatability of our proposed combined micro- and nanofibrous scaffolds.

## 5. Conclusion

Creation and utilization of appropriate scaffold architecture are a critical step towards generation of an engineered tissue construct that mimics complex native tissue. Electrospun nanofibrous scaffolds, with their dense framework, pore sizes, and fiber diameters, have limitations for creation of three-dimensional structures of relevant physiological thicknesses. We compared these nanofibrous scaffolds to 3D-bioplotted scaffolds, constructs with better dimensional control and reproducibility but thicker fibers and larger pore sizes. We combined these two fabrication approaches, with results indicating that a combination of 3D-bioplotted and electrospun scaffolds could provide an excellent alternative for full

heterogenous tissue regeneration. We tested our scaffolds in a relevant implantation model for osteochondral tissue and showed that although electrospun scaffolds yield higher cell proliferation, they are hard to manipulate during a clinically relevant osteochondral transplantation technique. Our combined scaffold was easily implanted using common surgical procedures into an osteochondral defect, without delamination or breaking of the scaffold.

This is one of the first studies to combine two commonly used scaffold fabrication technologies into a simple scaffold to more closely match thicker tissues with heterogenous matrix architecture. Such approaches may hold great potential for tissue engineering and regenerative medicine applications.

## Conflicts of Interest

The authors declare that there are no conflicts of interest regarding the publication of this paper.

## Acknowledgments

Special thanks are due to Saahil Mehendale for support on scaffold design. This work was supported in part by the Orthopaedic Research and Education Foundation 15-059 (Jeffrey Spang), NIH/NIBIB 1R03EB008790 (Elizabeth G. Lobo), NIH/CTSA 550KR71418 (Elizabeth G. Lobo), NIH/CTSA 550KR61325 (Elizabeth G. Lobo), and NSF/CBET 1133427 (Elizabeth G. Lobo). The 3D-printing aspect of this study was supported by a grant from NCSU Faculty Research and Professional Development (FRPD) program (Rohan A. Shirwaiker).

## References

- [1] Y. Ikada, "Challenges in tissue engineering," *Journal of the Royal Society Interface*, vol. 3, no. 10, pp. 589–601, 2006.
- [2] R. L. Robert Lanza and J. P. Vacanti, "Principles of Tissue Engineering," 2013.
- [3] A. Yousefi, M. E. Hoque, R. G. Prasad, and N. Uth, "Current strategies in multiphasic scaffold design for osteochondral tissue engineering: a review," *Journal of Biomedical Materials Research Part A*, vol. 103, no. 7, pp. 2460–2481, 2014.
- [4] J. E. Jeon, C. Vaquette, T. J. Klein, and D. W. Huttmacher, "Perspectives in multiphasic osteochondral tissue engineering," *Anatomical Record*, vol. 297, no. 1, pp. 26–35, 2014.
- [5] M. Lee and B. M. Wu, "Recent advances in 3D printing of tissue engineering scaffolds," *Methods in Molecular Biology*, vol. 868, pp. 257–267, 2012.
- [6] S. J. Hollister, "Porous scaffold design for tissue engineering," *Nature Materials*, vol. 4, pp. 518–524, 2005.
- [7] J. C. Bernhard and G. Vunjak-Novakovic, "Should we use cells, biomaterials, or tissue engineering for cartilage regeneration?" *Stem Cell Research & Therapy*, vol. 7, p. 56, 2016.
- [8] S. P. Nukavarapu and D. L. Dorcenus, "Osteochondral tissue engineering: current strategies and challenges," *Biotechnology Advances*, vol. 31, no. 5, pp. 706–721, 2013.
- [9] C. Cai, P. Sheshadri, R. A. Shirwaiker, and E. G. Lobo, "Effect of three dimensional polycaprolactone/hydroxyapatite scaffold architecture on proliferation and osteogenesis of human adipose derived stem cells," in *Proceedings of the TERMIS Americas*

- Annual Conference & Exposition*, T. E. P. A, Ed., Washington, DC, USA, 2014.
- [10] L. F. Mellor, S. Mehendale, M. Mohiti-Asli et al., *Evaluation of Micro and Nano-Scale Scaffold Architectures for Osteochondral Tissue Engineering*, Orthopaedic Research Society, Las Vegas, Nev, USA, 2015.
- [11] S. V. Mehendale, L. F. Mellor, M. A. Taylor, E. G. Lobo, and R. A. Shirwaiker, *Rapid Prototyping Journal*, vol. 23, 2017.
- [12] S. D. McCullen, Y. Zhu, S. H. Bernacki et al., "Electrospun composite poly(L-lactic acid)/tricalcium phosphate scaffolds induce proliferation and osteogenic differentiation of human adipose-derived stem cells," *Biomedical Materials*, vol. 4, no. 3, Article ID 035002, 2009.
- [13] J. C. Bodle, S. D. Teeter, B. H. Hluck, J. W. Hardin, S. H. Bernacki, and E. G. Lobo, "Age-related effects on the potency of human adipose-derived stem cells: creation and evaluation of superlots and implications for musculoskeletal tissue engineering applications," *Tissue Engineering—Part C: Methods*, vol. 20, no. 12, pp. 972–983, 2014.
- [14] P. A. Zuk, M. Zhu, H. Mizuno et al., "Multilineage cells from human adipose tissue: implications for cell-based therapies," *Tissue Engineering*, vol. 7, no. 2, pp. 211–228, 2001.
- [15] B. T. Estes, B. O. Diekman, J. M. Gimble, and F. Guilak, "Isolation of adipose-derived stem cells and their induction to a chondrogenic phenotype," *Nature Protocols*, vol. 5, no. 7, pp. 1294–1311, 2010.
- [16] S. H. Bernacki, M. E. Wall, and E. G. Lobo, "Isolation of human mesenchymal stem cells from bone and adipose tissue," *Methods in Cell Biology*, vol. 86, pp. 257–278, 2008.
- [17] G. Zhou, W. Liu, L. Cui, X. Wang, T. Liu, and Y. Cao, "Repair of porcine articular osteochondral defects in non-weightbearing areas with autologous bone marrow stromal cells," *Tissue Engineering*, vol. 12, no. 11, pp. 3209–3221, 2006.
- [18] C. T. Lim, X. Ren, M. H. Afizah et al., "Repair of osteochondral defects with rehydrated freeze-dried oligo[poly(ethylene glycol) fumarate] hydrogels seeded with bone marrow mesenchymal stem cells in a porcine model," *Tissue Engineering—Part A*, vol. 19, no. 15-16, pp. 1852–1861, 2013.
- [19] V. Bobic, C. D. Morgan, and T. Carter, "Osteochondral autologous graft transfer," *Operative Techniques in Sports Medicine*, vol. 8, no. 2, pp. 168–178, 2000.
- [20] C. L. Camp, M. J. Stuart, and A. J. Krych, "Current concepts of articular cartilage restoration techniques in the knee," *Sports Health*, vol. 6, no. 3, pp. 265–273, 2014.
- [21] A. Bedi, B. T. Feeley, and R. J. Williams III, "Management of articular cartilage defects of the knee," *The Journal of Bone and Joint Surgery Series A*, vol. 92, no. 4, pp. 994–1009, 2010.
- [22] L. F. Mellor, M. Mohiti-Asli, J. Williams et al., "Extracellular calcium modulates chondrogenic and osteogenic differentiation of human adipose-derived stem cells: a novel approach for osteochondral tissue engineering using a single stem cell source," *Tissue Engineering Part A*, vol. 21, no. 17-18, pp. 2323–2333, 2015.
- [23] M. L. A. da Silva, A. Martins, A. R. Costa-Pinto et al., "Cartilage tissue engineering using electrospun PCL nanofiber meshes and MSCs," *Biomacromolecules*, vol. 11, no. 12, pp. 3228–3236, 2010.
- [24] W. Li, C. T. Laurencin, E. J. Caterson, R. S. Tuan, and F. K. Ko, "Electrospun nanofibrous structure: a novel scaffold for tissue engineering," *Journal of Biomedical Materials Research*, vol. 60, no. 4, pp. 613–621, 2002.
- [25] W. J. Li, R. Tuli, C. Okafor et al., "A three-dimensional nanofibrous scaffold for cartilage tissue engineering using human mesenchymal stem cells," *Biomaterials*, vol. 26, no. 6, pp. 599–609, 2005.
- [26] S. V. Murphy and A. Atala, "3D bioprinting of tissues and organs," *Nature Biotechnology*, vol. 32, no. 8, pp. 773–785, 2014.
- [27] M. Yeo and G. Kim, "Cell-printed hierarchical scaffolds consisting of micro-sized polycaprolactone (PCL) and electrospun PCL nanofibers/cell-laden alginate struts for tissue regeneration," *Journal of Materials Chemistry B*, vol. 2, pp. 314–324, 2014.

## Clinical Study

# Management of Hepple Stage V Osteochondral Lesion of the Talus with a Platelet-Rich Plasma Scaffold

Wenqi Gu,<sup>1</sup> Tanzhu Li,<sup>2</sup> Zhongmin Shi,<sup>1</sup> Guohua Mei,<sup>1</sup> Jianfeng Xue,<sup>1</sup>  
Jian Zou,<sup>1</sup> Xiaokang Wang,<sup>1</sup> Haotong Zhang,<sup>1</sup> and Hongwei Xu<sup>1</sup>

<sup>1</sup>Shanghai Jiaotong University Affiliated Sixth People's Hospital, Shanghai 200233, China

<sup>2</sup>The People's Hospital of Shigatse City, Shigatse, Tibet 857000, China

Correspondence should be addressed to Zhongmin Shi; 18930177323@163.com

Received 26 December 2016; Accepted 8 March 2017; Published 16 March 2017

Academic Editor: Zheng Ren

Copyright © 2017 Wenqi Gu et al. This is an open access article distributed under the Creative Commons Attribution License, which permits unrestricted use, distribution, and reproduction in any medium, provided the original work is properly cited.

There has been no consensus on the treatment or prognosis of Hepple stage V osteochondral lesions of the talus (OLTs), especially for lesions greater than 1.5 cm<sup>2</sup> in size. The objective of this study was to investigate the clinical outcomes achieved upon application of a platelet-rich plasma (PRP) scaffold with a cancellous bone autograft for Hepple stage V OLTs. Fourteen patients (mean age, 39 years) were treated with a cancellous bone graft and a PRP scaffold between 2013 and 2015. The mean time to surgical treatment was 23.5 months. Ankle X-ray and magnetic resonance imaging were performed at the final follow-up. Functional outcomes were evaluated according to the Visual Analog Scale (VAS) score, American Orthopaedic Foot and Ankle Society (AOFAS) score, and Short Form 36 (SF-36) score. The range of motion (ROM) of the ankle joint and complications also were recorded. Thirteen patients completed the full follow-up, with a mean follow-up duration of 18 months. MRI demonstrated the complete regeneration of subchondral bone and cartilage in all patients. The postoperative VAS, AOFAS ankle and hindfoot, and SF-36 scores were improved significantly (all  $P < 0.001$ ) without obvious complications. We suggest that, for the Hepple stage V OLTs, management with cancellous bone graft and PRP scaffold may be a safe and effective treatment.

## 1. Introduction

Osteochondral lesions of the talus (OLTs) often cause pain and disability and present a great challenge to foot and ankle surgeons. The size of lesions varies, and a subchondral cyst can develop if the lesion is left untreated. In 1999, Hepple and colleagues developed a new classification system for OLTs with five stages according to MRI manifestation [1]. The identifying characteristic of a stage V lesion is the formation of subchondral cyst, which makes treatment more difficult. The key point of management for this type of lesion is to reconstruct and repair the subchondral bone and cartilage simultaneously. Although various procedures for treating subchondral cystic OLTs have been reported, including arthroscopic microfracture, retrograde arthroscopic procedure, autograft or allograft of osteochondral peg, and chondrocyte transplantation [2–6], the best treatment approach remains controversial. The arthroscopic microfracture technique is widely

preferred by surgeons due to the advantages of minimal invasion and supporting quick recovery, but the success rate has only been satisfactory for cases of small- or mid-sized lesions [2]. Large lesions (>1.5 cm<sup>2</sup>) with subchondral cyst tend to respond poorly to microfracture. The retrograde arthroscopic technique is ideal for large cystic lesions with intact cartilage [5]. However, in most cases, the cartilage over the lesion site is also unstable and prone to dehiscence. The osteochondral peg autograft or allograft may be a reasonable option for these lesions, because it allows simultaneous restoration of cartilage and subchondral bone. However, the undesirable donor site morbidity [7], curvature mismatch, and healing rate remain problems [8]. Chondrocyte transplantation may be a promising approach, but the high expense and two-stage operation are major challenges in China. Based on the disadvantages of the above-mentioned techniques for application in cases of Hepple stage V OLTs, we have attempted to develop a reliable technique for repairing this type of lesion.

Cancellous bone autograft is a reasonable technique for repairing a subchondral bone defect after debridement of a cyst that avoids obvious donor site injuries. However, the repair of cartilage lesion remains a great concern. Platelet-rich plasma (PRP) has been proposed as a novel treatment modality for the management of articular cartilage injuries, wound healing, nonunion, muscle injury, and tendon disease [9–13]. The potential of PRP for cartilage repair has been demonstrated through its anabolic effect on chondrocytes, mesenchymal stem cells (MSCs), and synoviocytes as well as its ability as a bioactive cell scaffold to fill defects and enhance cartilage regeneration [14]. Animal experiments also demonstrated that adjunctive use of PRP produced a better healing response than a mosaicplasty-only procedure for osteochondral lesions [15]. Currently, PRP is mainly applied as an additional postoperative therapy [16]. Considering the great potential of PRP for cartilage repair and regeneration, we applied a cancellous bone autograft with a PRP scaffold for treatment of Hepple stage V OLTs.

The objective of this study was to investigate surgical techniques and clinical outcomes of using a PRP scaffold with a cancellous bone autograft to repair a Hepple stage V OLT. We hypothesized that PRP would be a reliable scaffold for cartilage regeneration and be beneficial to the healing process for a large Hepple stage V OLT.

## 2. Material and Methods

**2.1. Patient Recruitment.** The current study was approved by Shanghai Sixth People's Hospital ethics review board. All participants signed an informed consent form before the study.

The inclusion criteria of this study were (1) stage V OLT according to MRI classification by Hepple et al. [1]; (2) lesion size  $> 1.5 \text{ cm}^2$ ; (3) age from 18–60 years; (4) primary or revision procedure; (5) normal ankle and hindfoot alignment; and (6) involvement of medial dome with cartilage dehiscence. The exclusion criteria were (1) diffusive degenerative joint changes; (2) inflammatory arthritis or chronic inflammatory disease; (3) history of infection; (4) malalignment of ankle and hindfoot; (5) nonreconstructable defect; (6) body mass index  $> 30 \text{ kg/m}^2$ ; (7) central or lateral lesion; and (8) subtalar joint involvement. Complete clinical and radiographic evaluations were carried out preoperatively, including X-ray examination, computed tomography (CT) scanning, and MRI scanning of the ankle joint. The preoperative Visual Analog Scale (VAS) score, American Orthopaedic Foot and Ankle Society (AOFAS) ankle and hindfoot score, Short Form 36 (SF-36) score, and range of motion (ROM) of the ankle joint were also documented.

**2.2. PRP Scaffold Preparation.** PRP scaffolds were prepared using the WEGO Platelet-Rich Plasma Preparation Kit (WEGO Ltd., Shandong, China). Approximately 40 mL of blood was taken from patient's arm, placed in a tube provided in the kit, and spun twice in a portable centrifuge (WEGO Ltd.) at 2000 rpm for 10 minutes each time. This standard process produced 3–4 mL of plasma.



FIGURE 1: A medial approach followed with a medial malleolar osteotomy was performed.



FIGURE 2: After elevation of injured cartilage, the cyst was debrided and prepared for cancellous bone autograft.

**2.3. Surgical Technique.** Following the induction of general anesthesia, the patient was laid supine on the operating table with a pneumatic tourniquet applied to the thigh. The iliac crest region was prepared. For patients with an anteromedial lesion, a standard anteromedial approach was made from the anterior border of medial malleolar, which lay between the anterior tibial tendon and posterior tibial tendon, to the navicular tubercle. After dissection of the superficial layer of the deltoid ligament and plantar flexion of the ankle joint, the anteromedial lesion was visualized. For patients with a centromedial or posteromedial lesion, a medial approach was performed from the center of medial malleolar to 6–7 cm proximally and to the navicular tubercle distally. A capsulotomy was made after dissection from the anterior medial malleolar. After positioning the osteotomy line by a guide K-wire, the medial malleolar osteotomy was performed using an oscillating saw with an osteotome for the final cut. The medial malleolar fragment was rotated for exposure, and the lesion area was confirmed (Figure 1).

After elevation of unstable cartilage, the sclerotic subchondral lamella was resected with a mini osteotome, and the cyst was debrided with a curette (Figure 2). After the defect size was measured, a 2.0 mm K-wire was used for drilling of the sclerotic subchondral bone. Next, the cancellous bone autograft was harvested from the iliac crest. The autograft was designed to fill the defect to about 2 mm below the cartilage (Figure 3). The superficial layer of the cancellous bone was covered by the prepared PRP scaffold (Figure 4).

For patients in whom medial malleolar osteotomy was performed, reduction of the medial malleolar fragment was achieved before fixation with two 4.3 mm cannulated screws (Qwix, Newdeal, France). After fluoroscopic evaluation, the



FIGURE 3: The subchondral defect was filled with cancellous bone.

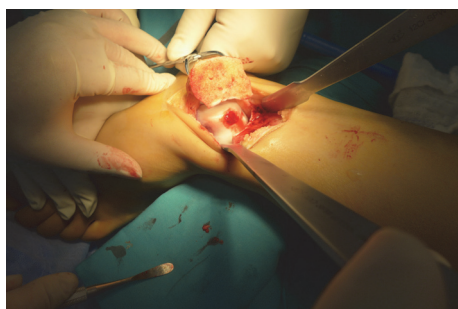


FIGURE 4: The PRP scaffold coverage was performed.

capsule and wound were sutured. For the patients with lateral instability, lateral collateral ligament reconstruction was performed via a lateral approach.

**2.4. Postoperative Management.** The RICE (rest, ice, compression, and elevation) principle was applied with a short-leg cast for immobilization. Toe, knee, and hip ROM exercises were started on the second day postoperatively. All patients had postoperative follow-up assessments at 2 weeks and 1, 2, 3, 6, 12, and 24 months after the operation. The wound was checked at 2 weeks postoperatively. If no soft tissue problem was observed, the skin sutures were removed. Patients were fitted with a walking boot after 2 weeks and began ankle ROM exercises. Weight-bearing was permitted at 3 months postoperatively still with the protection of the walking boot. The anteroposterior and lateral view on plain X-ray and MRI scanning were taken during the follow-up. The clinical outcome was evaluated by the VAS, AOFAS ankle and hindfoot, and SF-36 scores. The ROM of the ankle joint was also measured. The neutral position of the ankle was defined as 0°. All complications were recorded during the follow-up assessment.

**2.5. Statistical Analysis.** SAS 8.0 (SAS Institute Inc., Cary, NC, USA) was used for statistical analysis. The *t*-test was applied for comparison of preoperative and postoperative ROM of the ankle joint, VAS score, AOFAS score, and SF-36 score.  $P < 0.05$  represented a statistically significant difference.

### 3. Results

Fourteen patients who were treated between 2013 and 2015 in our hospital were enrolled in this study. The study population



FIGURE 5: The series of X-ray demonstrated the bony union of osteotomy site on the 3rd month postoperatively. The collateral ligament was also repaired in this patient.

included 10 males and 4 females with an average age of 39 years (range, 21–57 years). The mean time from onset to surgical treatment was 23.5 months (range, 11–48 months). Nine cases (64.3%) were left side involved, and five cases (35.7%) were right side involved. Of the 14 patients, 10 (71.4%) patients had a history of ankle sprain, and 4 (28.6%) patients had spent a long period for professional sports. Three (21.4%) patients underwent a primary arthroscopic procedure, whereas the others had received conservative therapy for at least 6 months. Lateral instability was seen in three (21.4%) cases. The average lesion size was 2.1 cm<sup>2</sup> (range, 1.6–3.0 cm<sup>2</sup>). According to the measurements on MRI, 8 patients were 1.6–2.0 cm<sup>2</sup>, 4 cases were 2.1–2.5 cm<sup>2</sup>, and another 2 cases were 2.6–3.0 cm<sup>2</sup>. According to Raikin and Elias's talar dome 9-zone grid system [17], 8 cases had a lesion in zone 4 (centromedial zone), 5 cases had a lesion in zone 7 (posteromedial zone), and 1 case had a lesion in zone 1 (anteromedial zone).

All the wounds healed without complications of infection or skin necrosis. Thirteen patients completed the full follow-up for an average of 18 months (range, 12–24 months). One patient was lost to follow-up after suture removal. Postoperative plain X-ray demonstrated that bony union of the osteotomy site was achieved in all patients within 3 months without malunion (Figure 5). The VAS score, AOFAS ankle and hindfoot score, SF-36 score, and ROM of ankle joint were all improved significantly postoperatively (Table 1). MRI manifested the restoration of the subchondral bone and a good congruence and curvature of the regenerated cartilage along the surrounding cartilage in all cases (Figure 6). No cases of implant failure, recurrence of lesion, or degenerative arthritis occurred during the follow-up, and no patients required a second stage of operation.

### 4. Discussion

Hepple stage V OLTs with a subchondral bone cyst are great challenges for foot and ankle surgeons. Most lesions of this

TABLE 1: The comparison of clinical evaluation.

	VAS (mean $\pm$ SD) (4~9)	AOFAS (mean $\pm$ SD) (31~73)	SF-36 (mean $\pm$ SD) (50~70)	Plantar flexion (mean $\pm$ SD) (5°~36°)	Dorsiflexion (mean $\pm$ SD) (0°~12°)
Pre-op	6.1 $\pm$ 1.5 (4~9)	54.0 $\pm$ 10.6 (31~73)	62.0 $\pm$ 5.9 (50~70)	22.8 $\pm$ 8.9° (5°~36°)	8.0 $\pm$ 3.4° (0°~12°)
Post-op	1.1 $\pm$ 1.0 (0~3)	86.2 $\pm$ 6.4 (74~100)	85.3 $\pm$ 5.9 (73~95)	35.5 $\pm$ 6.0° (25°~45°)	17.2 $\pm$ 3.1° (12°~22°)
P value	$P < 0.0001$	$P < 0.0001$	$P < 0.0001$	$P < 0.0001$	$P < 0.0001$



FIGURE 6: The MRI manifested that the large size of subchondral cystic lesion (a) was successfully repaired with a congruent curvature (b).

stage are symptomatic and require surgical management, but limited data are available regarding the best surgical strategy and corresponding clinical outcomes. The key point for this type of lesion is to simultaneously address the subchondral defect and cartilage lesion. This study aimed to investigate a new method for treating this type of lesion.

For the management of OLTs, the selection of the treatment protocol depends on various factors, including patient age, lesion size, and cyst formation, which all play important roles in the prediction of prognosis. Some patients with OLTs may benefit from a primary arthroscopic surgery regardless of the existence of a subchondral cyst [2]. However, the size of the lesion is a major predictive factor of prognosis after the arthroscopic procedure, which may be less suitable for large-sized lesions greater than 1.5 cm<sup>2</sup> [2, 18]. Robinson et al. reported an unsatisfied outcome in 53% patients of cystic lesion [19]. In the present case series, all of the patients had a large lesion with an average area of 2.1 cm<sup>2</sup>; however we achieved a satisfied outcome. The retrograde technique may be ideal for large OLTs with a subchondral cyst and intact cartilage [5]. The use of some cannulated systems may simplify the procedure and facilitate accurate bone graft. However, in our patient group, cartilage dehiscence was confirmed in all patients preoperatively, which counter-indicated the use of the retrograde technique. Jeong et al. [20] reported the retrograde technique for subchondral cystic OLTs. A progressing arthritic change of ankle joint was confirmed at the first year postoperatively. And they concluded that retrograde procedure might not be theoretically correct and would damage the uninjured bone marrow. The osteochondral autograft may be an acceptable technique for treating stage V OLTs based on the simultaneous restoration of the subchondral bone and cartilage. However, the donor site morbidity is a great concern in the knee-to-ankle procedure, which was reported as high as 16.9% [21], and may cause pain for a period of time [22]. Moreover, for a large size of cystic OLT, a larger subchondral

bone peg is needed for autograft, which may increase the risk of donor site injury. However, with a cancellous autograft technique, the donor site symptoms did not occur in our study.

Cancellous bone autograft is an appropriate method with limited injury to the donor site that offers better restoration of the mechanical properties of the talus. A fresh cancellous bone graft populated with native cells was used to facilitate the regeneration and growth of subchondral bone. In our patients, from the follow-up X-ray and MRI we observed a satisfied regeneration of the subchondral bone without bone resorption or recurrence of the cyst, indicating that cancellous bone autograft is an effective method for treating subchondral cysts. Furthermore, the successful reconstruction of the subchondral bone significantly relieved the patients' symptoms, as the postoperative VAS score was obviously improved and no donor site morbidity was seen in this study.

Repair of cartilage lesions is another challenge. After elevation and debridement of injured cartilage, the resulting defect will be hardly healed due to the limited ability of cartilage regeneration. PRP has been proven to have protective effects against chondrocyte apoptosis, inhibit inflammatory processes, improve the cartilage repair, and stimulate the migration and chondrogenic differentiation of human subchondral progenitor cells [23–27]. Thus, application of PRP offers a new method for cartilage repair [9, 28]. In spite of these promising features, PRP has been mainly applied via injection as an additional method for treating OLTs in previous research [16, 29], and the effects of PRP on the repair of large cartilage lesion have been rarely reported. Our application of a PRP scaffold after cancellous bone autograft has several advantages. First, it is convenient and safe to prepare the PRP without obvious donor site morbidity and complications. In this study, no complications associated with PRP collection were observed. In addition, as described above, curvature mismatch is a difficult problem associated with a subchondral peg autograft that sometimes causes symptoms and

compromises the clinical outcome. However, with the PRP scaffold, we could repair and restore the cartilage with congruence along the curvature. Furthermore, the patients in this group were young, implying a better chondrocyte viability, greater regeneration capacity, and less degeneration of cartilage. Therefore, for young patients, cartilage repair is more likely to be achieved with the support of a PRP scaffold. During the follow-up, we applied MRI not only for the prediction of prognosis, but also to confirm the restoration of the subchondral bone and cartilage and the congruity of the facet, which is a positive and scientific method for assessment. The follow-up MRI demonstrated that the regenerated cartilage had a good shape and thickness, matching that of the surrounding cartilage, which suggested a better match of properties with native cartilage. Better congruity of the facet is expected to benefit symptom relief and functional recovery. Therefore, we achieved a significant functional improvement and relief of pain in our study.

This study still has some limitations. First, the sample size of this study was small and the control group was not set up for comparison in this study. However, Hepple stage V lesion is uncommon in the clinical work, which may make a comparative study more difficult. Then, the follow-up time was not long enough and long-term outcome remains unknown. Third, the type and characteristics of the regenerated cartilage were unknown and should be confirmed by repeated arthroscopy with histological evaluation, which is less practicable in China. These limitations will be attempted to address in the future. Last, this study excluded patients with a central or lateral lesion. As acceptable clinical outcomes were obtained in this preliminary study, we may expand the application of this approach.

## 5. Conclusion

Application of a PRP scaffold with a cancellous bone autograft in the treatment of Hepple stage V OLTs may achieve acceptable short-term clinical outcomes with better regeneration of cartilage and subchondral bone with better congruity and minimal complications. Closer observation of the effects of PRP on Hepple stage V OLTs is recommended.

## Conflicts of Interest

All authors state that they have no conflicts of interest.

## Authors' Contributions

Wenqi Gu and Tanzhu Li contributed equally to this study and should be regarded as first authors.

## References

- [1] S. Hepple, I. G. Winson, and D. Glew, "Osteochondral lesions of the talus: a revised classification," *Foot and Ankle International*, vol. 20, no. 12, pp. 789–793, 1999.
- [2] K.-B. Lee, H.-W. Park, H.-J. Cho, and J.-K. Seon, "Comparison of arthroscopic microfracture for osteochondral lesions of the talus with and without subchondral cyst," *The American Journal of Sports Medicine*, vol. 43, no. 8, pp. 1951–1956, 2015.
- [3] D. Georgiannos, I. Bisbinas, and A. Badeskas, "Osteochondral transplantation of autologous graft for the treatment of osteochondral lesions of talus: 5- to 7-year follow-up," *Knee Surgery, Sports Traumatology, Arthroscopy*, vol. 24, no. 12, pp. 3722–3729, 2016.
- [4] E. Giza, C. Delman, J. C. Coetzee, and L. C. Schon, "Arthroscopic treatment of talus osteochondral lesions with particulated juvenile allograft cartilage," *Foot and Ankle International*, vol. 35, no. 10, pp. 1087–1094, 2014.
- [5] C. F. Hyer, G. C. Berlet, T. M. Philbin, and T. H. Lee, "Retrograde drilling of osteochondral lesions of the talus," *Foot & Ankle Specialist*, vol. 1, no. 4, pp. 207–209, 2008.
- [6] S. K. Kwak, B. S. Kern, R. D. Ferkel, K. W. Chan, S. Kasraeian, and G. R. Applegate, "Autologous chondrocyte implantation of the ankle: 2- to 10-year results," *The American Journal of Sports Medicine*, vol. 42, no. 9, pp. 2156–2164, 2014.
- [7] J. D. F. Calder, M. S. Ballal, R. S. Deol, C. J. Pearce, P. Hamilton, and M. Lutz, "Histological evaluation of calcaneal tuberosity cartilage—a proposed donor site for osteochondral autologous transplant for talar dome osteochondral lesions," *Foot and Ankle Surgery*, vol. 21, no. 3, pp. 193–197, 2015.
- [8] J. Ahmad and K. Jones, "Comparison of osteochondral autografts and allografts for treatment of recurrent or large talar osteochondral lesions," *Foot and Ankle International*, vol. 37, no. 1, pp. 40–50, 2016.
- [9] A. T. Sengul, Y. B. Buyukkkarabacak, B. Z. Altunkaynak et al., "Effects of platelet-rich plasma on cartilage regeneration after costal cartilage resection: a stereological and histopathological study," *Acta Chirurgica Belgica*, vol. 117, no. 1, pp. 21–28, 2017.
- [10] M. Ahmed, S. A. Reffat, A. Hassan, and F. Eskander, "Platelet-rich plasma for the treatment of clean diabetic foot ulcers," *Annals of Vascular Surgery*, vol. 38, pp. 206–211, 2017.
- [11] G. Zanon, F. Combi, A. Combi, L. Perticarini, L. Sammarchi, and F. Benazzo, "Platelet-rich plasma in the treatment of acute hamstring injuries in professional football players," *Joints*, vol. 4, no. 1, pp. 17–23, 2016.
- [12] O. Wittig, E. Romano, C. González et al., "A method of treatment for nonunion after fractures using mesenchymal stromal cells loaded on collagen microspheres and incorporated into platelet-rich plasma clots," *International Orthopaedics*, vol. 40, no. 5, pp. 1033–1038, 2016.
- [13] J. Fitzpatrick, M. Bulsara, and M. H. Zheng, "The effectiveness of platelet-rich plasma in the treatment of tendinopathy," *The American Journal of Sports Medicine*, vol. 45, no. 1, pp. 226–233, 2017.
- [14] X. Xie, C. Zhang, and R. S. Tuan, "Biology of platelet-rich plasma and its clinical application in cartilage repair," *Arthritis Research & Therapy*, vol. 16, no. 1, article 204, 2014.
- [15] E. Altan, K. Aydin, O. Erkokcak, H. Senaran, and S. Ugras, "The effect of platelet-rich plasma on osteochondral defects treated with mosaicplasty," *International Orthopaedics*, vol. 38, no. 6, pp. 1321–1328, 2014.
- [16] G. Görmeli, M. Karakaplan, C. A. Görmeli, B. Sarlkaya, N. Elmall, and Y. Ersoy, "Clinical effects of platelet-rich plasma and hyaluronic acid as an additional therapy for talar osteochondral lesions treated with microfracture surgery: a prospective randomized clinical trial," *Foot and Ankle International*, vol. 36, no. 8, pp. 891–900, 2015.
- [17] S. M. Raikin, I. Elias, A. C. Zoga, W. B. Morrison, M. P. Besser, and M. E. Schweitzer, "Osteochondral lesions of the talus:

- localization and morphologic data from 424 patients using a novel anatomical grid scheme,” *Foot & Ankle International*, vol. 28, no. 2, pp. 154–161, 2007.
- [18] J.-I. Choi and K.-B. Lee, “Comparison of clinical outcomes between arthroscopic subchondral drilling and microfracture for osteochondral lesions of the talus,” *Knee Surgery, Sports Traumatology, Arthroscopy*, vol. 24, no. 7, pp. 2140–2147, 2016.
- [19] D. E. Robinson, I. G. Winson, W. J. Harries, and A. J. Kelly, “Arthroscopic treatment of osteochondral lesions of the talus,” *Journal of Bone and Joint Surgery. Series B*, vol. 85, no. 7, pp. 989–993, 2003.
- [20] S. Y. Jeong, J. K. Kim, and K. B. Lee, “Is retrograde drilling really useful for osteochondral lesion of talus with subchondral cyst?: a case report,” *Medicine*, vol. 95, no. 49, Article ID e5418, 2016.
- [21] R. Andrade, S. Vasta, R. Pereira et al., “Knee donor-site morbidity after mosaicplasty—a systematic review,” *Journal of Experimental Orthopaedics*, vol. 3, no. 1, article 31, 2016.
- [22] Y. Zhu and X. Xu, “Osteochondral Autograft transfer combined with cancellous allografts for large cystic osteochondral defect of the talus,” *Foot & Ankle International*, vol. 37, no. 10, pp. 1113–1118, 2016.
- [23] J. Yang, Y. Lu, and A. Guo, “Platelet-rich plasma protects rat chondrocytes from interleukin-1 $\beta$ -induced apoptosis,” *Molecular Medicine Reports*, vol. 14, no. 5, pp. 4075–4082, 2016.
- [24] G. M. Van Buul, W. L. M. Koevoet, N. Kops et al., “Platelet-rich plasma releasate inhibits inflammatory processes in osteoarthritic chondrocytes,” *American Journal of Sports Medicine*, vol. 39, no. 11, pp. 2362–2370, 2011.
- [25] N. A. Smyth, C. D. Murawski, A. M. Haleem, C. P. Hannon, I. Savage-Elliott, and J. G. Kennedy, “Establishing proof of concept: platelet-rich plasma and bone marrow aspirate concentrate may improve cartilage repair following surgical treatment for osteochondral lesions of the talus,” *World Journal of Orthopedics*, vol. 3, no. 7, pp. 101–108, 2012.
- [26] J. P. Krüger, S. Hondke, M. Endres, A. Pruss, A. Siclari, and C. Kaps, “Human platelet-rich plasma stimulates migration and chondrogenic differentiation of human subchondral progenitor cells,” *Journal of Orthopaedic Research*, vol. 30, no. 6, pp. 845–852, 2012.
- [27] H. Li, S. Sun, H. Liu et al., “Use of a biological reactor and platelet-rich plasma for the construction of tissue-engineered bone to repair articular cartilage defects,” *Experimental and Therapeutic Medicine*, vol. 12, no. 2, pp. 711–719, 2016.
- [28] Y. Mifune, T. Matsumoto, K. Takayama et al., “The effect of platelet-rich plasma on the regenerative therapy of muscle derived stem cells for articular cartilage repair,” *Osteoarthritis and Cartilage*, vol. 21, no. 1, pp. 175–185, 2013.
- [29] A. Guney, M. Akar, I. Karaman, M. Oner, and B. Guney, “Clinical outcomes of platelet rich plasma (PRP) as an adjunct to microfracture surgery in osteochondral lesions of the talus,” *Knee Surgery, Sports Traumatology, Arthroscopy*, vol. 23, no. 8, pp. 2384–2389, 2015.

## Research Article

# Maxillary Sinus Augmentation with Decellularized Bovine Compact Particles: A Radiological, Clinical, and Histologic Report of 4 Cases

**Antonio Scarano**

*Department of Medical, Oral and Biotechnological Sciences and CeSi-MeT, University of Chieti-Pescara, Via dei Vestini 31, 66100 Chieti, Italy*

Correspondence should be addressed to Antonio Scarano; [ascarano@unich.it](mailto:ascarano@unich.it)

Received 19 January 2017; Accepted 13 February 2017; Published 2 March 2017

Academic Editor: Changmin Hu

Copyright © 2017 Antonio Scarano. This is an open access article distributed under the Creative Commons Attribution License, which permits unrestricted use, distribution, and reproduction in any medium, provided the original work is properly cited.

**Background.** One of the most problematic regions for endosseous implants is the posterior maxilla, not only having poor bone density, but also lacking adequate vertical height as a result of sinus pneumatization. The purpose of the present study was a radiologic, histological, and histomorphometrical evaluation, in humans, of specimens retrieved from sinuses augmented with decellularized bovine compact particles, after a healing period of 6 months. **Methods.** Four patients, with atrophic resorbed maxillas, underwent a sinus lift augmentation with decellularized bovine compact bone from bovine femur. The size of the particles used was 0.25–1 mm. A total of four grafts and 5 biopsies were retrieved and processed to obtain thin ground sections with the Precise 1 Automated System. **Results.** The mean volume after graft elevation calculated for each of the 4 patients was 2106 mm<sup>3</sup> in the immediate postoperative period (5–7 days), ranging from 1408.8 to 2946.4 mm<sup>3</sup>. In the late postoperative period (6 months) it was 2053 mm<sup>3</sup>, ranging from 1339.9 to 2808.9 mm<sup>3</sup>. Histomorphometry showed that newly formed bone was 36 ± 1.6% and marrow spaces were 34 ± 1.6%, while the residual graft material was 35 ± 1.4%. **Conclusion.** In conclusion, based on the outcome of the present study, Re-Bone® can be used with success in sinus augmentation procedures and 6 months are considered an adequate time for maturation before implant placement.

## 1. Introduction

The rehabilitation of the edentulous posterior maxilla with dental implants often represents a clinical challenge due to the insufficient bone volume resulting from pneumatization of the maxillary sinus and crestal bone resorption. The resultant atrophic residual ridge is one of low-density trabecular bone with a minimal cortical component [1]. The maxillary sinus lifting technique is a common surgical technique to augment bone volume in atrophic posterior maxilla [2] and healing was allowed for about 6 to 8 months before implant insertion [3]. One of the most problematic regions is the posterior maxilla, not only having poor bone density, but also lacking adequate vertical height for endosseous implants as a result of sinus pneumatization. Sinus floor augmentation can provide the necessary bone mass to place and stabilize implants essential for the initial steps towards osseointegration [4].

Different materials are used in sinus lifting, such as autogenous bone grafts [5–7], allografts [8, 9], alloplast [8–11], and xenografts [8, 12, 13].

Bovine bone particles were used with success in sinus lifting [14]. No pathological inflammatory cell infiltrate or foreign body reactions were reported with the use of anorganic bone [15, 16]. Bovine bone has been shown to be highly biocompatible with hard oral tissues in animals and man [17, 18].

The aim of the present study was a radiologic, histological, and histomorphometrical evaluation, in humans, of specimens retrieved from sinuses augmented with decellularized bovine compact particles, after a healing period of 6 months.

## 2. Materials and Methods

Four patients, with atrophic resorbed maxillas, underwent sinus lift augmentation with decellularized bovine compact

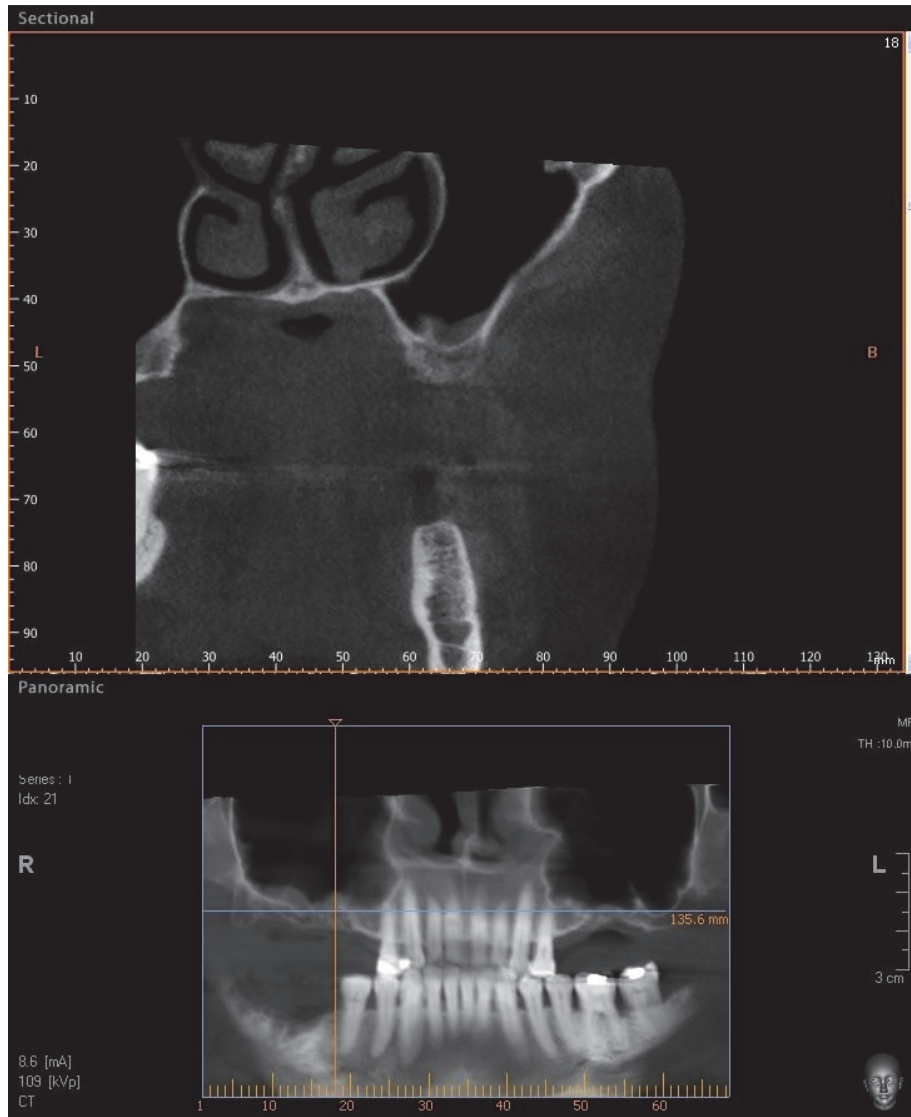


FIGURE 1: CBCT of an edentulous patient with bilateral severely atrophic maxilla.

bone from bovine femur (Re-Bone, UBGEN Padova, Italy) (Figures 1–4). The graft was condensed at each stage and a collagen membrane (SHELTER®, UBGEN Padova, Italy) The sizes of particles used were 0.25–1 mm. The sinus lift procedures were carried out as described by Boyne and James in 1980 (Figures 2–4). In all cases the sinus lifting procedure was considered to be successful and the insertion of implants of at least 12 mm was performed in all cases after 6 months. Biopsy specimens were retrieved at 6 months. A biopsy of the regenerated tissues was carried out with a small trephine under generous saline irrigation (Figures 5–7). A total of four grafts and 5 biopsies were retrieved. The cores were obtained at a mean depth of 12 mm. The specimens were retrieved, washed in saline solution, and immediately fixed in 4% paraformaldehyde and 0.1% glutaraldehyde in 0.15 M cacodylate buffer at 4°C and pH 7.4, to be processed for histology.

The specimens were processed to obtain thin ground sections with the Precise 1 Automated System (Assing, Rome, Italy) [19]. The specimens were dehydrated in an ascending series of alcohol rinses and embedded in a glycolmethacrylate resin (Technovit 7200 VLC, Kulzer, Germany). After polymerization the specimens were sectioned with a high precision diamond disc at about 150  $\mu\text{m}$  and ground down to about 30  $\mu\text{m}$ . The slides were stained with basic fuchsin, toluidine blue, and von Kossa. The histochemical analysis of acid and alkaline phosphatases was carried out according to a previously described protocol. For general morphologic observations, sections were stained with toluidine blue and observed under light microscopy. To determine the relative distribution of the new matrix bone and osteoblast activity, morphological analyses were performed. A polarized light was used to distinguish lamellar bone and woven bone.

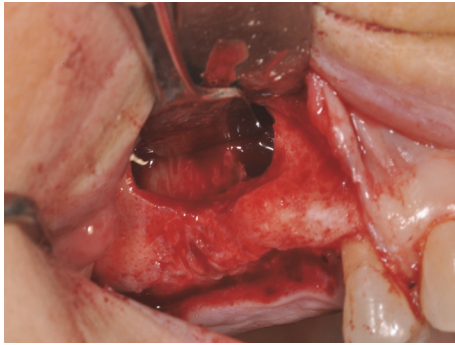


FIGURE 2: Sinus lifting procedure. The maxillary sinus lateral wall is exposed and a bone window is removed.

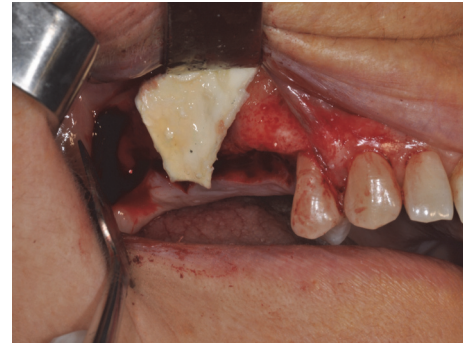


FIGURE 4: A membrane is placed over the antrostomy.

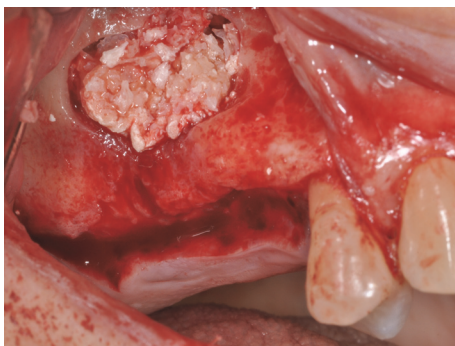


FIGURE 3: Sinus filled with cortical bovine bone.

TABLE 1: Volume after graft elevation mm<sup>3</sup>.

N° Sinus	Immediate postoperative	After 6 months
1	1408	1339
2	2265	2265
3	1808	1800
4	2946	2808
Mean	2106,75	2053,25
SD	660	629

### 3. Results

The mean volume after graft elevation calculated for each of the 4 patients was 2106 mm<sup>3</sup> in the immediate postoperative period (5–7 days), ranging from 1408.8 to 2946.4 mm<sup>3</sup>. In the late postoperative period (6 months) it was 2053 mm<sup>3</sup>, ranging from 1339.9 to 2808.9 mm<sup>3</sup> (Figures 5 and 6). Table 1.

No perforation of the sinus membrane was evident in any of the cases. No acute infection, with pain or fever, was observed. In all cases, bone augmentation showed hyperdensity for comparison between the immediate postoperative period and the late postoperative period, with more density than native bone at both times. The statistical analysis demonstrated a significant difference in volume alterations ( $P = 0.0119$ ).

In general, bone morphology was well present with well differentiated cellular constituents mineralized bone,

osteoid, osteoblasts, osteocytes, and blood vessels. At low magnification, trabecular mature bone was observed (Figures 7 and 8). The initial formation of immature bone extending from the periphery of the bone cavities was evident. The rest of the bone cavity contained mature tissue and biomaterial with a mild inflammatory reaction.

Re-Bone particles were easily distinguished from the newly formed bone: they tended to be less stained due to the low content of collagen. The particles were surrounded by newly formed bone (Figures 8 and 9). In a few marrow space areas, in which it was possible to find small capillaries, some particles were present at the interface. In some areas osteoblasts were observed in the process of posing bone directly onto the particle surface. Some positive osteoclast for acid phosphatase and a few positive osteoblast for alkaline phosphatases were observed. Histomorphometry showed that newly formed bone was  $36 \pm 1.6\%$  and marrow spaces were  $34 \pm 1.6\%$ , while the residual graft material was  $35 \pm 1.4\%$ .

### 4. Discussion

Oral rehabilitation with osseointegrated implants is very successful and predictable in patients with normal bone volume and density, which provide adequate stabilization of implants of standard diameter and length [20]. Rehabilitation of the edentulous posterior maxilla with dental implants is often difficult because bone height is insufficient and cancellous [2].

Although there is a high risk of implant displacement/migration into the maxillary, this has been only rarely reported [10, 21]. Different biomaterials can be successfully used for sinus lifting. Many research data show that bovine bone grafting in this areas is not contraindicated and represent a procedure with low morbidity [2, 4]. This xenograft is the one most commonly used material for sinus floor augmentation and has the most powerful scientific evidence for sinus grafting [2, 4, 14, 19, 22–24] because its structure is similar to that of human [22].

In fact the outcomes of the present study showed that the Re-Bone particles appeared to be surrounded by an abundant quantity of newly formed bone. This biomaterials appeared to undergo a slow resorption process; in fact in the present study, after 6 months of observation, most of the grafting material

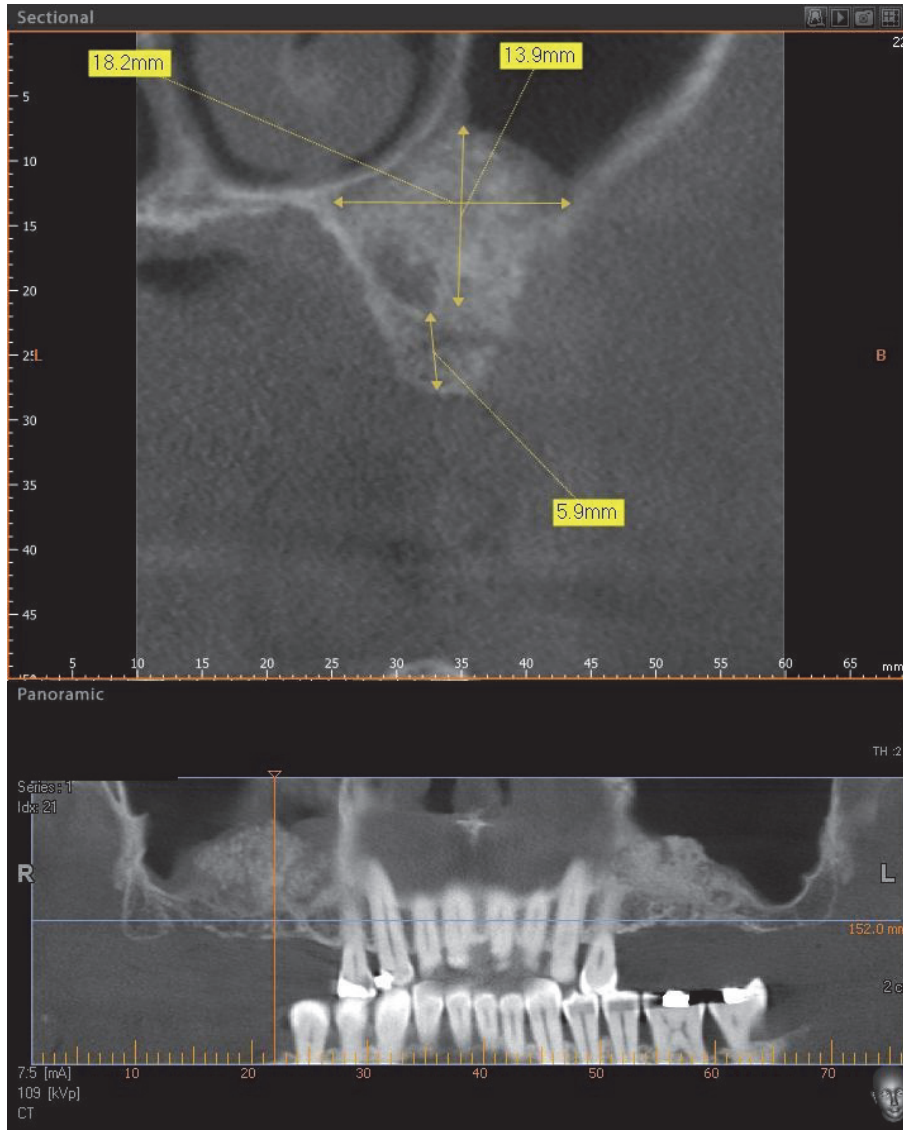


FIGURE 5: Postoperative CBCT scan panoramic view at 6 months after maxillary sinus lifting.



FIGURE 6: The lateral wall is completely closed by new hard tissues.

was still in place. This study is consistent with other studies reported that the use the bovine bone as a grafting material

yielded a bone formation and no presence of inflammatory cell infiltrate [25, 26]. Close contact between most of the materials and the newly formed osseous tissue was present, near but not in contact with the implant surface [14]. Several authors have discussed the use of different graft materials and have documented results both similar and varied when compared to those in the present study [14, 23]. A biomaterial similar to Re-Bone is the Bio-Oss®; this has a similar size, structure, and biological response with conducive to vessel ingrowth [15, 21]. According to our experience and previous literature, we did not observe histological differences between Bio-Oss and Re-Bone [14, 23]. The outcomes of this study revealed new bone formation around the graft particles ( $36 \pm 1.6\%$ ) within the maxillary sinus after six months of healing. The particles showed absence of gaps at the bone-particles interface, and the bone was always in close contact with the particles. This xenograft has excellent osteoconductive

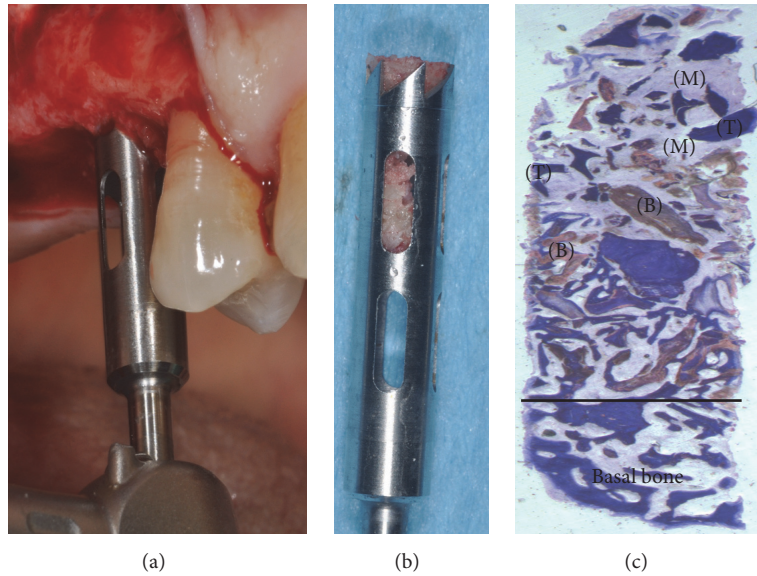


FIGURE 7: (a-b) Bone core biopsy carried out with a small trephine. (c) Newly formed trabecular bone (T) is present, with wide marrow (M) spaces and biomaterials (B). Toluidine blue 10x.

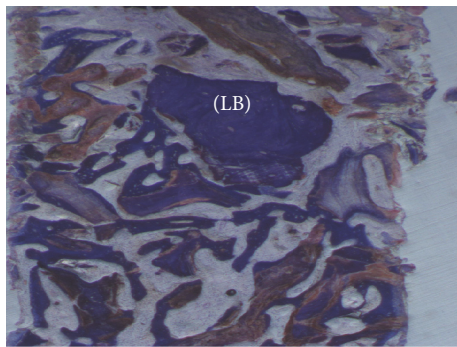


FIGURE 8: At higher magnification previous image: a few lamellar bones are visible (LB). Toluidine blue 50x.

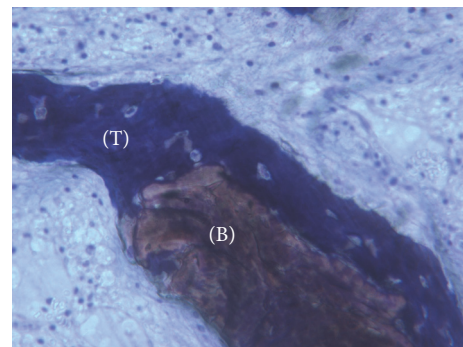


FIGURE 9: No gaps are present at the bone-particles interface, and newly formed bone is always in close contact with the particles. The biomaterial (B) seems to be totally incorporated in the trabecular bone (T). Toluidine blue 100x.

properties; in fact the outcomes of the present study showed that the Re-Bone particles appeared to be surrounded by an abundant quantity of newly formed bone. Probably, also Re-Bone can be resorbed by osteoclasts [21, 24]. The grafted biomaterial was clearly distinguishable from the remaining original bone due to its density and structure. This is the first case reported in the literature to use Re-Bone granules as bone grafts in sinus lifts. The granular nature of the material facilitated its application between the sinus filling and newly formed bone. *Through* surgery, the scaffold can be easily adapted to the dimension and of the sinus. During graft placement it can quickly adsorb the blood molecules and cells promoting bone formation. Its architecture favors cell attachment and proliferation. In addition, the properties exhibited make Re-Bone a valid alternative to autogenous grafting, preventing the added morbidity of a donor surgical site. Our results were similar with a recent randomized clinical trial published in 2016 to compare histological bone quality and radiographic volume stability in maxillary sinuses

grafted with porcine bone and bovine bone that confirms the validity of the bovine bone when used for sinus lifting [26]. The outcomes of the present bone core histomorphometric study showed a  $35 \pm 1.6\%$  presence of Re-Bone and  $36 \pm 1.6\%$  newly formed bone during the 6-month healing period. This means bone formation with low standard variation between 5 biopsies was not statistically significant. Therefore, 6 months are considered adequate time for Re-Bone maturation before implant placement or the uncovering of implants placed at the same time as grafting.

Obviously, with only 4 grafts and 5 biopsies, the data presented in this study cannot be considered conclusive. However, these results help to set practice parameters that will assure a study with a large number of patients in the future. In conclusion, the findings from the present four case reports support the use of Re-Bone as a bone substitute in maxillary sinus augmentation procedures.

## Competing Interests

The author declares that there are no competing interests.

## Acknowledgments

The author also acknowledges the helpful technical assistance of Dr. Mauro di Berardino (X-ray Technician) in the elaboration of CBCT.

## References

- [1] D. G. Smiler, P. W. Johnson, J. L. Lozada et al., "Sinus lift grafts and endosseous implants. Treatment of the atrophic posterior maxilla," *Dental Clinics of North America*, vol. 36, no. 1, pp. 151–187, 1992.
- [2] G. Iezzi, A. Piattelli, A. Giuliani et al., "Molecular, cellular and pharmaceutical aspects of bone grafting materials and membranes during maxillary Sinus-lift Procedures. Part I: A General Overview," *Current Pharmaceutical Biotechnology*, vol. 18, no. 1, pp. 19–32, 2017.
- [3] M. Del Fabbro, T. Testori, L. Francetti, and R. Weinstein, "Systematic review of survival rates for implants placed in the grafted maxillary sinus," *International Journal of Periodontics and Restorative Dentistry*, vol. 24, no. 6, pp. 565–577, 2004.
- [4] T. dos Anjos, R. de Molon, P. Paim, E. Marcantonio, E. Marcantonio Jr., and R. Faeda, "Implant stability after sinus floor augmentation with deproteinized bovine bone mineral particles of different sizes: a prospective, randomized and controlled split-mouth clinical trial," *International Journal of Oral and Maxillofacial Surgery*, vol. 45, no. 12, pp. 1556–1563, 2016.
- [5] J. N. Kent and M. S. Block, "Simultaneous maxillary sinus floor bone grafting and placement of hydroxylapatite-coated implants," *Journal of Oral and Maxillofacial Surgery*, vol. 47, no. 3, pp. 238–242, 1989.
- [6] J. Jensen, E. K. Simonsen, and S. Sindet-Pedersen, "Reconstruction of the severely resorbed maxilla with bone grafting and osseointegrated implants: a preliminary report," *Journal of Oral and Maxillofacial Surgery*, vol. 48, no. 1, pp. 27–32, 1990.
- [7] G. M. Raghoobar, T. J. Brouwer, H. Reintsema, R. P. Van Oort, J. N. Kent, and M. S. Block, "Augmentation of the maxillary sinus floor with autogenous bone for the placement of endosseous implants: a preliminary report," *Journal of Oral and Maxillofacial Surgery*, vol. 51, no. 11, pp. 1198–1203, 1993.
- [8] F. Alfonsi, V. Borgia, G. Iezzi et al., "Molecular, cellular and pharmaceutical aspects of filling biomaterials during the management of extraction sockets," *Current Pharmaceutical Biotechnology*, vol. 18, no. 1, pp. 64–75, 2017.
- [9] S. A. Small, I. D. Zinner, F. V. Panno, H. J. Shapiro, and J. I. Stein, "Augmenting the maxillary sinus for implants: report of 27 patients," *The International Journal of Oral & Maxillofacial Implants*, vol. 8, no. 5, pp. 523–528, 1993.
- [10] J. K. Tidwell, P. A. Blijdorp, P. J. W. Stoelinga, J. B. Brouns, and F. Hinderks, "Composite grafting of the maxillary sinus for placement of endosteal implants. A preliminary report of 48 patients," *International Journal of Oral and Maxillofacial Surgery*, vol. 21, no. 4, pp. 204–209, 1992.
- [11] P. K. Moy, S. Lundgren, and R. E. Holmes, "Maxillary sinus augmentation: histomorphometric analysis of graft materials for maxillary sinus floor augmentation," *Journal of Oral and Maxillofacial Surgery*, vol. 51, no. 8, pp. 857–862, 1993.
- [12] S. P. Avera, W. A. Stampley, and B. S. McAllister, "Histologic and clinical observations of resorbable and nonresorbable barrier membranes used in maxillary sinus graft containment," *International Journal of Oral and Maxillofacial Implants*, vol. 12, no. 1, pp. 88–94, 1997.
- [13] A. Skoglund, P. Hising, and C. Young, "A clinical and histologic examination in humans of the osseous response to implanted natural bone mineral," *International Journal of Oral and Maxillofacial Implants*, vol. 12, no. 2, pp. 194–199, 1997.
- [14] A. Scarano, G. Pecora, M. Piattelli, and A. Piattelli, "Osseointegration in a sinus augmented with bovine porous bone mineral: histological results in an implant retrieved 4 years after insertion. A case report," *Journal of Periodontology*, vol. 75, no. 8, pp. 1161–1166, 2004.
- [15] L. P. Clergeau, M. Danan, S. Clergeau-Guérithault, and M. Brion, "Healing response to anorganic bone implantation in periodontal intrabony defects in dogs. Part I. Bone regeneration. A microradiographic study," *Journal of Periodontology*, vol. 67, no. 2, pp. 140–149, 1996.
- [16] W. S. Hislop, P. M. Finlay, and K. F. Moos, "A preliminary study into the uses of anorganic bone in oral and maxillofacial surgery," *British Journal of Oral and Maxillofacial Surgery*, vol. 31, no. 3, pp. 149–153, 1993.
- [17] E. M. Pinholt, G. Bang, and H. R. Haanaes, "Alveolar ridge augmentation in rats by Bio-Oss," *Scandinavian Journal of Dental Research*, vol. 99, no. 2, pp. 154–161, 1991.
- [18] H. W. Denissen, K. de Groot, P. C. Makkes, A. van den Hooff, and P. J. Klopper, "Tissue response to dense apatite implants in rats," *Journal of Biomedical Materials Research*, vol. 14, no. 6, pp. 713–721, 1980.
- [19] A. Scarano, F. Carinci, A. Quaranta, G. Iezzi, M. Piattelli, and A. Piattelli, "Correlation between implant stability quotient (ISQ) with clinical and histological aspects of dental implants removed for mobility," *International Journal of Immunopathology and Pharmacology*, vol. 20, no. 1, pp. 33–36, 2007.
- [20] R. Adell, B. Eriksson, U. Lekholm, P. I. Brånemark, and T. Jemt, "Long-term follow-up study of osseointegrated implants in the treatment of totally edentulous jaws," *The International Journal of Oral & Maxillofacial Implants*, vol. 5, no. 4, pp. 347–359, 1990.
- [21] E. Nkenke and F. Stelzle, "Clinical outcomes of sinus floor augmentation for implant placement using autogenous bone or bone substitutes: a systematic review," *Clinical Oral Implants Research*, vol. 20, no. 4, pp. 124–133, 2009.
- [22] A. Scarano, A. Piattelli, G. Iezzi, and G. Varvara, "Spontaneous bone formation on the maxillary sinus floor in association with surgery to remove a migrated dental implant: a case report," *Minerva Stomatologica*, vol. 63, no. 10, pp. 351–359, 2014.
- [23] A. Scarano, M. Degidi, G. Iezzi et al., "Maxillary sinus augmentation with different biomaterials: a comparative histologic and histomorphometric study in man," *Implant Dentistry*, vol. 15, no. 2, pp. 197–207, 2006.
- [24] S. S. Wallace, S. J. Froum, and D. P. Tarnow, "Histologic evaluation of sinus elevation procedure: a clinical report," *International Journal of Periodontics and Restorative Dentistry*, vol. 16, no. 1, pp. 47–51, 1996.
- [25] Z. Schwartz, T. Weesner, S. Van Dijk et al., "Ability of deproteinized cancellous bovine bone to induce new bone formation," *Journal of Periodontology*, vol. 71, no. 8, pp. 1258–1269, 2000.
- [26] J.-S. Lee, H.-K. Shin, J.-H. Yun, and K.-S. Cho, "Randomized clinical trial of maxillary sinus grafting using deproteinized porcine and bovine bone mineral," *Clinical Implant Dentistry and Related Research*, vol. 19, no. 1, pp. 140–150, 2016.

## Research Article

# In Vitro Studies on the Degradability, Bioactivity, and Cell Differentiation of PRP/AZ31B Mg Alloys Composite Scaffold

Jian Zou, Zhongmin Shi, Hongwei Xu, and Xiaolin Li

Shanghai Jiaotong University Affiliated Sixth People's Hospital, Shanghai 200233, China

Correspondence should be addressed to Zhongmin Shi; 18930177323@163.com

Received 2 January 2017; Accepted 16 February 2017; Published 1 March 2017

Academic Editor: Zheng Ren

Copyright © 2017 Jian Zou et al. This is an open access article distributed under the Creative Commons Attribution License, which permits unrestricted use, distribution, and reproduction in any medium, provided the original work is properly cited.

In recent years, more and more methods have been developed to improve the bioactivity of the biodegradable materials in bone tissue regeneration. In present study, we used rat mesenchymal stem cells (rMSCs) to evaluate the outcomes of Mg alloys (AZ31B, Magnesium, and Aluminum) and Platelet-rich plasma (PRP)/Mg alloys on rMSCs biocompatibility and osteogenic differentiation. Water absorption experiments indicated that both bare AZ31B and PRP/AZ31B were capable of absorbing large amounts of water. But the water absorption ratio for PRP/AZ31B was significantly higher than that for bare AZ31B. The degradability experiments implied that both samples degraded at same speed. rMSCs on the surface of AZ31B distributed more and better than those on the AZ31B scaffold. In ALP activity experiment, the activity of rMSCs on the PRP/AZ31B was markedly higher than that on the AZ31B scaffolds on the 7th day and 14th day. qRT-PCR also showed that OPN and OCN were expressed in both samples. OPN and OCN expression in PRP/AZ31B sample were higher than those in bare AZ31B samples. In summary, the in vitro study implied that AZ31B combined with PRP could remarkably improve cell seeding, attachment, proliferation, and differentiation.

## 1. Introduction

How to treat large bone defect effectively is a great challenge for the orthopedic surgeon. More and more osteoconductive scaffolds with good biodegradability and mechanical properties have been developed to repair bone defect. In recent years, more and more research methods have been dedicated to improve the bioactivity of the biodegradable materials in bone tissue regeneration [1]. Nevertheless, these biomaterials have no adequate strength or a good elastic modulus and cannot be used as a load-bearing application. Magnesium (Mg) and its alloys are one kind of fantastic degradable materials, which has excellent biocompatibility, higher strength, applicable mechanical properties, and natural bone density [2–5]. Moreover, Magnesium is one type of essential elements for human being and active bone cells in the human body [4, 6]. This means that Mg can serve as a biodegradable scaffold in the human body and can be dissolved, consumed, or absorbed gradually. It is also proved that Mg can enhance bone cell adhesion and has no negative effect on cell growth or differentiation [5]. However, the main disadvantage of

pure Magnesium as biodegradable scaffold is its insufficient corrosion resistance. Hydrogen gas which is produced rapidly by Magnesium may lead to an alkaline poisoning effect and delay the tissue healing [7]. On the other hand, biomaterial scaffolds should maintain the strength to support the bone and tissue structural integrity before complete degradation in the whole healing process. However, Magnesium has inadequate strength. Though many alloys such as Aluminum and Zinc have been alloyed with Magnesium in order to improve the corrosion resistance and mechanical strength [8–10], most studies reported that the Mg alloys have negative effects on the mineralization and the bone cells' activity in vitro [11, 12].

Platelet-rich plasma (PRP) can be easily obtained from autologous blood. PRP has been used to treat wound healing, bone nonunion, and tendinitis for decades due to high concentration of platelets in plasma after special protocol. PRP, which is always considered as a bioactivator of growth factors and used as bone and tissue biomaterials, is plenty of growth factors, including platelet-derived growth factor (PDGF), transforming growth factor (TGF- $\beta$ ), basic fibroblast growth

factor (bFGF), insulin-like growth factor (IGF), and vascular endothelial growth factor (VEGF) [13–15]. The purpose of using PRP is to create a better healing environment by concentrating the plasma components from an individual's blood and reinjecting into the same individual at the site of injury.

Rat mesenchymal stem cells (rMSCs) are able to differentiate into various types of cells like osteoblasts, lipocytes, and so on [16]. So they are widely used as stem cells and seed cells on biomaterial scaffolds to evaluate the properties in tissue engineering [17–19]. In present study, we used rMSCs as seed cells to evaluate the effects on adhesion, viability, proliferation, and osteogenic differentiation of rMSCs on Mg alloys and PRP/Mg alloys in vitro. The alloys we used in this study are the alloy Mg-3Al-0.8Zn-0.4Mn (AZ31B).

## 2. Materials and Methods

**2.1. Preparation of PRP.** Heart blood was drawn from SD rats weighing 250–300 g. PRP was produced by double centrifugation process as described by Yuan et al. [20]. 4 mL heart blood was obtained from every rat and transferred to the sterile tube. The tubes were then centrifuged in the centrifuge (TD4, Shanghai Kait Instruments Factory, Shanghai, China) at the speed of 2500 rpm for 15 min at 4°C. Then there were three layers in the tube, including erythrocytes at bottom, the platelet-rich plasma at middle, and platelet-poor plasma at top. The erythrocytes at bottom were removed; then the top two layers of plasma were recentrifuged at the speed of 2000 rpm for 15 min. After that, the blood samples were separated into two layers: serum at top and the platelet-rich plasma at bottom. After discarding the top serum, the remaining 0.5 mL of plasma with rich platelets was PRP. Platelet counts of PRP and whole blood were analyzed in the hemacytometer (XS-2100, Mindray, China).

**2.2. Preparation of AZ31B and PRP/AZ31B Scaffold.** The preparation of bare AZ31B and PRP/AZ31B scaffold was under the sterilized condition. 0.4 mL PRP and Porous AZ31B ( $\text{Ø}6 \times 2$  mm) scaffold samples were put into one tube together. The tube was then spun at a speed of 2500 rpm for 5 min at 4°C. Due to the centrifugal force, PRP was mixed well with AZ31B scaffold. In addition, the interior porous structure of AZ31B scaffold were full of PRP. At final, the AZ31B scaffold full of PRP was immersed into a solution containing 0.8 IU thrombin and 1 mL  $\text{CaCl}_2$  for less than 3 seconds. After picking up from mentioned solution, the PRP/AZ31B scaffold was obtained.

**2.3. Scaffold Characterization.** The morphology of the bare AZ31B and PRP/AZ31B scaffold was observed with an scanning electron microscope (SEM, S-3400N, HITACHI, Japan).

**2.4. Water Absorption of AZ31B and PRP/AZ31B.** The original weight of bare AZ31B and PRP/AZ31B samples with sizes of  $\text{Ø}6 \times 2$  mm was measured with an electronic scale (CP64C, OHAUS, America). Then, the samples were immersed in water for 0.5, 6, 12, 18, 24, 30, 36, 42, and 48 h. At the selected

time points, the samples were removed from solution and the weight again was measured. The ratio of water absorption was defined as weight increase/original weight  $\times 100\%$ .

**2.5. Degradation of AZ31 and PRP/AZ31 in the Tris-HCl Solution.** The measurement of original weight of samples has been mentioned.  $\text{Ø}6 \times 2$  mm AZ31B and PRP/AZ31B samples were soaked into the sealed bottles with Tris-HCl solution to evaluate the degradation behavior. The bottles were placed at a temperature of 37°C and a humidity of 50%. The Tris-HCl solution was refreshed every three days. After 4, 14, 28, 42, 56, and 70 days of immersion, the samples were removed from the solution and cautiously washed by distilled water. After that, the samples were dried in an oven at a temperature of 100°C for 8 h and the weight was measured again. The ratio of degradation was defined as weight decrease/original weight  $\times 100\%$ .

**2.6. rMSCs Culture, Seeding, and Attachment.** The AZ31B and PRP/AZ31B scaffold samples were cut into  $\text{Ø}6 \times 3$  mm small columns. The small columns were sterilized by gamma radiation (15 kGy) and prewetted with DMEM solution. Then, they were put into 48-well plates.

rMSCs were purchased from Sciencell Research Laboratories (Carlsbad, CA, USA) and were cultured in differentiation in accordance with manufacturer's protocols. Cells after the four passage were seeded at density of 50,000 cells/mL and were cultured in MEM $\alpha$ . rMSCs were cultured on AZ31B and PRP/AZ31B scaffolds for 7 days before bone differentiation.

**2.7. Cell Morphology, Distribution, and Proliferation.** To observe the inside distribution and penetration of rMSCs, the scaffold samples were cut along the middle line. For confocal laser scanning microscope (CLSM) observation, the samples prepared as described above were rinsed slightly with PBS and were fixed in 4% paraformaldehyde for 10 min. Following pretreatment using Triton X-100 (0.5% v/v) for 5 min, the cells were stained with rhodamine-phalloidin (Sigma) and Hoechst 33258 (Sigma) in the dark for 30 min and 5 min, respectively. The F-actin and cell nuclei were observed by CLSM (LSM 510 meta; Zeiss, Germany). MTT assay (Sigma, USA) was used to assess cell proliferation in accordance with the manufacturer's protocols.

**2.8. ALP Activity.** After 1, 3, 7, and 14 days of culture in osteogenic medium, Para-nitrophenyl phosphate (p-NPP) (Sigma) was used to measure alkaline phosphatase (ALP) activity of rMSCs cells in accordance with the manufacturer's protocols. Measuring the Synergy2 (Biotech) microplate reader of the para-nitrophenol (p-NP) was used to calculate the ALP activity.

**2.9. Quantitative Real-Time Polymerase Chain Reaction (qRT-PCR).** After culturing in differentiation media, RNA extraction was performed using the TRIZOL reagent (Invitrogen) in accordance with the manufacturer's protocols. The concentration and purity of RNA were calculated by measuring

TABLE 1: qRT-PCR primer sequences used for mouse MSC.

	Forward primer (5' - 3')	Reverse primer (5' - 3')
GAPDH	GATTTGGCCGTATCGGAC	GAAGACGCCAGTAGACTC
Osteocalcin	CATGCCAGGTCACCAAAAT	GCCCCAAGGCCGCTTCTT
Osteopontin	ACTCAGATGCTGTAGCCA	TTTCATTGGAGTTGCTTG

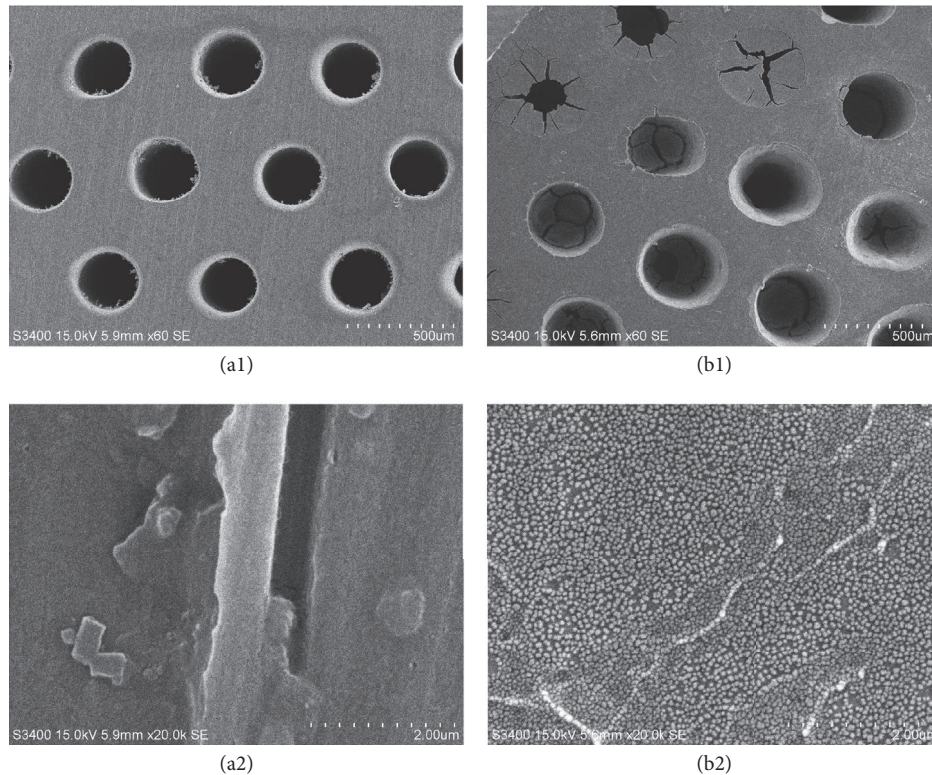


FIGURE 1: The surface morphologies of the bare AZ31B (a1, a2) and PRP/AZ31B (b1, b2) scaffolds.

the absorbance at 260 and 280 nm. The reverse transcription kit (Sciencell Research Laboratories, Carlsbad, CA, USA) was used to perform reverse transcription in accordance with the manufacturer's instructions. Table 1 shows the Primers of mouse GAPDH, osteopontin, and osteocalcin in the qRT-PCR experiments.

**2.10. Statistical Analysis.** All quantitative data were displayed as the mean  $\pm$  standard deviation ( $M \pm SD$ ) and analyzed with SPSS statistical software program (version 12.0.0, SPSS, IBM). Wilcoxon rank sum test was carried out to determine the significance. Significant differences were defined as  $P$  value less than 0.05.

### 3. Results

**3.1. Material Characterization.** The platelet concentrations of whole blood and PRP were  $(0.38 \pm 0.04) \times 10^9/\text{mL}$  and  $(1.21 \pm 0.06) \times 10^9/\text{mL}$ , respectively. It showed that the platelet concentration of PRP was almost 3.2 times that of the whole blood. The morphologies of bare AZ31B and PRP/AZ31B scaffold were given in Figure 1. The bare AZ31B was highly

porous with regular distributed macropores with an average diameter of 300  $\mu\text{m}$  (Figures 1(a1) and 1(a2)). Abundant PRP sheets were filled to the macropores of the AZ31B scaffold after the centrifugation. Large quantities of platelets were observed on the surface of AZ31B (Figures 1(b1) and 1(b2)).

**3.2. Water Absorption and Degradability.** Figure 2(a) showed the water absorption ratio of AZ31B and PRP/AZ31B samples at different time points. Both AZ31B and PRP/AZ31B continued to absorb water as time goes by. The water absorption ratios of bare AZ31B after soaking in water for 0.5 h and 12 h were 26% and 45%, respectively. The ratios of PRP/AZ31B were 49% and 68%. These results proved that both AZ31B and PRP/AZ31B were capable of absorbing large amounts of water. But the water absorption ratio for PRP/AZ31B was significantly higher than that for bare AZ31B.

The results of degradation behavior of AZ31B and PRP/AZ31B were different to those of water absorption. After immersion in Tris-HCl solution, both samples showed weight loss over time. The weight loss curve in Figure 2(b) showed that the weight loss ratio of the AZ31B was no different to that of PRP/AZ31B at any selected time point. The weight loss ratio

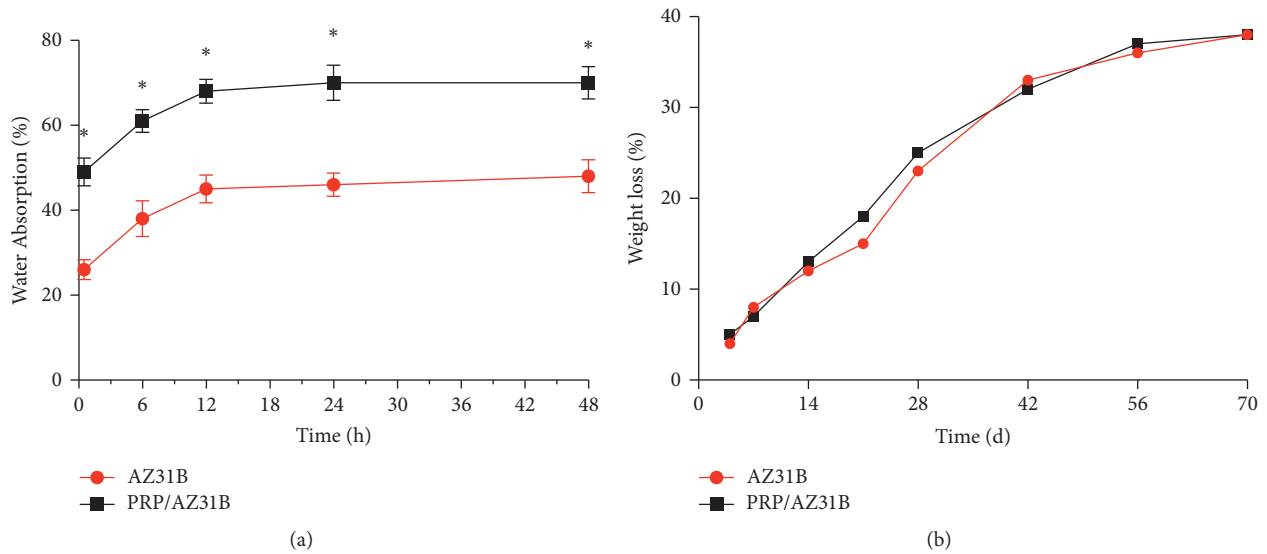


FIGURE 2: Water absorption (a) and weight loss (b) of AZ31B and PRP/AZ31B soaked in Tris-HCl solution ( $n = 6$ ). \* $P < 0.05$ .

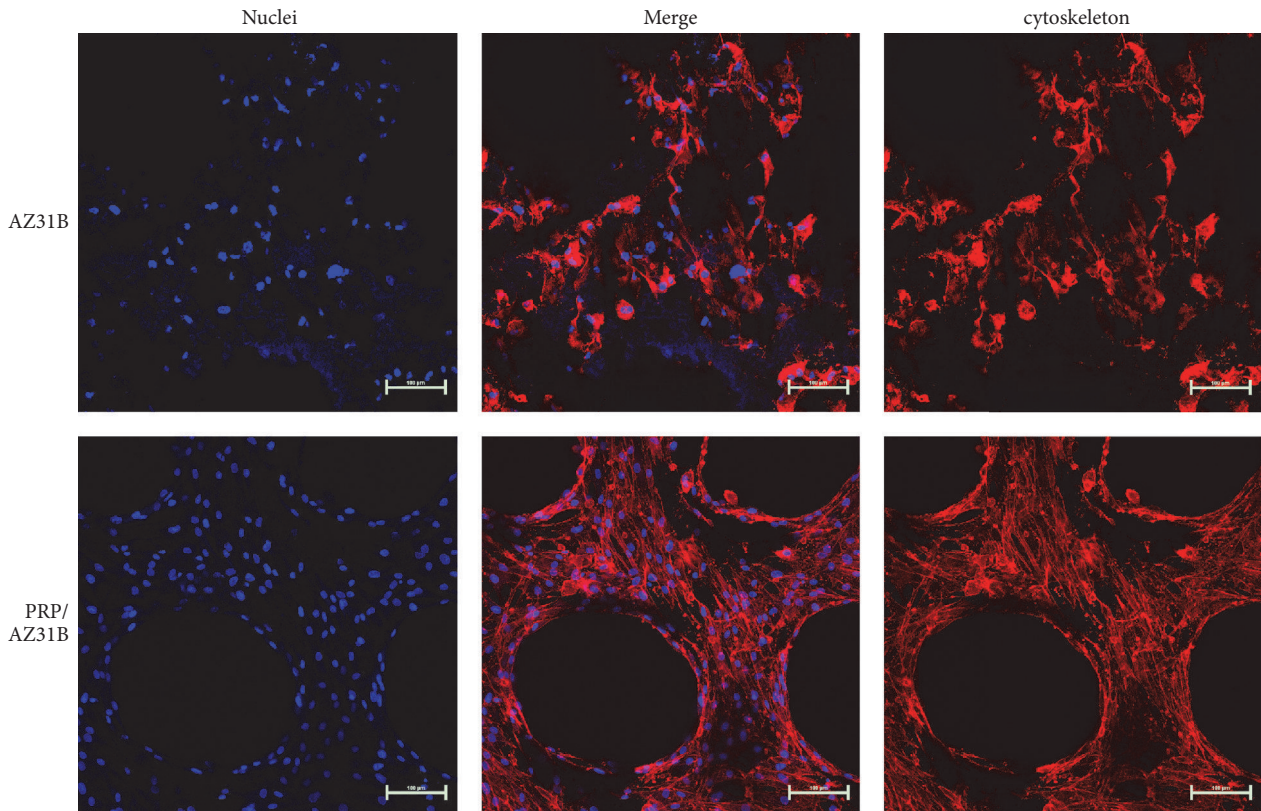


FIGURE 3: The CLSM images of cell morphology on both scaffolds after 7 days of incubation.

in both samples was less than 40 wt% at 70 days. These results implied that both PRP/AZ31B and AZ31B degraded at same speed.

**3.3. Cell Morphology and Distribution.** Figure 3 demonstrated the CLSM photographs of rMSCs which had been cultured for 8 days on the bare AZ31B and PRP/AZ31B

scaffold. The cells distributed regularly on the cut surface of AZ31B and PRP/AZ31B scaffold. More rMSCs were observed on the surface of PRP/AZ31B scaffold in comparison to those on AZ31B. Moreover, the rMSCs on the PRP/AZ31B scaffold distribute better than those on the bare AZ31B scaffold. There was no cell spread in the macropores in both samples. These results implied that the rMSCs were able to migrate to the

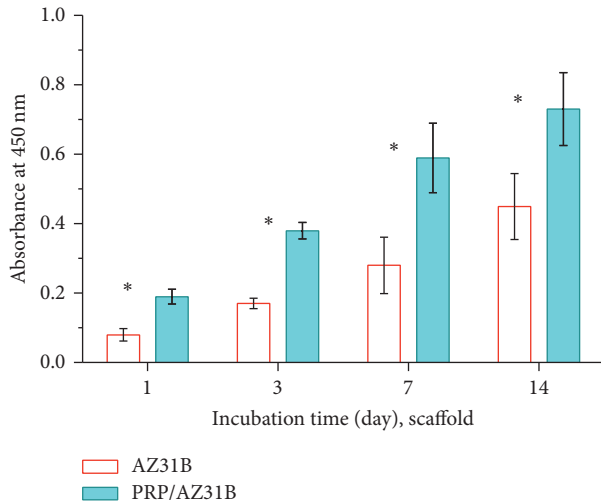


FIGURE 4: The rMSCs proliferation on the AZ31B and PRP/AZ31B scaffolds ( $n = 6$ ). \* $P < 0.05$ .

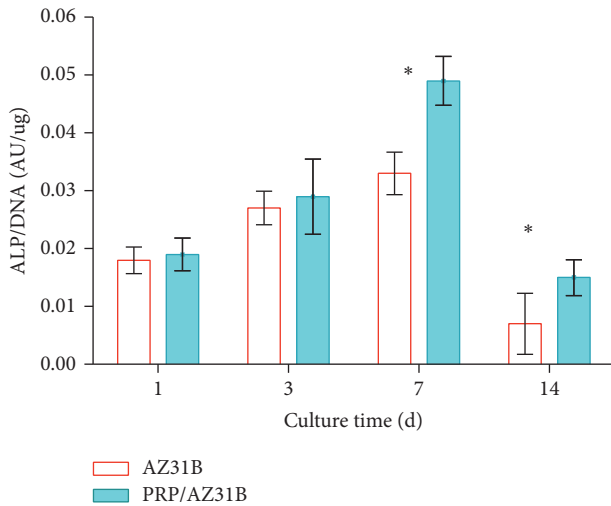


FIGURE 5: The ALP activity of rMSCs cultured on the AZ31B and PRP/AZ31B scaffolds ( $n = 6$ ). \* $P < 0.05$ .

inside of the scaffold smoothly as the culture time goes by. Plenty of PRP did not compromise the cell infiltration but improved the cell proliferation.

**3.4. Cell Proliferation.** The cell proliferation on both AZ31B and PRP/AZ31B scaffolds at 1, 3, 7, and 14 d was manifested in Figure 4. On the first day of culture, the rMSCs on the PRP/AZ31B scaffold were apparently more than those on the AZ31B scaffold. As the time goes by, the cells on both scaffolds proliferated well. But comparing with the cells on the AZ31B, those on PRP/AZ31B were significantly more ( $P < 0.05$ ).

**3.5. ALP Activity.** Figure 5 displayed the ALP activity of rMSCs which were cultured on both AZ31B and PRP/AZ31B scaffolds. On the 1st and 3rd day, the ALP activity was not different in AZ31B and PRP/AZ31B scaffolds. On the 7th

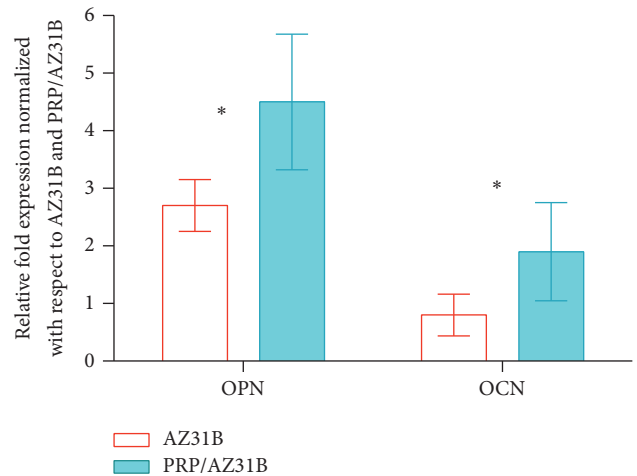


FIGURE 6: qRT-PCR gene expression data show the expression of osteoprotein (OPN) and osteocalcin (OCN) of rMSCs cultured on coated samples normalized with respect to cells cultured on bare AZ31B and AZ31B/PRP. \* $P < 0.05$ .

day and 14th day, the ALP activity of the PRP/AZ31B was markedly higher than that of the AZ31B scaffolds ( $n = 6$ ,  $P < 0.05$ ). The curve also demonstrated that ALP activity in both samples increased from the 1st day to 7th day and then decreased to the 14th day.

**3.6. qRT-PCR.** qRT-PCR was performed after the rMSCs were cultured in differentiation media for 14 days. Figure 6 showed that both OPN and OCN levels in PRP/AZ31B samples were significantly higher than those in bare AZ31B sample ( $P < 0.05$ ).

#### 4. Discussion

In the past few decades, traditional materials were widely used in orthopedic surgeries. However, Mg and Mg alloys nowadays were considered to be newly developed components of biomaterial scaffold for tissue engineering and prevail gradually. Recent reports have suggested that Mg and Mg alloys are accepted and used as biodegradable osteoconductive scaffold owing to their desirable biocompatibility and higher strength. In our current study, a PRP/Mg alloys composite scaffold with unidirectional pores was developed to evaluate the in vitro efficacy on rMSCs adhesion, viability, proliferation, and osteogenic differentiation.

PRP is a plasma enriched with platelet and contains a variety of growth factors including TGF- $\beta$ , PDGF, VEGF, BMPs, and cytokines [21] and therefore plays a crucial role in osteogenesis, angiogenesis, and soft tissue healing stimulation. Furthermore, various concentrations of growth factors can be detected once the platelet concentration of PRP is controlled [22]. Once the cells are cultured in the environment with PRP, the fibrin and a variety of growth factors released from platelets have synergistic effect on cells' behavior. Namazi and Kayedi [23] indicated PRP may have a significant therapeutic effect on pain relief at rest and

alleviate function difficulties including specific and usual activities in patients with scaphoid fractures in a study with 14 patients enrolled. Ghaffarpasand et al. [24] determined that application of PRP along with autologous bone graft in the site of nonunion of long bone after intramedullary nailing or ORIF resulted in high cure rate, short duration of healing, low rate of limb shortening, and mild postoperative pain. Malhotra et al. [25] injected autologous platelet-rich plasma to 94 long bone nonunion patients and found that 82 patients got united at the end of 4 months. They demonstrated that PRP was a safe and effective method for nonunion therapy. In this study, the PRP/AZ31B scaffold not only prevented the cells from peeling off the scaffold, but also provided more bioactive surface areas to promote cell adhesion. Therefore, the cell seeding of the scaffold was markedly improved. The cell attachment, proliferation, and differentiation on the PRP/Z31B scaffold notably ameliorated as well when compared with those of bare AZ31B scaffold due to synergistic effect of both fibrin and other growth factors released from the platelets.

In present study, the water absorption experiment showed that large amount of water was absorbed in both AZ31B and PRP/AZ31B with the water absorption ratio of the PRP/AZ31B (57%) almost twice higher than that of bare AZ31B scaffold (33%). The infiltration of PRP into AZ31B significantly increased in water absorption test, suggesting that PRP had much specific hydrophilic surface area and enhanced alloy's capacity to absorb water. These results inferred that the PRP/AZ31B, which had specific surface and remarkable rapid and efficient capability of water absorption, could be used as a biomaterial scaffold to load target drugs, cells, and other biomolecules with therapeutic effect [26]. As candidate biomaterials for bone repair and remodeling, these implants and scaffolds must feature with appropriate degradable property and can be gradually replaced by new bone tissue in *in vivo* models [27]. The weight loss of both AZ31B and PRP/AZ31B in Tris-HCl solution increased with incubation time and reached up to 38% after 70 days of incubation. Little variance of degradability was found between two samples. These results suggested that PRP/AZ31B could not only improve the cell adhesion and proliferation, but also have no adverse effect on degradability. Bone tissue regeneration is attributable to PRP/AZ31B's favorable biochemical properties to a large extent. [28].

In our current study, the proliferation of rMSCs on the surfaces of both PRP/AZ31B and AZ31B was evaluated by MTT assay. The results showed that PRP/AZ31B was in favor of the rMSCs proliferation at every time point, indicating that PRP/AZ31B with good cytocompatibility had no toxicity for cell growth and proliferation. In addition, ALP activity, which is one of the most widely used markers for detection of osteoblastic differentiation, is also a generally used to measure the osteoblast differentiation in the early stage [29]. The results in our study revealed that the ALP activity of the cells on both samples was time-dependent and ALP activity in PRP/AZ31B was higher than that in bare AZ31B sample at the time points of 7 and 14 d. These results also indicated that the PRP/AZ31B scaffolds could improve rMSCs differentiation to some extent. The reasonable explanation was that PRP's

infiltration into AZ31B could enhance cell proliferation and differentiation after 3 days' culture while high concentration of PRP and multipore structure of AZ31B provide more growth factors and therefore facilitated cell growth as seen in the experiments.

The cytocompatibility is a very critical criterion to assess cell spread on the surface of the substrate [30]. In our study, the results suggested that the rMSCs cells extended and spread well on the bare AZ31B and PRP/AZ31B surface and formed tight attachment to substrate after 24 h of culture, indicating that both AZ31B and PRP/AZ31B had no adverse effect on cell morphology and viability. Obviously, the process of cells' spread on PRP/AZ31B surface was much faster than that on bare AZ31B surface due to complex effect of a variety of growth factors of PRP. Therefore, our results suggested that PRP/AZ31B with plenty of bioactive factors was favorable for cell attachment, growth, and spread with good cytocompatibility. PRP/AZ31B may play a role in promoting new bone formation and accelerating surrounding tissue healing process when implanted *in vivo*.

There is no new concerned toxicity when bare AZ31B and PRP/AZ31B are applied to support rMSCs proliferation. Osteocalcin (OCN) and osteopontin (OPN), which were encoded by osteogenic genes, were studied on both samples to investigate the capability of AZ31B and PRP/AZ31B to promote the differentiation of rMSCs. OPN, encoded by SPPI gene, is a noncollagenous, extracellular structural protein which is well-known to accelerate wound healing and bone mineralization [31]. Because OPN has played an important role in mineralization and is able to adjust cell attachment and adhesion on the biomaterials, it has been used as biomarker for osteogenic differentiation in the early stage [32, 33]. OCN, which is secreted by osteoblasts and plentiful in bone, is the other biomarker for osteogenic differentiation and metabolic regulation. In contrast, OCN is a late-stage biomarker [34]. It has been proved that high serum OCN levels are correlated with high bone mineral density (BMD) in adults. Many researches stated that osteocalcin is used as a preliminary biomarker to evaluate the efficacy of antiosteoporosis drug. In our current study, qRT-PCR was performed after 14 days of cell culture. Though high levels of OPN and OCN were expressed in both samples as anticipated, OPN and OCN expressions in PRP/AZ31B sample were higher than those in bare AZ31B samples. The results revealed that PRP/AZ31B may apply better biochemical microenvironment for osteogenic differentiation, resulting in rapid progress of soft tissue healing and bone remodeling.

## 5. Conclusion

In this study, we developed a porous PRP/My alloys composite scaffold to evaluate the effects on rMSCs adhesion, viability, proliferation, and osteogenic differentiation. Water absorption experiments indicated that both bare AZ31B and PRP/AZ31B were capable of absorbing large amounts of water. But the water absorption ratio for PRP/AZ31B was significantly higher than that for bare AZ31B. The degradability experiments implied that both samples degraded at same speed. rMSCs on the surface of AZ31B distributed more

and better than those on the AZ31B scaffold. In ALP activity experiment, the ALP activity of the PRP/AZ31B was markedly higher than that of the AZ31B scaffolds on the 7th day and 14th day. qRT-PCR also showed that OPN and OCN were expressed in both samples. OPN and OCN expressions in PRP/AZ31B sample were higher than those in bare AZ31B samples. In summary, the *in vitro* study implied that AZ31B combined with PRP could remarkably improve cell seeding, attachment, proliferation, and differentiation.

## Competing Interests

All authors state that they have no conflict of interests.

## References

- [1] E. Pişkin, "Biodegradable polymers as biomaterials," *Journal of Biomaterials Science. Polymer edition*, vol. 6, no. 9, pp. 775–795, 1995.
- [2] F. Witte, N. Hort, C. Vogt et al., "Degradable biomaterials based on magnesium corrosion," *Current Opinion in Solid State & Materials Science*, vol. 12, no. 5–6, pp. 63–72, 2008.
- [3] L. Xu, F. Pan, G. Yu, L. Yang, E. Zhang, and K. Yang, "In vitro and in vivo evaluation of the surface bioactivity of a calcium phosphate coated magnesium alloy," *Biomaterials*, vol. 30, no. 8, pp. 1512–1523, 2009.
- [4] F. Witte, V. Kaese, H. Haferkamp et al., "In vivo corrosion of four magnesium alloys and the associated bone response," *Biomaterials*, vol. 26, no. 17, pp. 3557–3563, 2005.
- [5] M. P. Staiger, A. M. Pietak, J. Huadmai, and G. Dias, "Magnesium and its alloys as orthopedic biomaterials: a review," *Biomaterials*, vol. 27, no. 9, pp. 1728–1734, 2006.
- [6] H. Hermawan and D. Mantovani, "Degradable metallic biomaterials: the concept, current developments and future directions," *Minerva Biotechnologica*, vol. 21, no. 4, pp. 207–216, 2009.
- [7] E. D. McBride, "Absorbable metal in bone surgery: a further report on the use of magnesium alloys," *Journal of the American Medical Association*, vol. 111, no. 27, pp. 2464–2467, 1938.
- [8] H. R. Bakhsheshi-Rad, E. Hamzah, H. T. Low et al., "Fabrication of biodegradable Zn-Al-Mg alloy: mechanical properties, corrosion behavior, cytotoxicity and antibacterial activities," *Materials Science and Engineering: C*, vol. 73, pp. 215–219, 2017.
- [9] S. A. Salman, K. Kuroda, and M. Okido, "Preparation and characterization of hydroxyapatite coating on AZ31 Mg alloy for implant applications," *Bioinorganic Chemistry and Applications*, vol. 2013, Article ID 175756, 6 pages, 2013.
- [10] Y. Jang, B. Collins, J. Sankar, and Y. Yun, "Effect of biologically relevant ions on the corrosion products formed on alloy AZ31B: An improved understanding of magnesium corrosion," *Acta Biomaterialia*, vol. 9, no. 10, pp. 8761–8770, 2013.
- [11] M. Rodriguez, A. J. Felsenfeld, and F. LLach, "Aluminum administration in the rat separately affects the osteoblast and bone mineralization," *Journal of Bone and Mineral Research*, vol. 5, no. 1, pp. 59–67, 1990.
- [12] W. G. Goodman, "Experimental aluminum-induced bone disease: studies in vivo," *Kidney International. Supplement*, vol. 18, pp. S32–S36, 1986.
- [13] J. Alsousou, M. Thompson, P. Harrison, K. Willett, and S. Franklin, "Effect of platelet-rich plasma on healing tissues in acute ruptured Achilles tendon: a human immunohistochemistry study," *The Lancet*, vol. 385, article no. S19, 2015.
- [14] H. Rajabi, H. Sheikhan Shahin, M. Norouzian, D. Mehrabani, and S. Dehghani Nazhvani, "The healing effects of aquatic activities and allogenic injection of Platelet-Rich Plasma (PRP) on injuries of achilles tendon in experimental rat," *World Journal of Plastic Surgery*, vol. 4, no. 1, pp. 66–73, 2015.
- [15] E. Rubio-Azpeitia, P. Sánchez, D. Delgado, and I. Andia, "Three-dimensional platelet-rich plasma hydrogel model to study early tendon healing," *Cells Tissues Organs*, vol. 200, no. 6, pp. 394–404, 2015.
- [16] M. F. Pittenger, A. M. Mackay, S. C. Beck et al., "Multilineage potential of adult human mesenchymal stem cells," *Science*, vol. 284, no. 5411, pp. 143–147, 1999.
- [17] Y. Huang, X. Jin, X. Zhang et al., "In vitro and in vivo evaluation of akermanite bioceramics for bone regeneration," *Biomaterials*, vol. 30, no. 28, pp. 5041–5048, 2009.
- [18] H. Sun, C. Wu, K. Dai, J. Chang, and T. Tang, "Proliferation and osteoblastic differentiation of human bone marrow-derived stromal cells on akermanite-bioactive ceramics," *Biomaterials*, vol. 27, no. 33, pp. 5651–5657, 2006.
- [19] R. F. Service, "Tissue engineers build new bone," *Science*, vol. 289, no. 5484, pp. 1498–1500, 2000.
- [20] T. Yuan, S.-C. Guo, P. Han, C.-Q. Zhang, and B.-F. Zeng, "Applications of leukocyte- and platelet-rich plasma (L-PRP) in trauma surgery," *Current Pharmaceutical Biotechnology*, vol. 13, no. 7, pp. 1173–1184, 2012.
- [21] R. Landesberg, M. Roy, and R. S. Glickman, "Quantification of growth factor levels using a simplified method of platelet-rich plasma gel preparation," *Journal of Oral and Maxillofacial Surgery*, vol. 58, no. 3, pp. 297–300, 2000.
- [22] A. Breen, T. O'Brien, and A. Pandit, "Fibrin as a delivery system for therapeutic drugs and biomolecules," *Tissue Engineering—Part B: Reviews*, vol. 15, no. 2, pp. 201–214, 2009.
- [23] H. Namazi and T. Kayedi, "Investigating the effect of intra-articular platelet-rich plasma injection on union: pain and function improvement in patients with scaphoid fracture," *Journal of Hand and Microsurgery*, vol. 8, no. 3, pp. 140–144, 2016.
- [24] F. Ghaffarpasand, M. Shahrezaei, and M. Dehghankhalili, "Effects of platelet rich plasma on healing rate of long bone non-union fractures: a randomized double-blind placebo controlled clinical trial," *Bulletin of Emergency & Trauma*, vol. 4, no. 3, pp. 134–140, 2016.
- [25] R. Malhotra, V. Kumar, B. Garg et al., "Role of autologous platelet-rich plasma in treatment of long-bone nonunions: a prospective study," *Musculoskeletal Surgery*, vol. 99, no. 3, pp. 243–248, 2015.
- [26] G. Liu, C. Zhu, J. Xu et al., "Thermo-responsive hollow silica microgels with controlled drug release properties," *Colloids and Surfaces B: Biointerfaces*, vol. 111, pp. 7–14, 2013.
- [27] J. Li, Y. Song, S. Zhang et al., "In vitro responses of human bone marrow stromal cells to a fluoridated hydroxyapatite coated biodegradable Mg-Zn alloy," *Biomaterials*, vol. 31, no. 22, pp. 5782–5788, 2010.
- [28] S. Lee, H.-S. Yun, and S.-H. Kim, "The comparative effects of mesoporous silica nanoparticles and colloidal silica on inflammation and apoptosis," *Biomaterials*, vol. 32, no. 35, pp. 9434–9443, 2011.
- [29] C.-W. Hsu, S. Liu, E. Hsu, and J. O. Hollinger, "Inhibition of rhBMP-2-induced ALP activity by intracellular delivery of SMURF1 in murine calvarial preosteoblast cells," *Journal of Biomedical Materials Research. A*, vol. 102, no. 11, pp. 4037–4043, 2014.

- [30] J. Sun, Y. Zhu, L. Meng et al., “Electrophoretic deposition of colloidal particles on Mg with cytocompatibility, antibacterial performance, and corrosion resistance,” *Acta Biomaterialia*, vol. 45, pp. 387–398, 2016.
- [31] C. M. Giachelli and S. Steitz, “Osteopontin: a versatile regulator of inflammation and biomineralization,” *Matrix Biology*, vol. 19, no. 7, pp. 615–622, 2000.
- [32] J. Sodek, B. Ganss, and M. D. McKee, “Osteopontin,” *Critical Reviews in Oral Biology and Medicine*, vol. 11, no. 3, pp. 279–303, 2000.
- [33] E. Kärner, C.-M. Bäckesjö, J. Cedervall, R. V. Sugars, L. Ährlund-Richter, and M. Wendel, “Dynamics of gene expression during bone matrix formation in osteogenic cultures derived from human embryonic stem cells in vitro,” *Biochimica et Biophysica Acta (BBA)—General Subjects*, vol. 1790, no. 2, pp. 110–118, 2009.
- [34] Q. Q. Hoang, F. Sicheri, A. J. Howard, and D. S. C. Yang, “Bone recognition mechanism of porcine osteocalcin from crystal structure,” *Nature*, vol. 425, no. 6961, pp. 977–980, 2003.

## Research Article

# In Vitro and In Vivo Evaluation of Commercially Available Fibrin Gel as a Carrier of Alendronate for Bone Tissue Engineering

Beom Su Kim,<sup>1,2</sup> Feride Shkemi,<sup>3</sup> and Jun Lee<sup>2,3</sup>

<sup>1</sup>Bonecell Biotech. Inc., Dunsan-dong, Seo-gu, Daejeon 602-830, Republic of Korea

<sup>2</sup>Wonkwang Bone Regeneration Institute, Wonkwang University, Iksan 570-749, Republic of Korea

<sup>3</sup>Department of Oral & Maxillofacial and Surgery, Wonkwang University Daejeon Dental Hospital, Seo-gu, Daejeon 302-120, Republic of Korea

Correspondence should be addressed to Jun Lee; [omslee@wku.ac.kr](mailto:omslee@wku.ac.kr)

Received 20 October 2016; Revised 7 December 2016; Accepted 19 December 2016; Published 22 January 2017

Academic Editor: Changmin Hu

Copyright © 2017 Beom Su Kim et al. This is an open access article distributed under the Creative Commons Attribution License, which permits unrestricted use, distribution, and reproduction in any medium, provided the original work is properly cited.

Alendronate (ALN) is a bisphosphonate drug that is widely used for the treatment of osteoporosis. Furthermore, local delivery of ALN has the potential to improve the bone regeneration. This study was designed to investigate an ALN-containing fibrin (fibrin/ALN) gel and evaluate the effect of this gel on both in vitro cellular behavior using human mesenchymal stem cells (hMSCs) and in vivo bone regenerative capacity. Fibrin hydrogels were fabricated using various ALN concentrations ( $10^{-7}$ – $10^{-4}$  M) with fibrin glue and the morphology, mechanical properties, and ALN release kinetics were characterized. Proliferation and osteogenic differentiation of and cytotoxicity in fibrin/ALN gel-embedded hMSCs were examined. In vivo bone formation was evaluated using a rabbit calvarial defect model. The fabricated fibrin/ALN gel was transparent with Young's modulus of ~13 kPa, and these properties were not affected by ALN concentration. The in vitro studies showed sustained release of ALN from the fibrin gel and revealed that hMSCs cultured in fibrin/ALN gel showed significantly increased proliferation and osteogenic differentiation. In addition, microcomputed tomography and histological analysis revealed that the newly formed bone was significantly enhanced by implantation of fibrin/ALN gel in a calvarial defect model. These results suggest that fibrin/ALN has the potential to improve bone regeneration.

## 1. Introduction

Bone defects occur as a result of various conditions such as tumors, trauma, disease, and fracture. Although small defects have the capacity to self-regenerate, large-sized defects do not heal well. To enhance bone repair and reconstruction, the use of osteogenic growth factors or cytokines such as bone morphogenetic protein-2 (BMP-2) has been explored [1, 2].

Recently, several studies have suggested that alendronate (ALN), one of the bisphosphonates (BPs), can enhance the osteogenesis of osteoblasts and mesenchymal stem cells (MSCs) [3–5]. BPs are well known potential antiresorptive drugs and are widely used in the treatment of metabolic bone diseases [6]. BPs are classified into two main groups: nonnitrogen-containing BPs, which produce

nonhydrolyzable analogs of ATP that are toxic to cells, and nitrogen-containing BPs, which are more potent drugs that inhibit the mevalonate pathway and therefore indirectly induce osteoclast apoptosis [7, 8].

Among the BPs, alendronate (ALN) is one of the most potent nitrogen-containing BPs and is commonly used for treating osteoporosis [9]. The mechanism of ALN is attributed to the inhibition of osteoclast precursor cells through suppression of farnesyl diphosphate synthase, a key enzyme of the mevalonate pathway [10]. A previous study reported that ALN stimulates the proliferation and osteoblast differentiation of human bone marrow-derived MSCs [3]. Furthermore, Toker et al. reported that locally implanted ALN promoted bone formation in a rat critical-sized calvarial defect model [11]. However, ALN easily dissolves in aqueous

conditions because of its high hydrophilicity, and uncontrolled burst release can lead to side effects. Therefore, to achieve efficient osteogenesis, proper ALN delivery carriers are required for implantation at bone defect sites.

Fibrin gel consists of fibrinogen and thrombin components isolated from human plasma. When fibrinogen is activated by thrombin, it is converted into a fibrin monomeric biopolymer and forms a fibrin gel [12]. The fibrin gel is frequently used as a drug delivery system [13] or scaffold material [14] because it is biocompatible and naturally biodegrades, and it is possible to vary the release profile from hours to weeks [15]. Furthermore, fibrin promotes osteoblast differentiation and accelerates new bone formation from osteoblasts located near the bone membrane [16, 17]. However, the biocompatibility and *in vivo* bone healing properties of an ALN-loaded fibrin gel system have not been sufficiently studied.

In this study, we fabricated an ALN-loaded fibrin gel and the mechanical properties and release pattern were characterized. The biocompatibility was evaluated using human MSCs *in vitro*. The *in vivo* bone formation capacity of the fibrin/ALN gel was evaluated using a rabbit calvarial defect model.

## 2. Materials and Methods

**2.1. Preparation ALN-Containing Fibrin Gel.** To fabricate ALN-containing fibrin gel, ALN dissolved fibrinogen solution was polymerized using thrombin. Figure 1 shows a schematic diagram of preparation the ALN embedded fibrin gel to improve bone regeneration. Briefly, ALN was dissolved in phosphate buffered saline (PBS) at various concentrations ( $10^{-7}$ – $10^{-4}$  M). Fibrinogen powder (Greenplast; Greencross, Seoul, Korea) was dissolved in the prepared ALN solution and poured into a silicon mold. To induce polymerization, thrombin solution was added and blended. The composite mixture was polymerized at 37°C for 10 min. Fibrin gels were constructed so that the final concentrations were 20 mg/mL fibrinogen and 2 IU/mL thrombin.

**2.2. Mechanical Strength.** We measured Young's moduli of fibrin/ALN gel constructs prepared with various concentrations of ALN. The fabricated fibrin/ALN gels were loaded between two flat plates and compressed at a rate of 0.5 mm/min using an Instron 3345 (Norwood, MA, USA). Young's moduli were determined based on the 0–5% linear region of the stress-strain curve [18].

**2.3. *In Vitro* ALN Release.** The fibrin/ALN gel samples were soaked in 1 mL PBS (pH 7.4). At predetermined time intervals, 0.1 mL of the sample media was collected and replaced with fresh solution. ALN concentration was determined spectrophotometrically at 293 nm via complex formation with Fe(III) ions, as previously described [19].

**2.4. Cell Culture.** To evaluate biocompatibility, alveolar bone marrow-derived MSCs obtained from Professor You were utilized (Wonkwang University, Iksan, Korea). The cells were cultured in  $\alpha$ -MEM (Invitrogen, Carlsbad, CA) containing

10% fetal bovine serum (FBS; Invitrogen) and 1% penicillin/streptomycin at 37°C, 5% CO<sub>2</sub>, and 100% humidity. The hMSCs were passaged 3–6 times.

**2.5. Preparation of Cells Embedded in ALN-Loaded Fibrin Gel Constructs.** Human mesenchymal stem cells (hMSCs) were dissociated using a 0.05% trypsin/EDTA solution. An aliquot containing  $2 \times 10^4$  cells was resuspended in 100  $\mu$ L of fibrinogen only or ALN-containing fibrinogen solutions. The suspensions were then poured into silicone molds. Polymerization was induced by adding thrombin solution (20  $\mu$ L, 2 IU/mL) with mixing. The constructs were briefly washed with PBS to remove residual thrombin and the cell-containing gels were placed into 24-well plates and cultured as described above.

**2.6. Cell Proliferation Assay.** The proliferation of cells embedded in fibrin/ALN gel was analyzed using CellTiter96® Aqueous One solution (Promega, Madison, WI). Briefly, after 3 days of cultivation, 50  $\mu$ L MTS reagent was added to each well and incubated for 2 h. Then, 100  $\mu$ L supernatant was removed and the absorbance at 490 nm was measured using a SpectraMAX M3 plate reader (Molecular Devices, Sunnyvale, CA).

**2.7. Viability and Cytotoxicity Assay.** After 3 days of cultivation, hMSC-embedded gels were soaked in Dulbecco's phosphate buffered saline (DPBS) for 30 min to remove phenol red and serum. Staining was performed in dark conditions for 30 min using a Live/Dead® Viability/Cytotoxicity kit (Molecular Probes, UK). Calcein acetoxymethyl (calcein AM, 0.05%) stains viable cells green and ethidium homodimer-1 (EthD-1, 0.2%) stains the nuclei of nonviable cells red. The stained samples were examined under an inverted fluorescence microscope (DM IL LED Fluo; Leica Microsystems, Wetzlar, Germany).

**2.8. Alkaline Phosphatase (ALP) Activity.** ALP activity was measured using a *p*-nitrophenyl phosphate-based colorimetric assay. Briefly, the cell-embedded gels were cultured each gel. After 7 days of cultivation, gel constructs were homogenized in 100  $\mu$ L Tris (pH 8.0) buffer and lysed via ultrasonication for 5 min. The supernatant was then collected for the ALP activity assay using *p*-nitrophenylphosphate (*p*-NPP) as a substrate, as described previously [20].

**2.9. Calcium Accumulation Assay.** Calcium accumulation was assayed by alizarin red S staining. Embedded cells were cultured for 2 weeks during which medium was replaced every two days. The gel encapsulated cells were fixed with ice-cold 70% ethanol for one hour and ethanol was removed. Next, alizarin red S staining solution (40 mM, pH 4.2) was added and the cells were incubated for 30 min. The stained samples were washed five times for 30 min with distilled water and stained portions were photographed with a digital camera (EOS 500D; Canon, Tokyo, Japan). Quantification of calcium accumulation was carried out by chopping hydrogel samples into small pieces, and stained portions were solubilized using 10% (w/v) cetylpyridinium chloride in

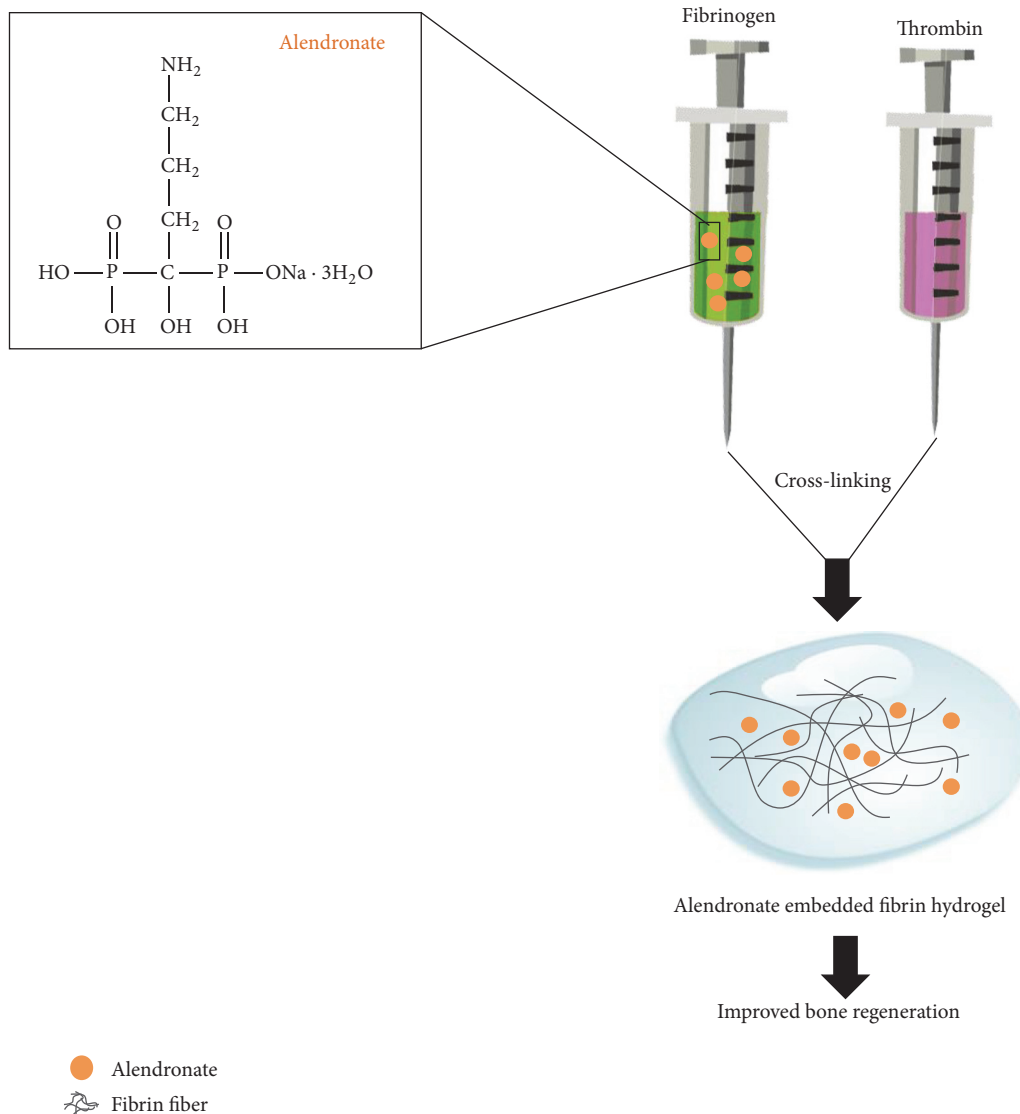


FIGURE 1: Schematic diagrams of the alendronate embedded fibrin hydrogel to improve bone regeneration.

10 mM sodium phosphate buffer (pH 7.0) and the absorbance measured at 562 nm.

**2.10. Real-Time Polymerase Chain Reaction.** After 7 days of cultivation, total mRNA was extracted from cells embedded in fibrin gel using an RNA isolation kit (Ribospin, GeneAll, Seoul, Korea) according to the manufacturer's instructions. PCR was performed using a TaqMan Universal PCR Master Mix, TaqMan primers, and probe sets (Applied Biosystems, Carlsbad, CA, USA) specifically targeting collagen type I (*Col1A1*; Hs00164004\_m1), runt related transcription factor (*Runx2*; Hs00231692\_m1), osteocalcin (*OCN*; Hs01587814\_g1), and *18S* (Hs99999901\_s1). The *18S* rRNA gene was used as an internal standard. The relative expression was normalized to the control group.

**2.11. Animal Experiment.** In order to test the bone regeneration capability of fibrin/ALN gel in an animal model, fibrin gel and fibrin/ALN gel were polymerized with thrombin solution at a final concentration of 20 mg/mL fibrinogen and  $10^{-6}$  M ALN as described above. The experimental procedures were approved by the Institute of Laboratory Animal Research, Wonkwang University. New Zealand white rabbits, aged 3 months and weighing approximately 2.5–3.0 kg, were used in the study. All the animals were anesthetized by intramuscular injection with a combination of 35 mg/kg ketamine (Yuhan ketamine®, Yuhan Crop., Seoul, Korea) and xylazine (Celactal®, Bayer Animal Health Crop., Seoul, Korea) and local anesthesia on the surgical site using 2% lidocaine solution. We approached the calvaria via linear incision through the skin and subcutaneous tissue over the medial line and induced two

separate circular defects using a trephine bur with an outer diameter of 8 mm. The animal study was performed using four rabbits at each time-point in all experiments with two defects induced in each rabbit. One of the calvarial defects was filled with fibrin gel without ALN and the other was filled with fibrin/ALN gel.

At 2, 4, and 8 weeks after surgery, bone tissue defects were removed from the host bone and fixed with 4% paraformaldehyde buffer (pH 7.2) before performing further experiments.

**2.12. Microcomputed Tomography (CT) Evaluation.** In order to evaluate the volume of regenerated bone, both defects were analyzed using three-dimensional micro-CT (Sky-Scan 1172™; Skyscan, Kontich, Belgium). The medium resolution was 8.82  $\mu\text{m}$  and the X-ray generator was on an operating voltage of 60 kV with a constant current of 167  $\mu\text{A}$ . The beam was filtered through a 0.5 mm aluminum filter. The image data were reconstructed and three-dimensional images were obtained. Based on the micro-CT data sets, the newly formed bone volume was calculated within the region of interest.

**2.13. Histological Analysis.** After micro-CT scanning, all specimens were decalcified in 10% EDTA and then dehydrated in a graded alcohol series ranging from 70 to 100%. Paraffin blocks were prepared using a routine process and were cut into 5  $\mu\text{m}$  sections (HM 325; Microm, Walldorf, Germany). For each sample, we stained five sections with hematoxylin & eosin (H&E) and Goldner's Masson trichrome, using standard techniques.

**2.14. Statistical Analysis.** All experiments were performed in triplicate. Values are expressed as mean  $\pm$  standard deviation (SD) and one-way analysis of variance (ANOVA) followed by a post *t*-test was performed using GraphPad Prism version 5.3 (GraphPad Software, San Diego, CA, USA).  $P < 0.05$  was considered statistically significant.

### 3. Results

**3.1. Morphological/Mechanical/Release Characterization of Fibrin/ALN Gels.** Fibrin/ALN gels were formulated with various concentrations of ALN. The formed gels were solid-like, semitransparent in appearance, and not affected by ALN concentration (Figure 2(a)). Next, we measured the compressive moduli of the fibrin/ALN gels. Young's modulus of the gels prepared with fibrin alone was  $13.37 \pm 0.6$  kPa and did not change significantly with the addition of ALN ( $P > 0.05$ ) (Figure 2(b)).

The ALN release kinetics results showed that the amount of ALN released increased with ALN concentration. Overall, the results showed a sustained ALN release of approximately 45% up until 10 days (Figure 2(c)).

**3.2. Cell Proliferation and Cellular Response.** To evaluate the effect of ALN concentration on hMSCs, cells were embedded in the gel and cultured. As shown in Figure 2, cell proliferation significantly increased in  $10^{-6}$  M ALN gels compared with the control. The cell proliferation markedly decreased in  $10^{-4}$  M ALN gels (Figure 3). To assess the in vitro cytocompatibility

of the fibrin/ALN gels with varying amounts of ALN, hMSCs cultured for 3 days within the gels were evaluated. The embedded cells were stained using live/dead fluorescence staining reagents and examined using a fluorescence microscope. Figure 4 shows that most of the hMSCs were viable and retained a fibroblast-like morphology in fibrin gels and  $10^{-7}$ ,  $10^{-6}$ , and  $10^{-5}$  M ALN composite fibrin gels. In contrast, when cells were embedded in  $10^{-4}$  M ALN fibrin/ALN gels, a large number of cells were found to be dead or unhealthy.

**3.3. Osteoblast Differentiation.** To determine the effect of ALN concentration of fibrin gels on osteoblast differentiation of hMSCs, ALP activity was analyzed at 7 days. Cells cultured in  $10^{-7}$  M,  $10^{-6}$  M, and  $10^{-5}$  M ALN fibrin gels exhibited significantly increased ALP activity compared with the control. ALP activity was not detected in  $10^{-4}$  M ALN fibrin gels (Figure 5(a)). In addition, calcium accumulation was analyzed to determine osteoblast differentiation. When cultured in  $10^{-7}$ ,  $10^{-6}$ , and  $10^{-5}$  M ALN fibrin gels, the results showed significantly increased calcium accumulation with the highest accumulation detected in the  $10^{-6}$  M ALN fibrin gel (Figure 5(b)). Real-time PCR for several osteoblast marker genes was also used to assess osteoblast differentiation. The mRNA expression of *Coll1A1*, *Runx2*, and *OCN* was significantly higher in ALN fibrin gels than in fibrin only gel (Figure 5(c)).

**3.4. Micro-CT Evaluation.** To examine the capacity of the fibrin/ALN gels to promote bone regeneration, fibrin and fibrin/ALN gels formulated with  $10^{-6}$  M ALN were implanted in a rabbit calvarial bone defect. At 2, 4, and 8 weeks after implantation, the tissue was harvested and new bone formation was analyzed using micro-CT. Figure 6(a) shows the three-dimensional images of the implanted fibrin or fibrin/ALN gels. In all groups, new bone formation occurred from the marginal defect site and progressed over time. Furthermore, 4 or 8 weeks after implantation, newly formed bone was greater in the fibrin/ALN gel-implanted group than in the fibrin gel implant group. Quantification of bone regeneration revealed significant differences in each group. Specifically, the newly formed bone volume was greater in the fibrin/ALN gel-implanted group ( $38.02 \pm 1.00$  mm<sup>3</sup>) than in the fibrin gel group ( $31.24 \pm 0.76$  mm<sup>3</sup>) at 8 weeks after implantation (Figure 6(b)).

**3.5. Histology.** Histological evaluation of the fibrin/ALN gel-repaired defect specimens was performed at 2, 4, and 8 weeks after implantation. Figure 7 shows the H&E-stained marginal site of the bone defect. Two weeks after implantation, a small amount of newly formed bone was observed at the margin of the defect in specimens implanted with fibrin gel. Otherwise, more thickness newly formed bone was observed in fibrin/ALN gel-implanted specimens. Four weeks after implantation, matured new bone was observed and newly formed bone was integrated with the host bone at the marginal aspect of the defect. At 8 weeks after implantation, the matured new bone was found to be more developed, and bone marrow cavity-like morphology was observed. Bone

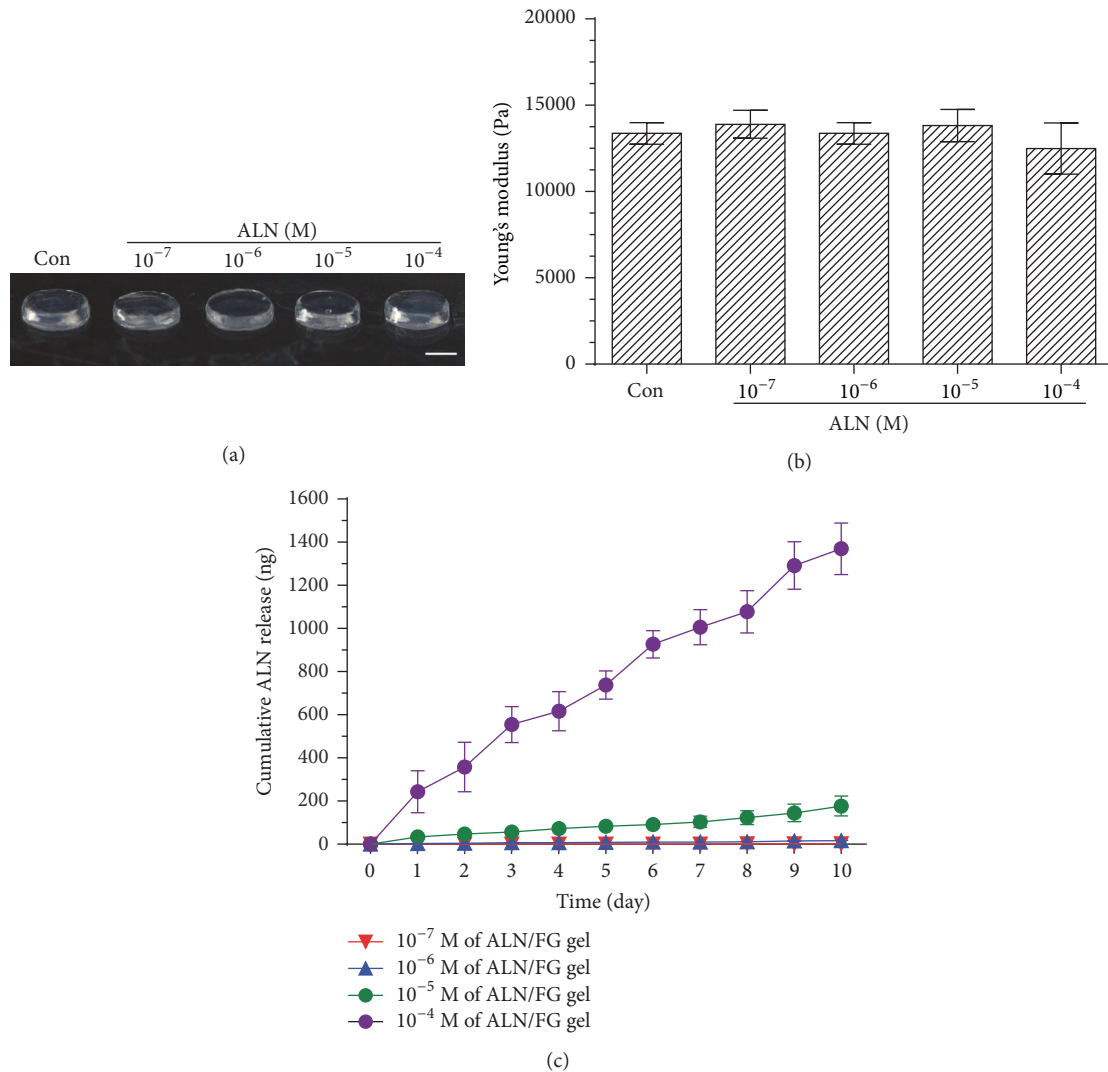


FIGURE 2: (a) Gross view of fibrin gels containing various ALN concentrations (10<sup>-4</sup> M~10<sup>-7</sup> M). (b) Effects of ALN concentration on the stiffness of fibrin/ALN gel. The stiffness of the fibrin/ALN gel was not significantly affected by ALN concentration. (c) In vitro cumulative release of ALN from fibrin gel. A slow sustained release was observed. The data shown are the mean ± standard deviation (SD) of three independent experiments.

growth was markedly thicker in the fibrin/ALN gel group than in the fibrin gel group (Figure 8). In addition, Figure 9 shows Goldner’s Masson trichrome staining of the central area of the calvarial defects. At 2 weeks after implantation, large amounts of fibroblastic connective tissue were observed in all groups. A small amount of immature bone was observed in the fibrin/ALN gel-implanted group. Furthermore, mature bone islands were observed at 4 weeks and this newly formed bone was more abundant at 8 weeks after implantation in the fibrin/ALN-implanted group. The results of the histological observation confirmed the results obtained from micro-CT analysis.

**4. Discussion**

Patients with severe bone loss could greatly benefit from tissue regeneration in large defects. Therefore, a number of

studies have attempted to enhance bone regeneration using growth factors or osteoinductive drugs. Several studies have reported enhanced bone regeneration using locally applied ALN. However, the use of ALN in combination with fibrin gel for bone tissue engineering has not yet been evaluated.

In this study, we prepared ALN-containing fibrin gels and the properties of fibrin/ALN gels, including compressive moduli, ALN release kinetics, in vitro cellular behavior of hMSCs, and in vivo bone regeneration capacity were evaluated. The concentrations of fibrinogen and thrombin affect the stiffness of fibrin gels [21]. In addition, the stiffness is affected by composite materials such as protein [22], and the mechanical strength of a gel influences cellular proliferation and spreading [23]. In this study, fibrinogen (20 mg/mL) and thrombin (2 IU/mL) were used because these concentrations were optimized in pilot experiments [24], and our results showed that the stiffness was not significantly affected by

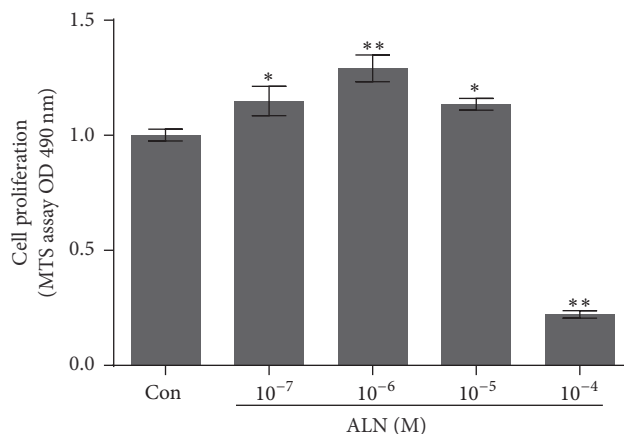


FIGURE 3: Effect of ALN concentration in fibrin/ALN gels on human mesenchymal stem cell (hMSC) proliferation. Cells were embedded and cultured in the fibrin gels prepared with ALN at various concentrations. After 3 days of cultivation, cell proliferation was measured. The cells embedded in the fibrin/ALN gels prepared with  $10^{-7}$ ,  $10^{-6}$ , and  $10^{-5}$  M ALN exhibited increased proliferation. However, proliferation was significantly inhibited in fibrin/ALN gels prepared with  $10^{-4}$  M ALN. The data shown are the mean  $\pm$  standard deviation (SD) of three independent experiments. \* $P < 0.05$  and \*\* $P < 0.01$  compared with the control.

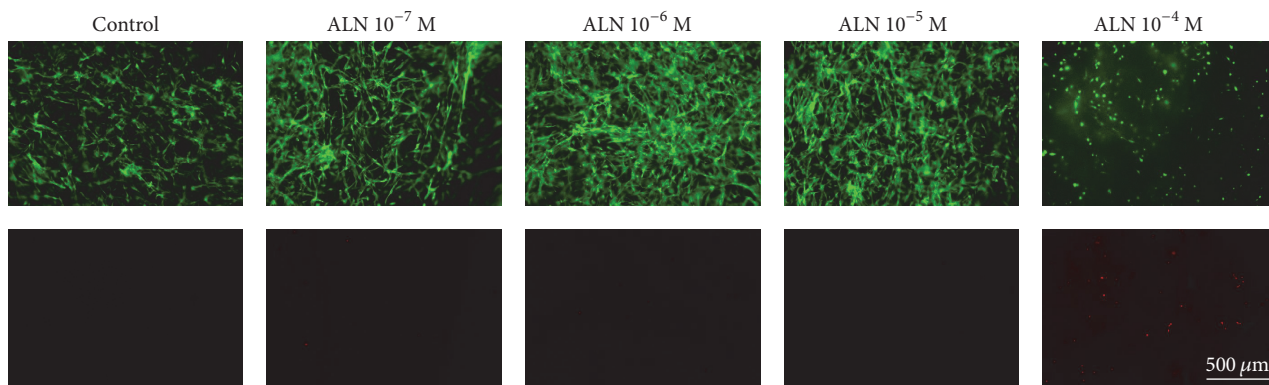


FIGURE 4: Effect of ALN concentration in fibrin/ALN gels on cell viability. Human mesenchymal stem cells (hMSCs) were embedded in fibrin/ALN gels containing various concentrations of ALN. After 3 days of cultivation, live/dead staining was performed. Most of the hMSCs were viable and retained a fibroblast-like morphology (stained by calcein AM, shown in green) in fibrin gels and  $10^{-7}$ ,  $10^{-6}$ , and  $10^{-5}$  M ALN composite fibrin gels. In contrast, when cells were embedded in  $10^{-4}$  M ALN fibrin/ALN gel, a large number of cells were found to be dead or unhealthy (stained by EthD-1, shown in red) and cells were poorly distributed and had a rounded cellular morphology.

ALN addition. A previous study reported that the stiffness of fibrin gel was influenced by the embedded cell density [25]. According to Jansen et al.'s report, stiffness was also affected by fibrin concentration, and significant changes only occurred at fibrin concentrations  $< 2$  mg/mL. In keeping with these reports, in the present study, gel stiffness was not significantly changed by cell embedding (data not shown), which is likely due to the fibrinogen concentration used in this study. The fibrin gels prepared in this study were shown to contain mostly viable cells that displayed an elongated fibroblastic-like morphology.

Several researchers have investigated the local application of ALN for bone repair. However, when using local injection, drug release pattern is an important factor. According to Jeon et al., the growth factor release pattern is influenced by the fibrinogen and thrombin concentrations. They showed that when using 94.3 mg/mL fibrinogen and 33.3 IU/mL thrombin, approximately 60% of the growth factor was released

after 3 days. In contrast, we observed a slow release profile and approximately 45% of the ALN was released after 10 days. The different release profiles may be the result of different concentrations of fibrinogen and thrombin [26], differences in the chemical structure and properties of the loaded drug, and preparation method [27].

In vitro cellular evaluation was the starting point for determining the biocompatibility of the formulated gel system. In this study, we first assessed cell proliferation and cytotoxicity to evaluate biocompatibility. A number of studies have reported that ALN regulates cell proliferation and differentiation [3, 28]. A previous study reported that ALN enhanced proliferation of human bone marrow stromal cells and also initiated osteoblastic differentiation involving osteogenesis-related genes such as BMP-2, bone sialoprotein-II, and Col1A1 [3]. Im et al. reported that the proliferation of MG-63 cells increased over a wide concentration range from  $10^{-6}$  M to  $10^{-9}$  M of ALN, while at  $10^{-4}$  M, cell proliferation

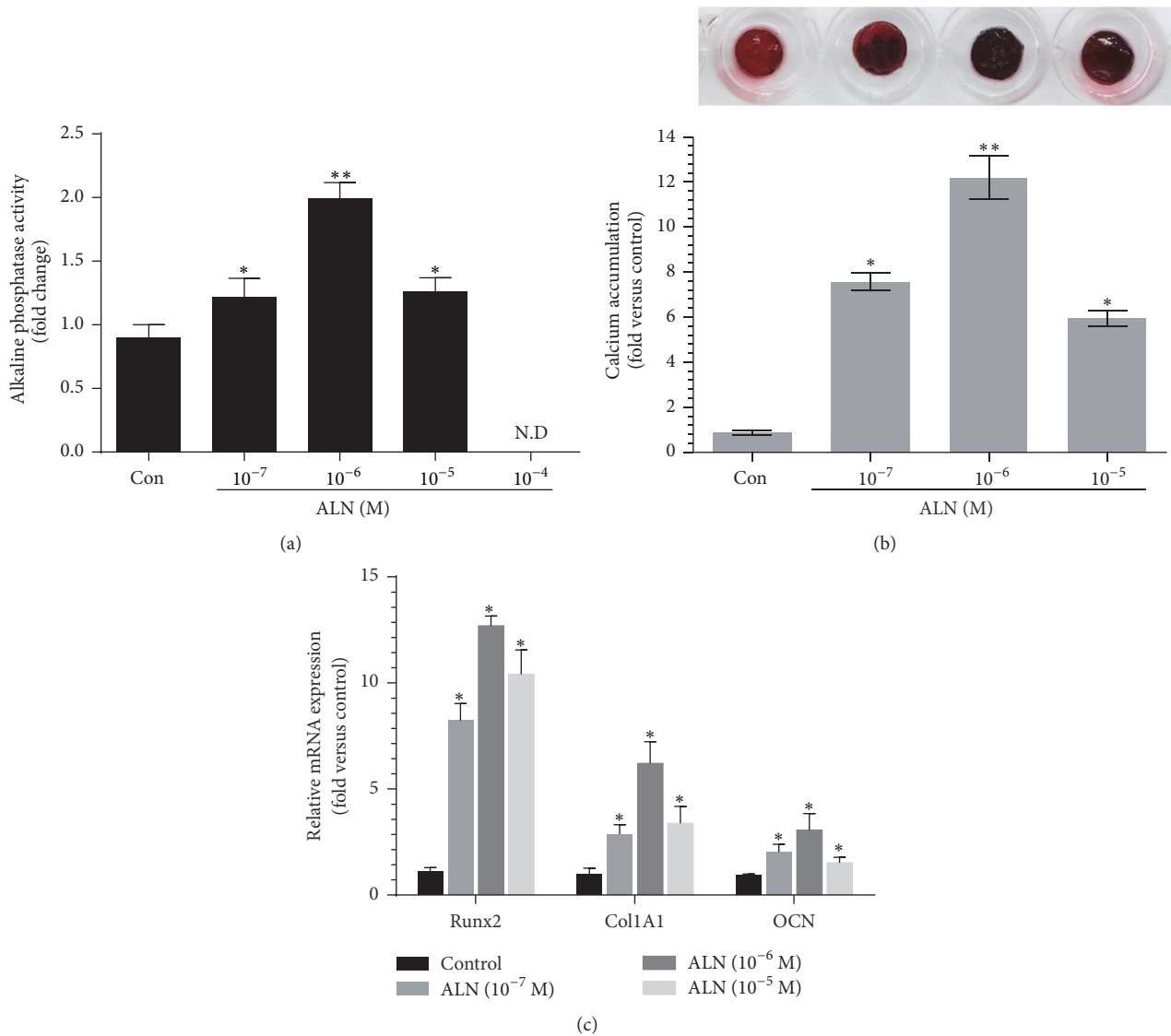


FIGURE 5: Effect of ALN concentration in fibrin/ALN gels (a) on alkaline phosphatase (ALP) activity (ND, not detected) and (b) calcium accumulation. Human mesenchymal stem cells (hMSCs) were embedded in the fibrin/ALN gels containing various concentrations of ALN. ALP activity assay and alizarin red S staining were performed after 7 and 14 days of cultivation, respectively. (c) In addition, after 7 days of cultivation, real-time PCR was performed for several osteoblast marker genes and cells cultured in fibrin/ALN gels containing 10<sup>-7</sup>, 10<sup>-6</sup>, and 10<sup>-5</sup> M ALN, and osteoblast differentiation was significantly increased. The data shown are the means ± standard deviation (SD) of three independent experiments. \* *P* < 0.05 and \*\* *P* < 0.01 compared with control.

decreased [5]. We observed increased cell proliferation from 10<sup>-5</sup> to 10<sup>-7</sup> M and the highest concentration of 10<sup>-4</sup> M ALN inhibited cell proliferation. This is in agreement with the results reported by Im et al. [5]. This effect may be attributable to cytotoxicity of ALN at high concentrations and this is also supported by our live/dead assay results. Furthermore, they also showed that ALP activity level increased after treatment with 10<sup>-8</sup> M ALN [5]. We used ALP activity and calcium accumulation as an indicator of osteoblast differentiation. Our data showed that the ALP activity and calcium accumulation in fibrin gels increased with increasing ALN concentration from 10<sup>-5</sup> M to 10<sup>-7</sup> M and the highest osteoblast differentiation was observed in 10<sup>-6</sup> M ALN-containing fibrin gels.

In 10<sup>-4</sup> M ALN fibrin gels, ALP activity was not detected because the high concentration inhibited cell proliferation, as previously described. During osteoblast differentiation, *Col1A1* [29, 30] and *Runx2* are important genes [31] that, together with *OCN*, regulate osteoblast differentiation [32]; these genes are well known osteoblast markers. Therefore, to confirm ALN-induced osteoblast differentiation, we performed real-time PCR for these marker genes and showed that their induction was related to ALN concentration in the fibrin gel system. The results suggest that fibrin gels containing 10<sup>-7</sup> M~10<sup>-5</sup> M of ALN resulted in enhanced cell proliferation and osteoblastic differentiation of embedded hMSCs.

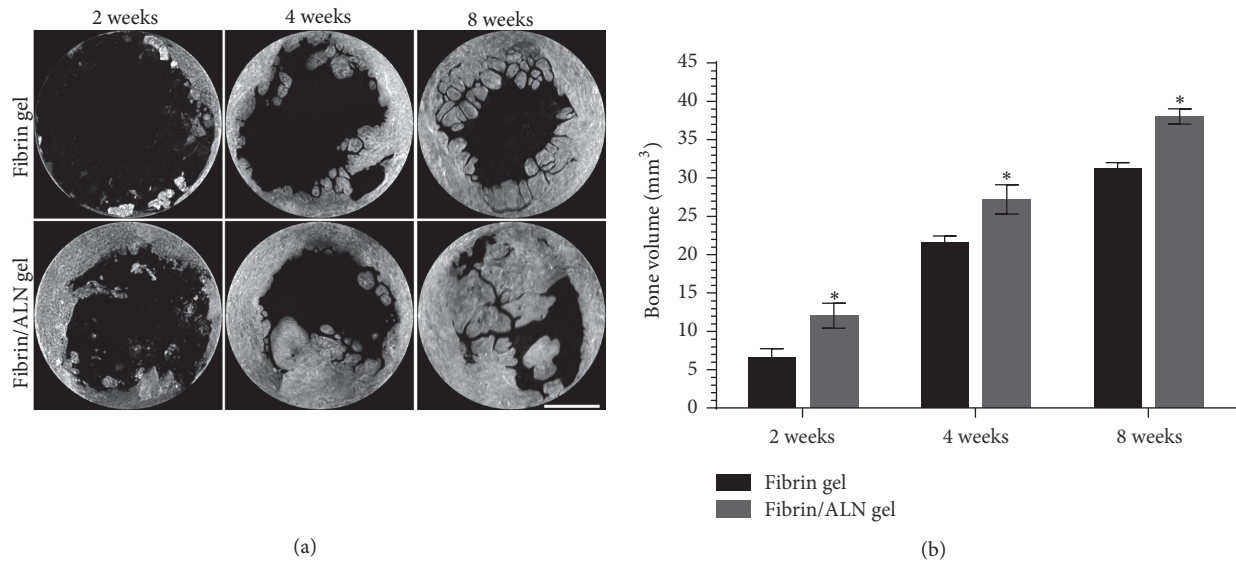


FIGURE 6: Effect of fibrin/ALN gel on new bone formation in a rabbit calvarial defect. Representative three-dimensional microcomputer tomography images (a) and quantification graph (b) of calvarial bone defect regeneration at 2, 4, and 8 weeks after implantation with fibrin gel or fibrin/ALN gel. The new bone formation increased in the fibrin/ALN gel ( $10^{-6}$  M ALN) group compared to that in the fibrin gel-implanted group. Scale bar = 3 mm. The data shown are the mean  $\pm$  standard deviation (SD). \*  $P < 0.05$  compared with the fibrin gel-implanted group.

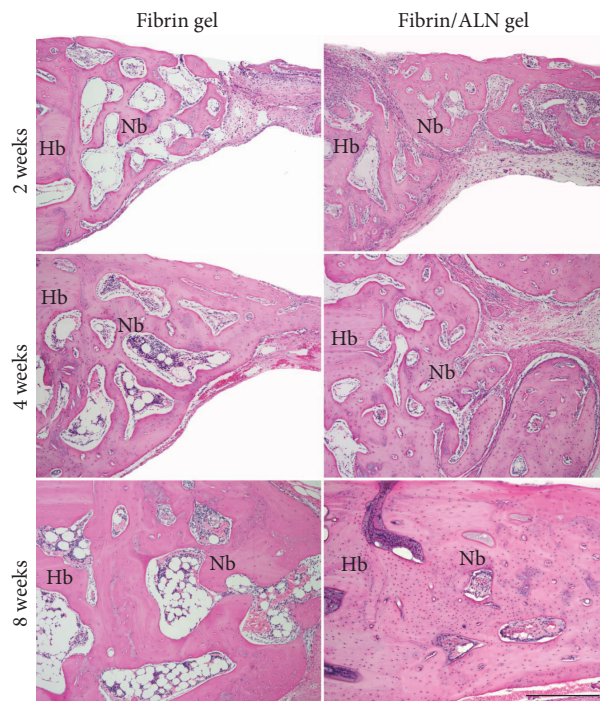


FIGURE 7: Hematoxylin and eosin-stained microscopic images of the margin of the defect site at 2, 4, and 8 weeks after implantation of fibrin gel or fibrin/ALN gel (containing  $10^{-6}$  M ALN). Newly formed bone at the periphery of the defect was observed in both the fibrin gel and fibrin/ALN groups from 2 weeks after implantation. Mature bone was more abundant in the fibrin/ALN group and newly formed bone tended to coalesce with the host bone. Hb, host bone; Nb, new bone. Scale bar: 250  $\mu$ m.

We used a rabbit calvarial defect model to evaluate the capacity of fibrin/ALN gels to regenerate bone after injury. Several studies report enhanced bone formation following local delivery of ALN [33, 34]. Toker et al. reported that an autogenous bone graft with ALN enhanced new bone

formation in a rat calvarial defect model [33]. Komatsu et al. found that local application of ALN promoted bone formation in a rat tooth replantation model, and the bone formation effects may have occurred through endocytic incorporation of ALN and subsequent inhibition of protein

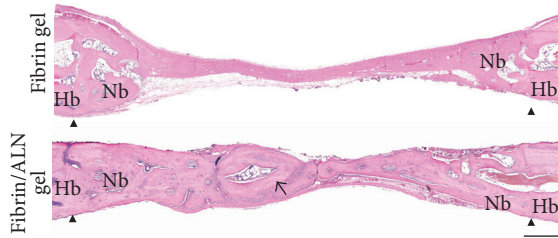


FIGURE 8: Histologic morphology of the new bone at 8 weeks after implantation. In the central area, newly formed bone was more mature in the fibrin/ALN gel-implanted group than in the fibrin gel group. The arrow indicates the newly formed bone containing woven bone and lamella. Arrow head indicates the defect marginal site. Hb, host bone; Nb, new bone. Scale bar: 500  $\mu\text{m}$ .

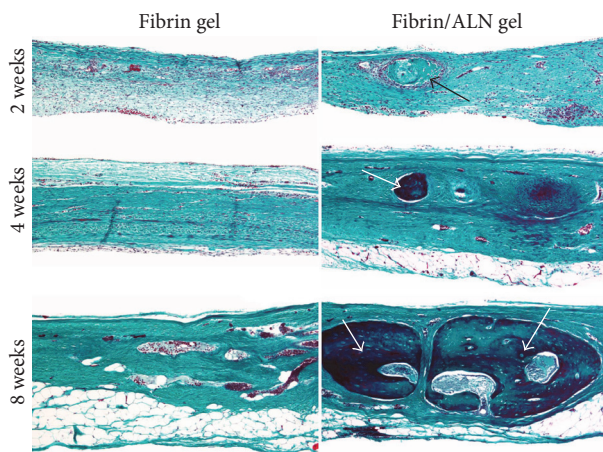


FIGURE 9: Goldner's Masson trichrome-stained histological images of regenerated bone in the central area of calvarial defects at 2, 4, and 8 weeks after implantation. At 2 weeks, large amounts of fibroblastic connective tissue were observed in the fibrin gel and fibrin/ALN gel-implanted groups. Specifically, a small island-like amount of immature bone (black arrow) was observed in the fibrin/ALN gel-implanted group. Furthermore, mature bone islands (white arrow) were observed at 4 weeks and the newly formed bones were more abundant at 8 weeks in the fibrin/ALN-implanted group than in the fibrin gel-implanted group. Scale bar: 250  $\mu\text{m}$ .

prenylation [34]. For our *in vivo* study, we used fibrin gel prepared with  $10^{-6}$  M ALN because of its superior cellular cytocompatibility. After implantation of the fibrin/ALN gel into the calvarial defect, newly formed bone, in the form of an island, was visible in the central defect area. Furthermore, the newly formed bone increased in the fibrin/ALN gel-implanted group compared to that in the fibrin gel group. Although the precise biological mechanism of fibrin/ALN gel involved in bone formation was not revealed in this study, our findings suggest that improved bone formation occurred via stimulation of proliferation and differentiation of bone-forming cells by ALN released from the fibrin/ALN gel.

## 5. Conclusions

We prepared fibrin/ALN gels for ALN local delivery to improve bone regeneration. The fibrin/ALN gel provided

a suitable environment for hMSC proliferation and differentiation *in vitro*. Furthermore, fibrin/ALN gels enhanced new bone formation in a rabbit calvarial defect *in vivo*. This study highlighted the potential of fibrin/ALN gel for drug delivery and sustained release for bone tissue regeneration applications. Further studies should focus on enhancing bone defect regeneration by varying the fibrinogen and thrombin concentrations in fibrin/ALN gels.

## Competing Interests

The authors declare that there is no conflict of interests regarding the publication of this paper.

## Acknowledgments

This work was supported by the National Research Foundation of Korea (NRF) funded by the Ministry of Science, ICT, and Future Planning (NRF-2015R1A2A2A01004888) and the Ministry of Education (NRF-2015R1D1A1A01056748).

## References

- [1] B.-S. Kim, M.-K. Choi, J.-H. Yoon, and J. Lee, "Evaluation of bone regeneration with biphasic calcium phosphate substitute implanted with bone morphogenetic protein 2 and mesenchymal stem cells in a rabbit calvarial defect model," *Oral Surgery, Oral Medicine, Oral Pathology and Oral Radiology*, vol. 120, no. 1, pp. 2–9, 2015.
- [2] C.-H. Chung, Y.-K. Kim, J.-S. Lee, U.-W. Jung, E.-K. Pang, and S.-H. Choi, "Rapid bone regeneration by *Escherichia coli*-derived recombinant human bone morphogenetic protein-2 loaded on a hydroxyapatite carrier in the rabbit calvarial defect model," *Biomaterials Research*, vol. 19, article 17, 2015.
- [3] F. Von Knoch, C. Jaquiere, M. Kowalsky et al., "Effects of bisphosphonates on proliferation and osteoblast differentiation of human bone marrow stromal cells," *Biomaterials*, vol. 26, no. 34, pp. 6941–6949, 2005.
- [4] G. Duque and D. Rivas, "Alendronate has an anabolic effect on bone through the differentiation of mesenchymal stem cells," *Journal of Bone and Mineral Research*, vol. 22, no. 10, pp. 1603–1611, 2007.
- [5] G.-I. Im, S. A. Qureshi, J. Kenney, H. E. Rubash, and A. S. Shanbhag, "Osteoblast proliferation and maturation by bisphosphonates," *Biomaterials*, vol. 25, no. 18, pp. 4105–4115, 2004.
- [6] J. S. Chen and P. N. Sambrook, "Antiresorptive therapies for osteoporosis: a clinical overview," *Nature Reviews Endocrinology*, vol. 8, no. 2, pp. 81–91, 2012.
- [7] R. G. G. Russell, N. B. Watts, F. H. Ebetino, and M. J. Rogers, "Mechanisms of action of bisphosphonates: similarities and differences and their potential influence on clinical efficacy," *Osteoporosis International*, vol. 19, no. 6, pp. 733–759, 2008.
- [8] R. G. G. Russell and M. J. Rogers, "Bisphosphonates: from the laboratory to the clinic and back again," *Bone*, vol. 25, no. 1, pp. 97–106, 1999.
- [9] P. J. J. Prinsloo and D. J. Hosking, "Alendronate sodium in the management of osteoporosis," *Therapeutics and Clinical Risk Management*, vol. 2, no. 3, pp. 235–249, 2006.
- [10] H. V. Cohen, "Bisphosphonate-associated osteonecrosis of the jaw: patient care considerations: overview for the orthopaedic

- nursing healthcare professional," *Orthopaedic Nursing*, vol. 29, no. 3, pp. 176–182, 2010.
- [11] H. Toker, H. Ozdemir, H. Ozer, and K. Eren, "A comparative evaluation of the systemic and local alendronate treatment in synthetic bone graft: a histologic and histomorphometric study in a rat calvarial defect model," *Oral Surgery, Oral Medicine, Oral Pathology and Oral Radiology*, vol. 114, no. 5, pp. S146–S152, 2012.
- [12] J. T. Horan and C. W. Francis, "Fibrin degradation products, fibrin monomer and soluble fibrin in disseminated intravascular coagulation," *Seminars in Thrombosis and Hemostasis*, vol. 27, no. 6, pp. 657–666, 2001.
- [13] B. Kim, J. Kim, S. Yang, H. Kim, H. J. Lim, and J. Lee, "Angiogenin-loaded fibrin/bone powder composite scaffold for vascularized bone regeneration," *Biomaterials Research*, vol. 19, article no. 18, 2015.
- [14] B. K. Gu, D. J. Choi, S. J. Park, M. S. Kim, C. M. Kang, and C. Kim, "3-dimensional bioprinting for tissue engineering applications," *Biomaterials Research*, vol. 20, no. 12, 2016.
- [15] P. A. Janmey, J. P. Winer, and J. W. Weisel, "Fibrin gels and their clinical and bioengineering applications," *Journal of the Royal Society Interface*, vol. 6, no. 30, pp. 1–10, 2009.
- [16] H. Arbes, P. Bösch, F. Lintner, and M. Salzer, "First clinical experience with heterologous cancellous bone grafting combined with the Fibrin Adhesive System (F.A.S.)," *Archives of Orthopaedic and Traumatic Surgery*, vol. 98, no. 3, pp. 183–188, 1981.
- [17] N. Isogai, W. J. Landis, R. Mori et al., "Experimental use of fibrin glue to induce site-directed osteogenesis from cultured periosteal cells," *Plastic and Reconstructive Surgery*, vol. 105, no. 3, pp. 953–963, 2000.
- [18] J. A. Hubbell, "Biomaterials in tissue engineering," *Nature Biotechnology*, vol. 13, no. 6, pp. 565–576, 1995.
- [19] J. Kuljanin, I. Janković, J. Nedeljković, D. Prstojević, and V. Marinković, "Spectrophotometric determination of alendronate in pharmaceutical formulations via complex formation with Fe(III) ions," *Journal of Pharmaceutical and Biomedical Analysis*, vol. 28, no. 6, pp. 1215–1220, 2002.
- [20] B.-S. Kim, J. S. Kim, H.-M. Sung, H.-K. You, and J. Lee, "Cellular attachment and osteoblast differentiation of mesenchymal stem cells on natural cuttlefish bone," *Journal of Biomedical Materials Research Part A*, vol. 100, no. 7, pp. 1673–1679, 2012.
- [21] W. Ho, B. Tawil, J. C. Y. Dunn, and B. M. Wu, "The behavior of human mesenchymal stem cells in 3D fibrin clots: dependence on fibrinogen concentration and clot structure," *Tissue Engineering*, vol. 12, no. 6, pp. 1587–1595, 2006.
- [22] V. K. Lai, S. P. Lake, C. R. Frey, R. T. Tranquillo, and V. H. Barocas, "Mechanical behavior of collagen-fibrin co-gels reflects transition from series to parallel interactions with increasing collagen content," *Journal of Biomechanical Engineering*, vol. 134, no. 1, Article ID 011004, 2012.
- [23] F. Brandl, F. Sommer, and A. Goepferich, "Rational design of hydrogels for tissue engineering: impact of physical factors on cell behavior," *Biomaterials*, vol. 28, no. 2, pp. 134–146, 2007.
- [24] B.-S. Kim, H.-J. Kim, J.-G. Choi, H.-K. You, and J. Lee, "The effects of fibrinogen concentration on fibrin/atelocollagen composite gel: an *in vitro* and *in vivo* study in rabbit calvarial bone defect," *Clinical Oral Implants Research*, vol. 26, no. 11, pp. 1302–1308, 2015.
- [25] K. A. Jansen, R. G. Bacabac, I. K. Piechocka, and G. H. Koenderink, "Cells actively stiffen fibrin networks by generating contractile stress," *Biophysical Journal*, vol. 105, no. 10, pp. 2240–2251, 2013.
- [26] O. Jeon, H. R. Soo, H. C. Ji, and B.-S. Kim, "Control of basic fibroblast growth factor release from fibrin gel with heparin and concentrations of fibrinogen and thrombin," *Journal of Controlled Release*, vol. 105, no. 3, pp. 249–259, 2005.
- [27] A. Breen, T. O'Brien, and A. Pandit, "Fibrin as a delivery system for therapeutic drugs and biomolecules," *Tissue Engineering—Part B: Reviews*, vol. 15, no. 2, pp. 201–214, 2009.
- [28] G. G. Reinholz, B. Getz, L. Pederson et al., "Bisphosphonates directly regulate cell proliferation, differentiation, and gene expression in human osteoblasts," *Cancer Research*, vol. 60, no. 21, pp. 6001–6007, 2000.
- [29] R. J. Majeska and R. E. Wuthier, "Studies on matrix vesicles isolated from chick epiphyseal cartilage Association of pyrophosphatase and ATPase activities with alkaline phosphatase," *Biochimica et Biophysica Acta*, vol. 391, no. 1, pp. 51–60, 1975.
- [30] L. Masi, A. Franchi, M. Santucci et al., "Adhesion, growth, and matrix production by osteoblasts on collagen substrata," *Calcified Tissue International*, vol. 51, no. 3, pp. 202–212, 1992.
- [31] C. Banerjee, L. R. McCabe, J.-Y. Choi et al., "Runt homology domain proteins in osteoblast differentiation: AML3/CBFA1 is a major component of a bone-specific complex," *Journal of Cellular Biochemistry*, vol. 66, no. 1, pp. 1–8, 1997.
- [32] J. B. Lian, G. S. Stein, J. L. Stein, and A. J. van Wijnen, "Osteocalcin gene promoter: unlocking the secrets for regulation of osteoblast growth and differentiation," *Journal of Cellular Biochemistry. Supplement*, vol. 30-31, pp. 62–72, 1998.
- [33] H. Toker, H. Ozdemir, H. Ozer, and K. Eren, "Alendronate enhances osseous healing in a rat calvarial defect model," *Archives of Oral Biology*, vol. 57, no. 11, pp. 1545–1550, 2012.
- [34] K. Komatsu, A. Shimada, T. Shibata et al., "Alendronate promotes bone formation by inhibiting protein prenylation in osteoblasts in rat tooth replantation model," *Journal of Endocrinology*, vol. 219, no. 2, pp. 145–158, 2013.

## Research Article

# Analysis of the Osteogenic Effects of Biomaterials Using Numerical Simulation

Lan Wang,<sup>1,2</sup> Jie Zhang,<sup>1</sup> Wen Zhang,<sup>1</sup> Hui-Lin Yang,<sup>3</sup> and Zong-Ping Luo<sup>1,3</sup>

<sup>1</sup>Orthopaedic Institute, Soochow University, Suzhou, China

<sup>2</sup>Department of Fundamental Courses, Wuxi Institute of Technology, Wuxi, China

<sup>3</sup>Department of Orthopaedics, The First Affiliated Hospital, Soochow University, Suzhou, China

Correspondence should be addressed to Zong-Ping Luo; [zongping\\_luo@yahoo.com](mailto:zongping_luo@yahoo.com)

Received 31 October 2016; Accepted 30 November 2016; Published 2 January 2017

Academic Editor: Zheng Ren

Copyright © 2017 Lan Wang et al. This is an open access article distributed under the Creative Commons Attribution License, which permits unrestricted use, distribution, and reproduction in any medium, provided the original work is properly cited.

We describe the development of an optimization algorithm for determining the effects of different properties of implanted biomaterials on bone growth, based on the finite element method and bone self-optimization theory. The rate of osteogenesis and the bone density distribution of the implanted biomaterials were quantitatively analyzed. Using the proposed algorithm, a femur with implanted biodegradable biomaterials was simulated, and the osteogenic effects of different materials were measured. Simulation experiments mainly considered variations in the elastic modulus (20–3000 MPa) and degradation period (10, 20, and 30 days) for the implanted biodegradable biomaterials. Based on our algorithm, the osteogenic effects of the materials were optimal when the elastic modulus was 1000 MPa and the degradation period was 20 days. The simulation results for the metaphyseal bone of the left femur were compared with micro-CT images from rats with defective femurs, which demonstrated the effectiveness of the algorithm. The proposed method was effective for optimization of the bone structure and is expected to have applications in matching appropriate bones and biomaterials. These results provide important insights into the development of implanted biomaterials for both clinical medicine and materials science.

## 1. Introduction

Biological systems have mechanisms to automatically adapt to environmental changes in order to maintain their required functions under varying conditions and stresses [1]. Many studies have investigated functional biological adaptations to environmental changes in the muscles, lungs [2, 3], arteries [4], bones [5, 6], and even plants [7]. For example, bones gradually adapt into an optimal structure to support our organs and human anatomical features. As the external loading changes, the bone structure will adopt an optimal shape and structure to adapt to the new loading; this process is called bone functional adaptation. The mechanisms mediating bone adaptation have been studied extensively. The “self-optimizing” properties of bone were described as early as 1896 [8], and a theory, known as Wolff’s law, on the naturally optimum structure of bone was proposed.

Some of the earliest theoretical frameworks for bone adaptation included proposals for the elastic formulation of

apparent bone density by an exponential penalization factor [9, 10]. Bendsøe [11] obtained similar results using topology optimization by the penalized material model. Recently, with the rapid development of computer technology, the quantitative study of bone functional adaptation has become possible [12]. Rossi and Wendling-Mansuy [13], Weinans et al. [14], and Beaupré et al. [15] combined mathematical descriptions with the finite element method (FEM) to quantitatively predict the self-optimizing features of bones, and the computed outcomes were shown to have many similarities with actual bone morphologies. Boyle and Kim [16] applied topology optimization to simulate three-dimensional human proximal femur remodeling and further proved the effectiveness of Wolff’s hypothesis.

However, bones are not necessarily always healthy and may have defects or fractures. The rapid development of biomedicine has provided access to new methods such as implantation to support defective bones, stimulate cell growth, and release ions to help generate better bone

structure. Moreover, the optimal features of bone materials, including compatibility, reactivity, and degradability, have been studied extensively for use in the clinical setting [17, 18].

For new bone, the initial mechanical strength is very important. If it is too strong, the concentration of stress on the new bone may be disadvantageous toward osteogenesis [19, 20]. If it is too weak, the bone cannot provide adequate support [21]. When choosing an optimal bone material, its initial biomechanical strength and its rate of degradation must be considered simultaneously [20]. If the degradation rate is too fast, voids in the bone may appear and lead to a weakened structure and the failure of osteogenesis [22]. If the rate is too slow, osteogenesis will be hindered [23]. Therefore, the appropriate bone material for implantation must be chosen to simultaneously satisfy both the degradation rate and new bone formation capacity, leading to the improved synchronization of both events. The implantation of bone material will cause changes in the stress applied to the bones, which will in turn cause changes in the internal structure optimization. The original optimization algorithm for bone cannot be used directly in defective bones, and the challenge thus becomes the matching of the bone material and osteogenesis. Thus, researchers in the fields of clinical research and related material sciences have begun to focus on the problem of matching the bone implantation material with the bone tissue [24].

The two existing research approaches for achieving this goal are experimental biomechanics and FEM analysis. Although constructing an experimental animal model has advantages such as intuitiveness and subjectivity [25], the need for long testing periods and susceptibility to numerous extraneous factors can be disadvantageous. This may limit the ability of researchers to observe any quantitative relationships between the implantation material and the bones. The current constitutive model plays an important role in understanding the effects of the implantation material on bone growth. Computational digital image processing technology and computer-aided analysis methods have simplified the creation of computer models [16, 21, 26]. We have preliminary achieved simulation of osteoblast with material and bone density distribution which considered the elastic modulus of material [27]. However, the degradation period has not been considered which was very important parameter for the implanted biodegradable biomaterials and has no animal experiments to provide the corresponding support.

In this study, we created a theoretical FEM model of bone remodeling with implanted biomaterials. Our bone growth optimization process takes into consideration Young's modulus and the degradation rate of the bone material, achieving a simulation of osteoblasts with material and bone density distributions. The simulation results for the metaphyseal bone of the rat left femur and micro-CT images from rats with experimental femur defects are compared. The results validate the effectiveness of the method in modeling bone structure and overall shape optimization. In addition, this method provides theoretical guidance to the matching problem between bones and implant biomaterials.

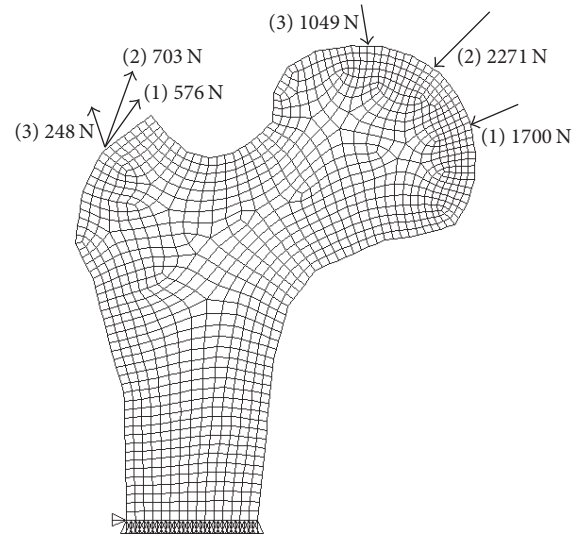


FIGURE 1: Finite element mesh for the proximal femur model.

TABLE 1: Load results for the proximal femur model.

	Joint reaction force/N	Angle/°	Rotor rally/N	Angle/°
1	1700	25	576	35
2	2271	66	703	62
3	1049	15	248	8

Note: the angle is the angle between the direction of force and the horizontal direction.

## 2. Materials and Methods

In this study, a combination of the bone self-adaptive optimization theory and material degradation rules was used to simulate the proximal femur with defects, as detailed below.

**2.1. Finite Element Model.** A two-dimensional finite element model of the proximal femur was used. The model was obtained from the preprocessing of the femur of a normal adult male using CT, Photoshop 5.0, and ANSYS 10.0 software. With the ANSYS meshing tools, the model was divided into 3,689 nodes and 1,168 elements whose mesh element size was defined as  $0.25 \text{ cm}^2$  as shown in Figure 1. The implant material was linear, elastic, and isotropic. The material properties of the model included the elastic modulus  $E$  (2000 MPa), Poisson's ratio  $\mu$  (0.3), and apparent density  $\rho$  ( $1.0 \times 10^3 \text{ kg}\cdot\text{m}^{-3}$ ) [13, 16]. The joint forces acting on the femoral head (different stress points) and the rotor muscle tendon tension were chosen based on the literature [28]. The loads are provided in Table 1. The defect was assumed to be  $1 \text{ cm} \times 1 \text{ cm}$  and involved 36 elements, including the cortical and cancellous bone. This size has been used in many prior animal experiments [25, 29, 30].

The ranges of implant material properties used in this study were previously defined [31, 32]. The elasticity modulus values were 30, 500, 1000, 2000, and 3000 MPa. For the material degradation time, the iteration step length was 1 day

for the simulation. Three time periods (10, 20, and 30 days) were chosen.

**2.2. Simulation-Based Analysis.** The optimization of the objective function is presented as follows [27]:

$$F(\rho(t)) = \sum_{j=1}^n \left( \frac{1}{2} \sigma_j(t)^T S_j(t) \sigma_j(t) \right), \quad (1)$$

where  $F$  is the strain energy at time  $t$ ,  $\sigma_j(t)$  is the stress vector component of element  $j$  at time  $t$ ,  $\rho(t) = \{\rho_j(t) \mid j = 1 \cdots n\}$ ,  $\rho_j(t)$  is the apparent density of element  $j$  at time  $t$ ,  $n$  is the number of elements, and  $S_j(t)$  is the global stiffness matrix, defined as follows:

$$S_j(t) = \begin{bmatrix} \frac{1}{E_j(t)} & -\frac{\mu_j(t)}{E_j(t)} & 0 \\ -\frac{\mu_j(t)}{E_j(t)} & \frac{1}{E_j(t)} & 0 \\ 0 & 0 & \frac{2(1 + \mu_j(t))}{E_j(t)} \end{bmatrix}, \quad (2)$$

where  $E_j(t)$  and  $\mu_j(t)$  represent the elastic modulus and Poisson's ratio, respectively.

The constraint equations are

$$g_1(\rho(t)) = \sum_{j=1}^n \rho_j(t) v_j(t), \quad (3)$$

$$0 < \rho_j(t) < 1.8 \text{ g} \cdot \text{cm}^{-3}, \quad (4)$$

where  $g_1$  was total mass constraint function and  $v_j(t)$  is volume of element  $j$  at time  $t$ . Equation (3) indicates that the bone quality remains unchanged and (4) defines  $1.8 \text{ g} \cdot \text{cm}^{-3}$  as the maximum density of the cortical bone during the optimization process. Through solving the optimization model, the density value of the next time was predicted to be  $\hat{\rho}(t+1) = \{\hat{\rho}_j(t+1) \mid j = 1 \cdots n\}$ .

Degradation of the material occurs slowly at earlier time points and more rapidly as time passes [30, 31]. In this study, an ideal material degradation function was established as follows:  $E_1(t+1) = (1 - t/T)^{0.5} * E1_0$ , where  $E1_0$  is the initial modulus of the implant material (30, 500, 1000, 2000, and 3000 MPa) [31, 32],  $E_1(t+1)$  is the elastic modulus of the implant material at time  $t+1$ , and  $T$  is degradation cycle. The relationship between the elastic modulus and apparent density is as follows:  $E = 2315\rho^3$  [21, 24].

The apparent densities of the defect elements and other part elements, respectively, follow the rules below:

$$\Delta\rho_i(t+1) = c \cdot (\hat{\rho}_i(t+1) - \rho_i(t)),$$

$$i = \left\{ \frac{n}{k} \mid k \text{ is the implant material element} \right\},$$

$$\Delta\rho_k(t+1) = c \cdot (\hat{\rho}_k(t+1) - \rho_k(t)) - (r(t+1) - r(t)) \quad (5)$$

$$\{k \text{ is the implant material element and } k = 1, \dots, 36\},$$

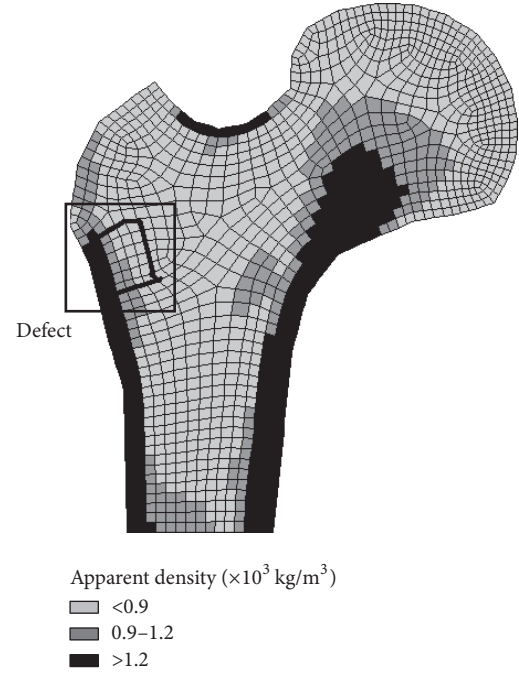


FIGURE 2: Density distribution for the proximal femur and defective area.

where  $c$  is the recycling control rate obtained from experience, defined as 0.02.  $r(t)$  was the degradation function of implant material and a second-order function was used in this work.

The next apparent density was calculated as follows:

$$\rho_j(t+1) = \rho_j(t) + \Delta\rho_j(t+1). \quad (6)$$

The osteogenesis was the mean of the 36 implanted element which was obtained as  $E_j = 2315\rho_j^3 - E1(j+1)$ .

**2.3. Animal Experiments and Finite Element Model.** Seven 10-week-old female Sprague-Dawley rats with body weights of  $204 \pm 4 \text{ g}$  were used for the micro-CT imaging study. The experimental protocol was approved by the Institutional Animal Committee. A defect (3 mm in diameter and 3 mm in depth) was drilled on the lateral side of the left femur. The biomaterial CSC (calcium sulfate cement), which has a degradation rate of 4–8 weeks in vivo for the rat model [33–36], was studied. The extents of biomaterial degradation and osteogenesis were scanned in vivo at three time points (7, 17, and 27 days) with a micro-CT scanner (SkyScan 1176, Bruker-microCT, Kontich, Belgium). The CSC, instrument parameters, and scanning methods were the same as the control animal experiment described in Zhang et al. [25], which restricted the rats in  $47 \times 35 \times 20 \text{ cm}^3$  cages.

Micro-CT images were reconstructed and the biggest horizontal truncation area of the refilled defect was calculated from the refilled defect volume by after-tracing the CSC edge visualized by the new bone formation, using the system software and a threshold of 110 in gray scale.

The simulation was designed on the basis of the animal experiments. The model, obtained using CT, Photoshop 5.0,

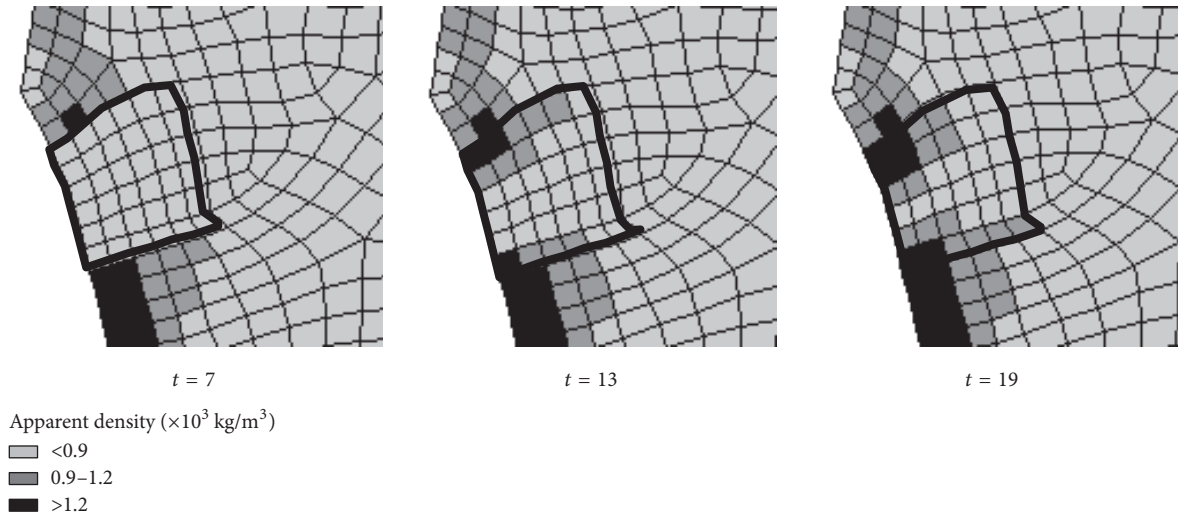


FIGURE 3: Apparent osteogenic density changes with  $E = 1000$  MPa and  $t = 20$  days.

and ANSYS 10.0 software, was based experimentally on the metaphyseal bone of the proximal left femur in rats. The implant material properties used were as follows: elastic moduli of 7000 and 2000 MPa and Poisson's ratio of 0.3 for two parts of the cortical bone; an elastic modulus of 900 MPa and Poisson's ratio of 0.3 for the cancellous bone; and an elastic modulus of 800 MPa and Poisson's ratio of 0.3 for the implant material. The joint force was assumed as 0.65 N, which is about one-third of an average rat body weight (204 g) [25]. For the material degradation time in the simulation, an iteration step length was 1 day.

### 3. Results

**3.1. Initial State.** The initial proximal femur bone density distribution was obtained, as shown in Figure 2, based on the bone self-optimization theory [30, 31]. The darker gray region in the illustration represents a larger apparent density; the black area is the cortical bone, and the gray area is the cancellous bone. There are three types of apparent densities in the indicated square area black area that were chosen as defects. Thus, this model could be used to analyze the bone with the implant material.

The iterations were terminated after the density no longer exhibited significant change (value  $< 0.001$ ) [30]. The step length was 1 day, which was set according to the material degradation and bone formation rates. An example of the apparent density change is given by Figure 3. Only the defective areas are shown because the apparent density was convergent and the rest of the structure exhibited nearly zero change. At day 7 after loading, the proportion of new bone formation is approximately zero. At days 17 and 19, the new bone formation proportions are 33.3% and 52.7%, respectively. As the biomaterial degrades, new bone is grown.

**3.2. Effects of Material Properties and Degradation Frequency on Osteogenic Simulation.** The impact of the average elastic moduli for different implant materials on osteogenesis is

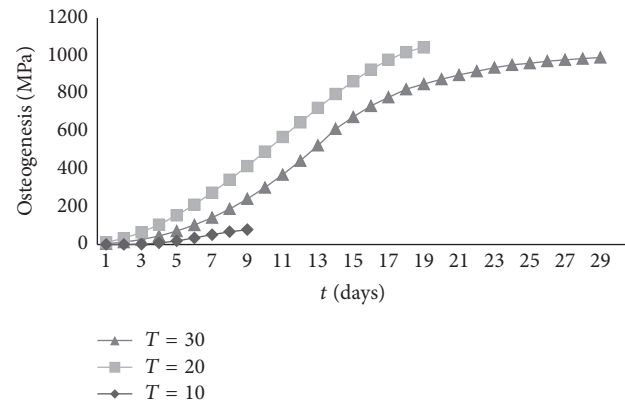


FIGURE 4: Contrast simulation results for osteogenesis using implant materials with different degradation periods.

shown in [27]. The osteogenesis rate approaches zero when  $E = 0.002$  MPa and the osteogenic effects are reduced compared with those of the stiffer material when  $E = 30$  MPa. During the same degradation period of 20 days, the effects of the material with an elastic modulus of about 1000 MPa are improved compared with those of materials having either higher or lower elastic modulus values. Finally, at the highest simulated elastic modulus of 3000 MPa, the rate of osteogenesis is reduced because the material degrades more slowly and there is no space for new bone growth.

Because optimal osteogenesis occurred at an elastic modulus of 1000 MPa, we used a material with this elastic modulus value to assess the effects of three degradation periods. The osteogenesis simulation results using implantation materials with different degradation periods at an elastic modulus of 1000 MPa are shown in Figure 4. Interestingly, we observe optimal osteogenesis when the degradation period is 20 days. When the degradation period is 10 days, degradation is too rapid, and the biomaterial cannot achieve maximum osteogenic effects. On the other hand, when the degradation

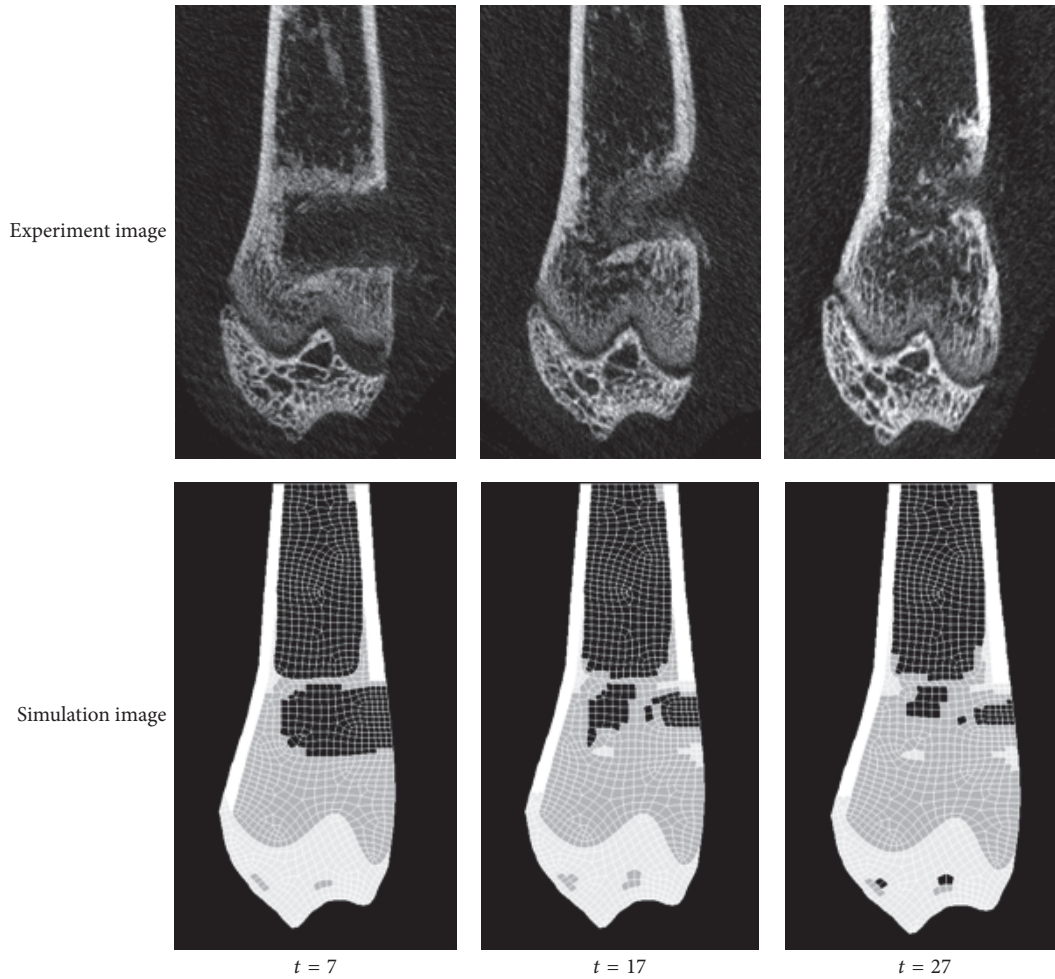


FIGURE 5: Micro-CT images from the animal experiments and simulation results showing the CSC degradation and new bone formation at  $t = 7, 17,$  and  $27$  days.

period is 30 days, degradation is too slow, and there is no space for new bone to form.

**3.3. Comparison with Animal Experiments.** The micro-CT images of the animal experiments and the simulation images showing the CSC degradation and new bone formation at  $t = 7, 17,$  and  $27$  days are presented in Figure 5. At day 7 after loading, the defect areas are  $7.73 \pm 0.41$  and  $8.21 \text{ mm}^2$  for the control and the simulation, respectively. At day 17, the refilled defect areas are reduced in both the control ( $6.31 \pm 0.43 \text{ mm}^2$ ) and the simulation ( $6.70 \text{ mm}^2$ ) and yet further reduced on day 27 ( $3.99 \pm 0.35$  and  $4.01 \text{ mm}^2$ , respectively). The simulation results are well fitted to the experimental data.

## 4. Conclusions

Based on the theories and methods of Beaupré et al. [15, 24], we introduced a material degradation function which allowed us to develop methods that would numerically simulate and optimize bone growth after biomaterial implantation. These methods accurately described the bone density distribution

after bone material implantation over time, thereby permitting us to propose theories and simulation techniques for bones in abnormal states. In this study, we verified that the implanted material may help defective bones to adapt to external loading and then quantitatively demonstrated that the bone adaptation to external loading had major effects on bone growth and followed Wolff's law.

The computer simulation provided a quantitative analysis method for resolving two basic but complementary problems between an implant material and bone growth: (1) quantifying the effects of the implant material and (2) finding a suitable biodegradable material. Compared to using animal experiments, we could reduce a 30-day study period to several hours via the computer simulation. Although degradation functions cannot precisely model how implant materials will behave, the simulation process uses discretized data with points chosen from journal references.

For simulation purposes, the degradation rate of the implant material was assumed to be constant; this may be achieved experimentally by using porous materials. However, due to the use of composite materials and the irregular shape of an implant, degradation will not be uniform across the bulk

of the implant material. As a result, the next step will be to perform a prospective study based on the stimulation results, considering properties such as the dimensions, proportions, and structure of the material. Assuming that the material is isotropic simplifies the quantitative analyses of material degradation and bone growth; however, the anisotropic properties of the material will need to be considered later. Based on these studies, a more accurate and reasonable degradation analysis can be established by introducing more parameters into the degradation distribution function which will better fit the experimental results.

Application of the bone remodeling theory aided by computationally iterated simulation allows for the calculation of bone density, osteogenesis, and the development of defective bones. This may be helpful for planning during surgery and for the prediction of postoperative bone growth. Although these bone remodeling simulations are still rudimentary, bone remodeling theories are expected to become more refined as our understanding of 3D modeling and complex loading is improved. The applications of these data will be broad, particularly after improvement of the numerical simulation technology.

## Competing Interests

The authors of this paper declare no conflict of interests.

## Acknowledgments

This work was jointly supported by the National Natural Science Foundation of China (Grant nos. 61304123 and 81320108018), the Specialized Research Fund for the Doctoral Program of Higher Education of China (no. 20133201120022), Jiangsu Province, two postdoctoral research funding schemes (nos. I202046C and 2013M541722), and a project funded by the Priority Academic Program Development of Jiangsu Higher Education Institutions.

## References

- [1] C. S. Florio, "Development of a widely applicable gradientless shape optimization based bone adaptation model for comparative parametric studies," *Structural and Multidisciplinary Optimization*, vol. 52, no. 1, pp. 157–177, 2015.
- [2] N. A. Campbell, *Biology*, Benjamin Cummings, New York, NY, USA, 3rd edition, 1993.
- [3] M. J. Cowan and R. G. Crystal, "Lung growth after unilateral pneumonectomy: quantitation of collagen synthesis and content," *American Review of Respiratory Disease*, vol. 111, pp. 267–276, 1975.
- [4] Y. C. Fung, *Biomechanics: Motion, Flow, Stress, and Growth*, Springer, New York, NY, USA, 1990.
- [5] H. Roesler, "The history of some fundamental concepts in bone biomechanics," *Journal of Biomechanics*, vol. 20, no. 11-12, pp. 1025–1034, 1987.
- [6] S. C. Cowin, Ed., *Bone Mechanics Handbook*, Informa Healthcare, New York, NY, USA, 2nd edition, 2008.
- [7] R. R. Archer and B. F. Wilson, "Mechanics of the compression wood response," *Plant Physiology*, vol. 46, no. 4, pp. 550–556, 1970.
- [8] J. Wolff, *The Law of Bone Remodeling [Translated from the 1892 Original, Das Gesetz der Transformation der Knochen, by P. Maquet and R. Furlong]*, Springer, Berlin, Germany, 1986.
- [9] D. R. Carter and W. C. Hayes, "The behavior of bone as a two-phase porous structure," *Journal of Bone and Joint Surgery A*, vol. 59, no. 7, pp. 954–962, 1977.
- [10] D. R. Carter, "Mechanical loading histories and cortical bone remodeling," *Calcified Tissue International*, vol. 36, no. 1, pp. S19–S24, 1984.
- [11] M. P. Bendsøe, "Optimal shape design as a material distribution problem," *Structural Optimization*, vol. 1, no. 4, pp. 193–202, 1989.
- [12] W. C. Hayes and B. Snyder, "Toward a quantitative formulation of Wolff's law in trabecular bone," in *Mechanical Properties of Bone*, S. C. Cowin, Ed., vol. 45, pp. 43–68, American Society of Mechanical Engineers, New York, NY, USA, 1981.
- [13] J.-M. Rossi and S. Wendling-Mansuy, "A topology optimization based model of bone adaptation," *Computer Methods in Biomechanics and Biomedical Engineering*, vol. 10, no. 6, pp. 419–427, 2007.
- [14] H. Weinans, R. Huiskes, and H. J. Grootenboer, "The behavior of adaptive bone-remodeling simulation models," *Journal of Biomechanics*, vol. 25, no. 12, pp. 1425–1441, 1992.
- [15] G. S. Beaupré, T. E. Orr, and D. R. Carter, "An approach for time-dependent bone modeling and remodeling—theoretical development," *Journal of Orthopaedic Research*, vol. 8, no. 5, pp. 651–661, 1990.
- [16] C. Boyle and I. Y. Kim, "Three-dimensional micro-level computational study of Wolff's law via trabecular bone remodeling in the human proximal femur using design space topology optimization," *Journal of Biomechanics*, vol. 44, no. 5, pp. 935–942, 2011.
- [17] J. E. Zins, A. Moreira-Gonzalez, A. Parikh, E. Arslan, T. Bauer, and M. Siemionow, "Biomechanical and histologic evaluation of the Norian craniofacial repair system and Norian Craniofacial Repair System Fast Set Putty in the long-term reconstruction of full-thickness skull defects in a sheep model," *Plastic and Reconstructive Surgery*, vol. 121, no. 5, pp. 271e–282e, 2008.
- [18] J. Zhao, G. Shen, C. Liu et al., "Enhanced healing of rat calvarial defects with sulfated chitosan-coated calcium-deficient hydroxyapatite/bone morphogenetic protein 2 scaffolds," *Tissue Engineering Part A*, vol. 18, no. 1-2, pp. 185–197, 2012.
- [19] V. I. Sikavitsas, J. S. Temenoff, and A. G. Mikos, "Biomaterials and bone mechanotransduction," *Biomaterials*, vol. 22, no. 19, pp. 2581–2593, 2001.
- [20] X. Lu and Y. Leng, "Theoretical analysis of calcium phosphate precipitation in simulated body fluid," *Biomaterials*, vol. 26, no. 10, pp. 1097–1108, 2005.
- [21] V. A. Stadelmann, C. M. Conway, and S. K. Boyd, "In vivo monitoring of bone-implant bond strength by microCT and finite element modelling," *Computer Methods in Biomechanics and Biomedical Engineering*, vol. 16, no. 9, pp. 993–1001, 2013.
- [22] C.-F. Cao, J.-J. Zhou, J.-H. Pang, and X.-Q. Chen, "A five-year clinical and radiographic follow-up of bipolar hip arthroplasty with insertion of a porous-coated anatomic femoral component without cement," *Orthopaedic Surgery*, vol. 3, no. 2, pp. 88–94, 2011.

- [23] H. Kihara, M. Shiota, Y. Yamashita, and S. Kasugai, "Biodegradation process of  $\alpha$ -TCP particles and new bone formation in a rabbit cranial defect model," *Journal of Biomedical Materials Research—Part B Applied Biomaterials*, vol. 79, no. 2, pp. 284–291, 2006.
- [24] G. S. Beaupré, T. E. Orr, and D. R. Carter, "An approach for time-dependent bone modeling and remodeling—application: a preliminary remodeling simulation," *Journal of Orthopaedic Research*, vol. 8, no. 5, pp. 662–670, 1990.
- [25] J. Zhang, L. Wang, W. Zhang, M. Zhang, and Z.-P. Luo, "Synchronization of calcium sulphate cement degradation and new bone formation is improved by external mechanical regulation," *Journal of Orthopaedic Research*, vol. 33, no. 5, pp. 685–691, 2015.
- [26] W. Annicchiarico, G. Martinez, and M. Cerrolaza, "Boundary elements and  $\beta$ -spline surface modeling for medical applications," *Applied Mathematical Modelling*, vol. 31, no. 2, pp. 194–208, 2007.
- [27] W. Lan, Z. Wen, Y. Hui-Lin, and L. Zong-Ping, "Osteogenesis effect of biomaterials analyzed using topology optimization," in *Proceedings of the 34th Chinese Control Conference (CCC '15)*, pp. 2765–2768, IEEE, Hangzhou, China, July 2015.
- [28] C. Y. Lin, N. Kikuchi, and S. J. Hollister, "A novel method for biomaterial scaffold internal architecture design to match bone elastic properties with desired porosity," *Journal of Biomechanics*, vol. 37, no. 5, pp. 623–636, 2004.
- [29] A. H. Dewi, I. D. Ana, J. Wolke, and J. Jansen, "Behavior of plaster of Paris-calcium carbonate composite as bone substitute. A study in rats," *Journal of Biomedical Materials Research—Part A*, vol. 101, no. 8, pp. 2143–2150, 2013.
- [30] H. Rojban, M. Nyan, K. Ohya, and S. Kasugai, "Evaluation of the osteoconductivity of  $\alpha$ -tricalcium phosphate,  $\beta$ -tricalcium phosphate, and hydroxyapatite combined with or without simvastatin in rat calvarial defect," *Journal of Biomedical Materials Research—Part A*, vol. 98, no. 4, pp. 488–498, 2011.
- [31] A. Roshan-Ghias, F. M. Lambers, M. Gholam-Rezaee, R. Müller, and D. P. Pioletti, "In vivo loading increases mechanical properties of scaffold by affecting bone formation and bone resorption rates," *Bone*, vol. 49, no. 6, pp. 1357–1364, 2011.
- [32] A. J. Wagoner Johnson and B. A. Herschler, "A review of the mechanical behavior of CaP and CaP/polymer composites for applications in bone replacement and repair," *Acta Biomaterialia*, vol. 7, no. 1, pp. 16–30, 2011.
- [33] T. M. Turner, R. M. Urban, S. Gitelis, K. N. Kuo, and G. B. J. Andersson, "Radiographic and histologic assessment of calcium sulfate in experimental animal models and clinical use as a resorbable bone-graft substitute, a bone-graft expander, and a method for local antibiotic delivery. One institution's experience," *Journal of Bone and Joint Surgery A*, vol. 83, no. 2, pp. S8–S18, 2001.
- [34] P. A. Glazer, U. M. Spencer, R. N. Alkalay, and J. Schwardt, "In vivo evaluation of calcium sulfate as a bone graft substitute for lumbar spinal fusion," *The Spine Journal*, vol. 1, no. 6, pp. 395–401, 2001.
- [35] Y. Murashima, G. Yoshikawa, R. Wadachi, N. Sawada, and H. Suda, "Calcium sulphate as a bone substitute for various osseous defects in conjunction with apicectomy," *International Endodontic Journal*, vol. 35, no. 9, pp. 768–774, 2002.
- [36] P. J. Rao, M. H. Pelletier, W. R. Walsh, and R. J. Mobbs, "Spine interbody implants: material selection and modification, functionalization and bioactivation of surfaces to improve osseointegration," *Orthopaedic Surgery*, vol. 6, no. 2, pp. 81–89, 2014.

## Review Article

# Periosteal Distraction Osteogenesis: An Effective Method for Bone Regeneration

Danyang Zhao,<sup>1</sup> Yu Wang,<sup>2</sup> and Dong Han<sup>1</sup>

<sup>1</sup>Department of Plastic and Reconstructive Surgery, Shanghai Ninth People's Hospital, Shanghai Jiao Tong University School of Medicine, No. 639, Zhizaoju Road, Shanghai 200011, China

<sup>2</sup>Department of Geriatrics, Shanghai Ninth People's Hospital, Shanghai Jiao Tong University School of Medicine, No. 639, Zhizaoju Road, Shanghai 200011, China

Correspondence should be addressed to Dong Han; 15021092831@163.com

Received 4 September 2016; Accepted 15 November 2016

Academic Editor: Changmin Hu

Copyright © 2016 Danyang Zhao et al. This is an open access article distributed under the Creative Commons Attribution License, which permits unrestricted use, distribution, and reproduction in any medium, provided the original work is properly cited.

The treatment of bone defects is challenging and controversial. As a new technology, periosteal distraction osteogenesis (PDO) uses the osteogenicity of periosteum, which creates an artificial space between the bone surface and periosteum to generate new bone by gradually expanding the periosteum with no need for corticotomy. Using the newly formed bone of PDO to treat bone defects is effective, which can not only avoid the occurrence of immune-related complications, but also solve the problem of insufficient donor. This review elucidates the availability of PDO in the aspects of mechanisms, devices, strategies, and measures. Moreover, we also focus on the future prospects of PDO and hope that PDO will be applied to the clinical treatment of bone defects in the future.

## 1. Introduction

Bone regeneration is a major challenge in the reconstructive surgery field. The commonly used therapies for bone defects are bone graft substitutes, guided bone regeneration (GBR), and distraction osteogenesis (DO). Autologous bone graft, the gold standard for the treatment of bone defects, although it can avoid the immune-related complications, is limited by donor, pain, morbidity, secondary trauma surgery, bone resorption, and osteonecrosis [1, 2]. Other graft substitutes, such as allogenic bone and biosynthetic materials, have the problem of biocompatibility, which often lead to infection, immune rejection, and implant displacement [3]. GBR is a technique that uses a layer of high molecular biological membrane as a barrier to cover bone defect; it can stop the entry of irrelevant tissues or cells and maintain the stability of blood clots to let the coagula fill the defect gap [4]. DO, also known as “the endogenous bone tissue engineering,” forms new bone by gradually separating two bone segments on the condition of osteotomy or corticotomy [5, 6]. This approach can generate sufficient osseous mass, but it is invasive for human body and has a long treatment cycle; it also easily

causes bone nonunion and fibrous ossification. Schmidt et al. [7] were the first to confirm the histological formation of new bone by periosteal distraction without corticotomy, and the conception of periosteal distraction osteogenesis (PDO) gradually arose from it.

PDO is a breakthrough after DO; it is the combination of tissue expansion and GBR, which creates an artificial space between bone surface and periosteum by expanding the periosteum, muscle, and skin at the same time (Figure 1(a)). It can avoid the occurrence of immune-related complications and solve the problem of insufficient donor; it also does not need corticotomy comparing with DO. A large number of researchers have explored the feasibility and superiority of PDO through many animal experiments (Table 1). This review will discuss the effectiveness of PDO in the aspects of mechanisms, devices, strategies, and measures.

## 2. Mechanisms of PDO

Periosteum plays a significant role both in DO and in PDO. The osteogenicity of periosteum has already been proved in DO. Kojimoto et al. [8] implanted an orthofix at tibiofibular

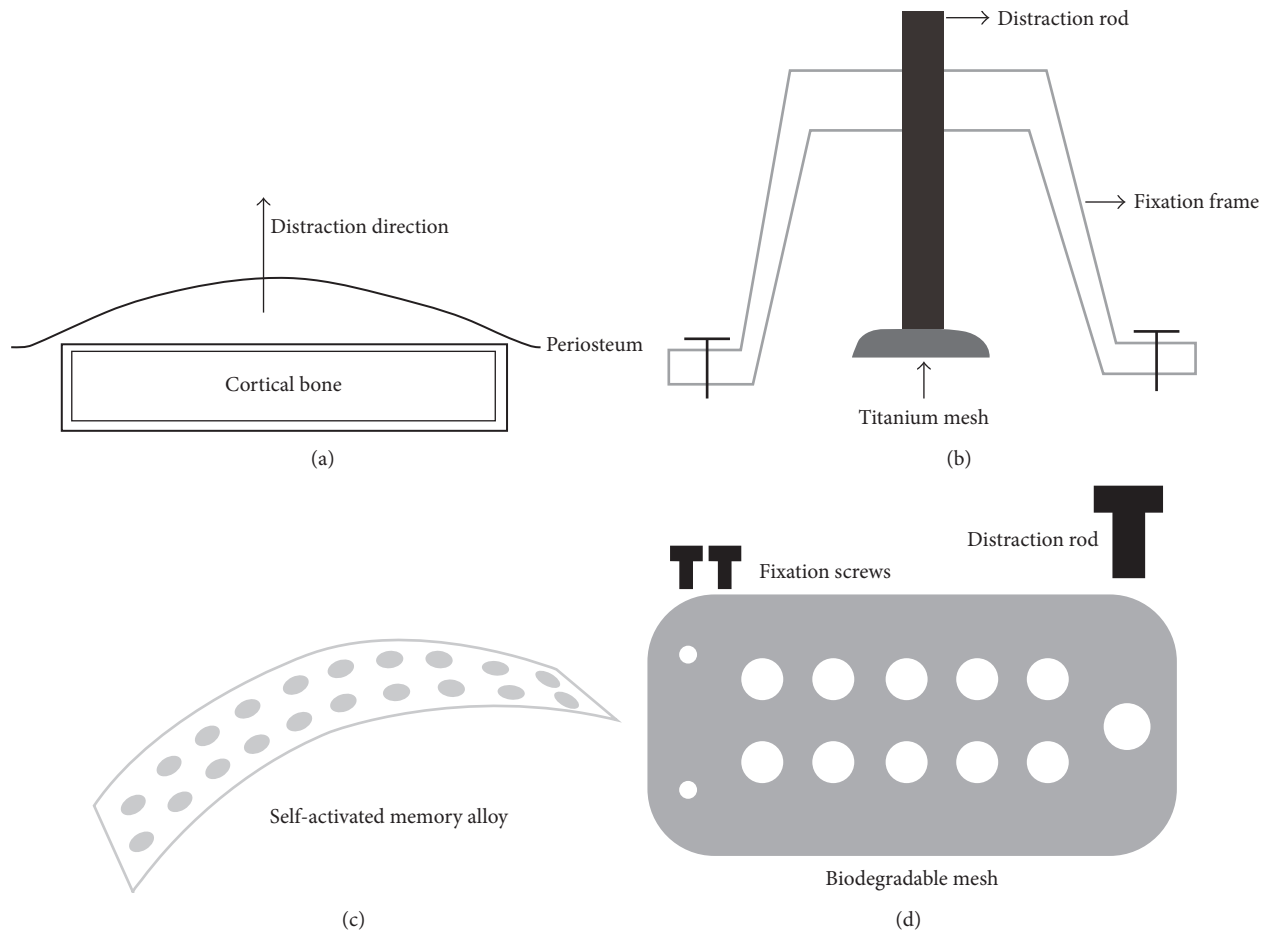


FIGURE 1: The mechanism (a) and devices (b, c, d) of PDO. (a) PDO creates an artificial space between the bone surface and periosteum to generate new bone by expanding the periosteum, muscle, and skin at the same time. (b) U-shaped distractor composes of three different parts: fixation frame, distraction rod, and titanium mesh. Bilateral fixation legs can be fixed rigidly to the surface of cortical bone by titanium screws, and then through the rotation of middle distraction rod, the titanium mesh can be lifted off the ground of bone and distract the periosteum simultaneously. (c) SMA leaves out distraction screws. (d) Biodegradable PLLA/HA mesh instead of titanium mesh for distracting periosteum.

junction in rabbit and found that removing periosteum could obviously affect callus formation, suggesting that periosteum is important for DO, even more important than corticotomy; another study also supported this finding [5]. Sun and Herring [9] regarded that the periosteal injury would inhibit the early period of mandibular DO site healing. Besides, Takeuchi et al. [10] proved that there was more newly formed bone in periosteum retention group compared with that in the periosteum excision group by micro-CT, and the preservation of periosteum could not only prevent the resorption of external bone, but also maintain vertical height of mandible during DO. Furthermore, Yin et al. [11] also stressed the necessity of maintaining the integrity of periosteum in the installation of dental implant distractor.

As we all know, the periosteum is composed of two different parts. The outer layer is also called fibrous layer, which is closely integrated by collagen fibers; it is rich in blood vessels and nerves and has nutritional and sensory function. The inner layer is also called cambium layer, which is arranged in order by osteocytes; it is involved in the growth

and proliferation of bone and has the ability of osteogenicity [12]. The periosteum is rich in bone progenitor cells which can differentiate into osteoblasts in the process of periosteum stretch [13]. An early study [14] demonstrated that the mechanical strain can stimulate human periosteal cells to increase the expression of Runt-Related Transcription Factor 2 (RUNX2) and upregulate some osteogenic and angiogenic growth factors, such as transforming growth factor- $\beta$  (TGF- $\beta$ ), basic fibroblast growth factor (b-FGF), vascular endothelial growth factor (VEGF), and platelet derived growth factor (PDGF). Thus it is theoretically possible to produce new bone only by periosteum distraction without corticotomy, namely, PDO. The slow and stable tension can activate the mesenchymal stem cells (MSCs) to differentiate into osteoblasts with high activity and even calcify to mature bone tissue.

There is another theory that supports the feasibility of PDO. Stevens et al. [16] took advantage of the osteogenicity of rabbit tibial periosteum to acquire new bone and successfully repaired the contralateral tibial defects. They called the

TABLE 1: Summary of preclinical animal experiments.

Authors	Distractor	Animal	Position	Latency period	Distraction period	Consolidation period	Factor	Year	Reference number
Kostopoulos and Karring	PTFE capsule	Rat	Mandibular ramus	0 days	Immediate distraction	7, 14 days and 1, 2, 4 weeks	Different opening direction	1995	[15]
Schmidt et al.	Titanium mesh	Rabbit	Lateral surface of the mandible	7 days	7 mm over 15 days	Days 28, 35, 42, 56	None	2002	[7]
Stevens et al.	Calcium-alginate gel	Rabbit	Anteromedial aspect of metaphyseal and diaphyseal tibia	0 days	Immediate distraction	6, 8, 12 weeks	TGF- $\beta$ /FGF-2	2005	[16]
Kessler et al.	Titanium mesh	Mimipig	Forehead region	5 days	0.5 mm/d for 10 days	7, 17, 45 days	In comparison with IE	2007	[17]
Sencimen et al.	Stainless steel device	Rabbit	Lateral surface of the mandible	7 days	0.25 mm twice a day for 10 days	15, 30, 60 days	In comparison with DO	2007	[18]
Estrada et al.	Plate supported by a screw	Rabbit	Forehead	10 days	0.25 mm/d or 0.5 mm/d until 8 mm	10, 20, 30, 40, 50, 60 days after distraction	Different distraction rates	2007	[19]
Estrada et al.	Distraction rod with base staple and titanium plate	Dog	Intraoral in the four quadrants	10 days	0.22 mm/d for 22 days	90 days	None	2007	[19]
Yamauchi et al.	Highly purified $\beta$ -TCP block	Dog	Lateral surface of the mandible	8 days	0.5 mm/d for 8 days	8 weeks	None	2008	[20]
Casap et al.	U-shaped device Made of stainless steel and titanium	Rabbit	Mandible	2 weeks	1 mm/d for 7 days	60 days	VEGF	2008	[21]
Abrahamsson et al.	Osmotic self-inflatable expander	Rabbit	Lower border of the mandible	0 days	Depend on the inflation rate of the expander	2 weeks	None	2009	[22]
Oda et al.	Titanium mesh	Rabbit	Mandible	7 days	0.5 mm/d for 8 days	4 and 8 weeks	Cortical bone perforation	2009	[23]
Lethaus et al.	Laser-perforated titanium	Mimipig	Forehead region	3 days	0.5 mm twice per day for periods 5, 10, 15 days, respectively	14, 28, 42 days	Versus static shielding	2010	[24]
Sato et al.	Mesh plate	Rabbit	Parietal bone	7 days	20 days	3 weeks	Bone marrow stem cell administration	2010	[25]

TABLE I: Continued.

Authors	Distractor	Animal	Position	Latency period	Distraction period	Consolidation period	Factor	Year	Reference number
Altuğ et al.	U-shaped distractor built from stainless steel	Rabbit	Lateral aspect of the mandible	1 day or 7 days	0.25 mm twice a day for 10 days	15, 30, 60 days	Different latency periods	2011	[26]
Zakaria et al.	Biodegradable mesh (PLLA/HA)	Rabbit	Calvarial bone	7 days	0.5 mm every 12 hours for 5 days	4 and 6 weeks	Different distraction rates	2012	[27]
Zakaria et al.	Titanium mesh	Rabbit	Calvarial bone	7 days	0.5 mm every 12 hours for 5 days	4 and 6 weeks	Different distraction rates	2012	[28]
Saulacic et al.	Hemispherical disc	Rat	Calvarial bone	7 days	0.4 mm/d for 10 days	10, 20 days	None	2013	[29]
Saulacic et al.	Occlusive distraction plate or perforation of the distraction plate	Rat	Calvaria	7 days	0.2 mm/d for 10 days	7 days	Different distractors	2013	[30]
Yamauchi et al.	Ni-Ti SMA	Rabbit	Forehead	14 days	Depend on the elasticity of SMA	3 and 6 weeks	None	2013	[31, 32]
Suer et al.	Custom-design device	Rabbit	Lateral surface of the mandibular corpus	7 days	0.25 mm Twice a day for 6 days	4 and 8 weeks	HBO	2014	[33]
Kahraman et al.	A new periosteal distractor	Rabbit	Periosteum at the forehead	7 days	7 days	0.35 mm/d for 10 days, 45 days	Simvastatin	2015	[34]
Pripratanont et al.	Modified Hyrax device	Rabbit	Ramus and body of mandible	3 days	0.5 mm twice a day for 7 days	4 and 8 weeks	PRF	2015	[35]
Saulacic et al.	Custom made distraction device	Rabbit	Calvaria	7 days	0.25 or 0.5 mm/d for 10 days	1 week, 2 weeks, 2 months	Different distraction rates	2016	[36]
Dziewiecki et al.	Nondegradable titanium device and degradable devices (poly-DL-lactide and polyglycolic acid)	Minipig	Calvarial bone	0 days	Immediate distraction	12, 28, 42 days	None	2016	[37]
Yamauchi et al.	SMA mesh device and absorbable thread	Rabbit	Under the periosteum at the forehead	0 days	Time-released dynamic distraction	4 and 8 weeks	None	2016	[38]

IE = Immediate Elevation; DO = distraction osteogenesis; SMA = self-activated memory alloy; HBO = hyperbaric oxygen; PRF = platelet-rich fibrin; PTFE = Polytetrafluoroethylene; TGF- $\beta$  = transforming growth factor- $\beta$ ; FGF-2 = fibroblast growth factor-2.

artificial space between the periosteum and the tibia “in vivo bioreactor,” which creates a space in the body and uses the organism’s own potency to regenerate tissue for repair [39]. The periosteum is equivalent to a physical barrier that effectively prevents other soft tissues from invading and is also conducive to the supplement of bone cells. Using this method to construct tissues is similar to bone autograft; it can be achieved by body’s own healing mechanism and regenerative potency.

To sum up, the mechanism of PDO lies in the formation of an “in vivo reactor” between the periosteum and cortical bone. Using the osteogenicity of periosteum, it not only releases osteogenic cells and factors during the distraction, but also creates an independent space for bone regeneration.

### 3. The Designs and Materials of Distraction Devices

In order to obtain a good result of osteogenesis, we must carry out a stable and sustained stretch for periosteum. Researchers often used different designs and materials to analyze the effect of PDO (Table 1). With the progress of science and technology, the distraction devices are gradually evolving.

At first, Kostopoulos and Karring [15] implanted the Teflon (PTFE) capsules at mandibular ramus of rats; the capsules could avoid the interference of the surrounding soft tissue, whereas they block the contact between the periosteum and the cortex unfortunately. They suggested that the periosteal distraction devices should be perforated in order to maintain the communication between the periosteum and cortical bone.

Schmidt et al. [7] then used a U-shaped distractor (Figure 1(b)) to stretch the periosteum of rabbit mandible and acquired new bone height of average  $2.86 \pm 0.56$  mm, and the U-shaped distractor has been improved later [18, 21, 26, 33, 36, 40]. The U-shaped device is usually made of titanium alloy or stainless steel with advantages of high strength and corrosion resistance. It often has three different parts; they are fixation frame, distraction rod, and titanium mesh. Bilateral fixation legs can be fixed rigidly to the surface of cortical bone by titanium screws. Through the middle distraction rod, the titanium mesh will be lifted off the ground of bone and distracts the periosteum simultaneously. The speed and frequency of U-shaped distractor can be controlled manually, but it often causes damage to the soft tissues, especially to the integrity of periosteum. Screw loosening and mesh disengagement also occasionally occur; thus further improvement is needed. Nowadays, the distraction devices are continuously modifying; many researchers only used a titanium mesh and few screws to achieve the same effect; those distraction devices not only simplified the operation process, but also reduced the damage to soft tissues [17, 19, 23–25, 28–30, 41].

To overcome the manual operation problem, Abrahamsson et al. [22, 42, 43] put a self-inflatable osmotic expander under the mandibular periosteum of rabbits and then placed a preformed scaffold that was filled with autogenous bone graft or bone substitute; finally the distraction

device acquired newly formed bone after three months. Yamauchi et al. [31, 32, 38] then designed a new type of self-activated memory alloy (SMA) (Figure 1(c)); it does not need distraction screws and thus solves the complications with the minimal invasion. Nonetheless, the accuracy and controllability of the above two kinds of expansion devices were relatively poor. It is difficult to guarantee the accuracy of quantitative distraction without damage to the osteogenic potential of periosteum.

Besides the designs, the materials of distraction devices are changing rapidly. In one study, biocompatible gel was injected into the space between the periosteum and tibia to distract the tibial periosteum [16]. The gel was completely degraded after 2 weeks, and there was no obvious difference between the new bone and tibial cortex by the time of 8 weeks. Yamauchi et al. [20, 44] implanted a highly purified beta-tricalcium ( $\beta$ -TCP) block on the lateral surface of the beagle dog mandible. With the degradation of material, the  $\beta$ -TCP block was gradually replaced by new bone. In another experiment, the graft which was implanted in the distracted area between the alveolar bone and  $\beta$ -TCP block could stably exist [45]. Zakaria et al. [27] then tried to use biodegradable poly-L-lactide/hydroxyapatite (PLLA/HA) mesh (Figure 1(d)) to replace the titanium mesh for distracting periosteum. Recently, Dziewiecki et al. [37] compared nondegradable titanium to degradable devices (poly-DL-lactide and polyglycolic acid) in PDO; they also proved that degradable devices could produce new bone and there were no significant differences in the amount of newly formed bone between titanium and degradable materials.

Those above measures are similar to the in vivo bone tissue engineering, yet not requiring seed cells and exogenous growth factors. They solve the problem of second operation for pulling the device out, but the choice of biodegradable materials (biodegradability and toxicity) and the stability of degradable materials need to be studied.

### 4. Effect of Distraction Strategies on the Formation of New Bone

Similar to the traditional DO [46], the strategies of PDO can be divided into three stages: latency period, distraction period, and consolidation period (Figure 2). Different stages of PDO will affect the effect of osteogenesis, but the optimal parameters, including the distraction site, have not been obtained.

*4.1. Distraction Sites.* PDO was initially applied to the distraction of atrophic or edentulous mandible for increasing the height and width of alveolar ridge and was used for endosseous implant placement [47]. In the past, most of the distraction devices were placed at the internal and external sides of the mandible, but the alveolar gap was too narrow to perform the operation, and the devices would fall off because of animals’ chewing action. Later, tibial periosteum was used to obtain new bone tissue [16]. Same as the mandibular bone, this method was limited by the size and space of osteogenesis, and the regenerated bone was insufficient to repair large bone

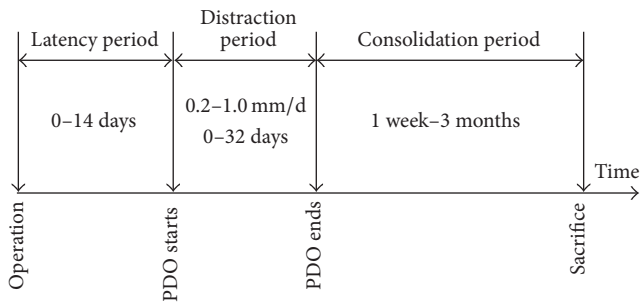


FIGURE 2: Protocol of PDO applied in different studies. The latency periods of PDO are different from 0 days to 14 days, the distraction periods of PDO are different from 0 days to 32 days, and the speed is 0.2–1.0 mm/d; the consolidation periods of PDO are different from 1 week to 3 months.

defects. In order to solve these problems, Kessler et al. [17] implanted a titanium mesh and a screw on the forehead of pig and distracted the calvarial periosteum through the dynamic rotation of the screw. On the one hand, the skull bone was flatter than other bones and the periosteum of skull was thicker than other parts of the body; on the other hand, the area was adequate and easy to separate. Using the calvarial periosteum solves the problem of insufficient source of bone tissues.

The choice of sites determines the effect of distraction. Flat bone floor and tough periosteum will greatly improve the effect of PDO. Besides, the distraction site should be kept away from the incision place as far as possible to avoid the incremental tension in the process of distraction; otherwise, the wound will tend to have a dehiscence and result in the failure of the experiment.

**4.2. The Length of Latency Period.** The latency period refers to the intermission from the placement of device to the distraction. The traditional DO has a latency period of 5–7 days, while the latency periods of PDO are different from 0 days to 14 days (Figure 2) according to the difference of materials [46, 48]. In order to evaluate the effect of different latency periods on the PDO, 7-day latency period and 1-day latency period were compared [26], and the result showed that the average new bone masses were 2.62 cm<sup>2</sup> and 3.26 cm<sup>2</sup>, respectively, but without significant difference, suggesting that bone tissue can be made by PDO using different latency periods. From another point of view, during the latency period, animals are gradually adapted to the device and the wound is also gradually healing, so it is recommended to wait for at least one week to proceed to the distraction.

**4.3. The Speed and Frequency of Distraction.** The distraction period is to separate the periosteum from the bone surface by a slow and persistent tension [46, 48]. According to Ilizarov's law of tension-stress, the speed of distraction for limb lengthening should be 1 mm every day [6]. Many researchers tend to take the speed of 0.2–1.0 mm/d in PDO (Figure 2). It is because that cells and nutrition supply simultaneously come

from the two bone ends and the surrounding periosteum in the process of DO, while in PDO, these can only come from the basal bone and periosteum; thus the speed of 1 mm/d is relatively fast.

In a study [19] that used the speed of 0.25 mm/d and 0.5 mm/d to distract the periosteum, lower speed was found to be more favorable for new bone formation. However, Saulacic et al. [36] believed that the high speed of distraction might be beneficial to periosteal osteogenesis, although it was easy to cause the disruption of wound and exposure of the device. Zakaria et al. [27, 28] designed a new type of device, by means of the inclined structure; this device could be used to study the effect of different distraction rates at the same time. The result suggested that the optimal speed of distraction should be lower than 0.33 mm/d. Low distraction speed could reduce the invasion of the surrounding soft tissues; what is more, the newly formed bone would contain relatively thicker trabecular bone and less fat tissue.

As for the frequency of distraction, the frequency of once a day, four times a day, and sixty times a day were used to study the effect of different distraction speeds on limb elongation [6], and the result showed that 1 mm/d with four steps once a day was the best for DO. However, researchers often used the frequency of once a day or twice a day in the process of PDO, though there was no relevant literature to carry out a comparative study.

**4.4. Dynamic Distraction versus Static Distraction.** In the process of PDO, scholars carried out a lot of comparative works on the dynamic and static distraction. Static distraction achieves the desired height all at once, while dynamic distraction adopts a more gentle way to distract separately. Kessler et al. [17] found that the dynamic distraction was more favorable for early bone formation, and the newly formed bone was similar to the rows of micropillars in conventional DO, while the immediate distraction could just produce the woven bone. Lethaus et al. [24] put the distraction device under the calvarial bone, the result showed that the cumulative bone mass was about 66% in dynamic group and 67% in static group, and there were no significant differences between the two groups with regard to bone quality or quantity. Yamauchi et al. [38] used a SMA mesh device and an absorbable thread to conduct dynamic distraction; result showed that dynamic distraction group had higher volume of newly formed bone by comparing with simple SMA group.

Generally speaking, dynamic distraction might be more moderate, which can avoid damage to the osteogenic potential of periosteum when the stretch is excessive.

## 5. Measures to Promote the Formation of New Bone in PDO

Researchers conducted a lot of different explorations to increase the quality and quantity of osteogenesis, such as cortical bone perforation, MSCs administration, addition of different cytokines, and so on (Table 1). These technical improvements not only confirmed the feasibility of PDO, but also provided valuable information for improving PDO.

**5.1. Cortical Bone Perforation.** Cortical bone perforation is a big step in GBR, and PDO takes advantages of it to promote new bone formation. Exposure of cancellous bone by perforating on bone surface facilitates the release of MSCs from bone marrow or endosteum. Meanwhile, the increase of bleeding allows the angioblast cells to enter the space under periosteum, which is beneficial to the vascularization of newly formed bone.

Sencimen et al. [18] compared PDO with conventional DO in New Zealand male rabbits; they found that the newly formed bone was  $14.4 \text{ mm}^2$  in PDO group, compared with  $25.4 \text{ mm}^2$  in DO group; moreover, the formation of new bone in the DO group was more compact, while the formation of new bone in PDO group was rich in adipose tissue. Oda et al. [23] used a titanium mesh and a screw to distract the periosteum of mandible in rabbits; the average area of the new bone was  $25.7 \pm 5.1 \text{ mm}^2$  and  $12.9 \pm 3.2 \text{ mm}^2$  with or without decortication at 8 weeks after distraction period. The new bone could be seen under the whole mesh in the decortication group, but in the control group, the new bone could only be seen near the distraction screw; it might be because the local environment around the screw was similar to the experimental group, suggesting that cortical bone perforation was beneficial to bone expansion in PDO. Yamauchi et al. [32] united the technologies of bone perforation and SMA to carry on PDO to a height of  $2.9 \pm 0.5 \text{ mm}$  and found that the new bone mass in experimental group was higher than that in the control group in each period. In the study of the osteogenetic effect in PDO, Saulacic et al. [30] considered that if the bone marrow cavity was not exposed, the new bone mainly depended on the periosteum; on the contrary, it would depend on bone cortex. We can conclude that cortical bone perforation influences the formation of new bone in PDO.

**5.2. MSCs Administration.** MSCs administration is actually the same as cortical bone perforation that can overcome the shortage of osteoblasts. MSCs not only participate in osteogenesis, but also produce enough VEGF to promote the formation of new blood vessels [49]. Sato et al. [25] injected MSCs into the space under the periosteum during PDO and the result showed that the volume, height, and degree of mineralization of the new bone in experiment group were higher than noninjected group, suggesting that MSCs administration could induce osteogenesis at periosteal distraction sites. However, it is necessary to explore the optimal injection time and frequency in the future.

**5.3. Cytokines.** In DO, the application of cytokines has obtained achievements, but in PDO, the study in this area is far from enough. VEGF, as a vascular growth factor, not only is conducive to the formation of blood vessels, but also can promote osteogenesis during the process of distraction [50, 51]; the injection of exogenous VEGF was proved to be beneficial to bone formation in PDO [21]. Another study [35] proved that the newly formed bone by PDO was more mature after adding platelet-rich fibrin (PRF). In addition, PDO could also induce the release of endogenous bone morphogenetic protein-2 (BMP-2) [36]. We have reason

to believe that adding other biological factors which can promote the osteogenesis of DO, such as TGF- $\beta$ , bFGF, and PDGF, can also improve the osteogenesis of PDO.

**5.4. Other Measures.** In recent years, researchers are still exploring other measures to improve PDO. One study found the bone formation was delayed and the new bone mineralization was insufficient in the ovaries-resected rabbits, but there was no significant histological difference compared with the control group [40], which indicated that the osteoporosis causing by decreased estrogen did not affect the new bone formation in PDO. Hyperbaric oxygen (HPO) was proved to be beneficial to PDO [33]. HPO therapy could improve the oxygen partial pressure in the blood and tissues, which could promote the synthesis of bone [52]. Kahraman et al. [34] made a local application of simvastatin when implanted distraction device, but there was not enough evidence to show that the use of lipid-lowering agents can promote the formation of new bone in PDO.

## 6. Future Directions and Prospects

The choice of materials, devices, and strategies is all variables in preclinical studies; for future preclinical work, those variables should be tuned to further optimize outcomes. The periosteum is a deeper implantation site and provides less available volume for osteogenesis, so the implantation site is very important; the periosteum should be thicker and enough implantation area is also needed. PDO still has a long period; it is necessary to promote the formation of new bone in PDO. MSCs and growth factors are promising; cortical bone perforation should be careful because it is hard to control and thus easily cause damage to the bone.

The biodegradable distraction devices seem to have advantages in PDO; nanomaterial is a potential candidate, because it can deliver drugs, growth factors, and genes with high efficiency [53, 54], which can be used for promoting cell proliferation, survival, and differentiation in bone regeneration. Future research should focus on the biodegradability, toxicity, and the stability of biodegradable materials. Besides, three-dimensional (3D) printing is a new technique with great potential in regeneration of tissues and organs [55, 56]; the distraction devices can be designed accurately by 3D printing technique to form complex shapes; what is more, 3D printing can design different sizes of holes in distraction devices to keep the communication between the periosteum and the cortex. On the whole, 3D printing technique designed biodegradable materials can combine with stem cells, growth factors, regenerative drugs, or other measures to produce sufficient amount of bone tissue; this might have great potential to achieve functional and aesthetic repair for bone defects.

## 7. Conclusion

There are still many disputes in the treatments of bone defects; as outlined above, PDO undoubtedly has fine application prospect. This review elucidates the advantages of PDO in

the formation of new bone from the aspects of mechanisms, devices, strategies, and measures. At present, the technology of PDO has been used in the treatments of atrophic alveolar ridge and cleft palate, but there exist rare clinical reports; this might be attributed to device instability, soft tissues injury, infection, and other complications. Theoretically, newly formed bone by PDO can be applied to the bone defects in all parts of the body caused by hyperparathyroidism, calcium metabolism disorder, rickets, trauma, infection, and congenital malformation or other pathological conditions.

## Competing Interests

The authors declare that there is no conflict of interests regarding the publication of this paper.

## Authors' Contributions

Danyang Zhao and Yu Wang contributed equally to this study as co-first authors.

## Acknowledgments

This review was supported by the Natural Science Foundation of China (NSFC; Project nos. 81272132, 81571944).

## References

- [1] J. T. Marino and B. H. Ziran, "Use of solid and cancellous autologous bone graft for fractures and nonunions," *Orthopedic Clinics of North America*, vol. 41, no. 1, pp. 15–26, 2010.
- [2] H. C. Pape, A. Evans, and P. Kobbe, "Autologous bone graft: properties and techniques," *Journal of Orthopaedic Trauma*, vol. 24, no. 1, pp. S36–S40, 2010.
- [3] P. Patka, H. J. Haarman, and F. C. Bakker, "Bone transplantation and bone replacement materials," *Nederlands Tijdschrift voor Geneeskunde*, vol. 142, no. 16, pp. 893–896, 1998.
- [4] R. Dimitriou, G. I. Mataliotakis, G. M. Calori, and P. V. Giannoudis, "The role of barrier membranes for guided bone regeneration and restoration of large bone defects: current experimental and clinical evidence," *BMC Medicine*, vol. 10, article 81, 2012.
- [5] G. A. Ilizarov, "The tension-stress effect on the genesis and growth of tissues. Part I. The influence of stability of fixation and soft-tissue preservation," *Clinical Orthopaedics and Related Research*, no. 238, pp. 249–281, 1989.
- [6] G. A. Ilizarov, "The tension-stress effect on the genesis and growth of tissues. Part II. The influence of the rate and frequency of distraction," *Clinical Orthopaedics and Related Research*, no. 239, pp. 263–285, 1989.
- [7] B. L. Schmidt, L. Kung, C. Jones, and N. Casap, "Induced osteogenesis by periosteal distraction," *Journal of Oral and Maxillofacial Surgery*, vol. 60, no. 10, pp. 1170–1175, 2002.
- [8] H. Kojimoto, N. Yasui, T. Goto, S. Matsuda, and Y. Shimomura, "Bone lengthening in rabbits by callus distraction. The role of periosteum and endosteum," *Journal of Bone and Joint Surgery—B*, vol. 70, no. 4, pp. 543–549, 1988.
- [9] Z. Sun and S. W. Herring, "The effect of periosteal injury and masticatory micromovement on the healing of a mandibular distraction osteogenesis site," *Archives of Oral Biology*, vol. 54, no. 3, pp. 205–215, 2009.
- [10] S. Takeuchi, A. Matsuo, and H. Chiba, "Beneficial role of periosteum in distraction osteogenesis of mandible: its preservation prevents the external bone resorption," *Tohoku Journal of Experimental Medicine*, vol. 220, no. 1, pp. 67–75, 2010.
- [11] X. Yin, C. Zhang, E. P. Hze-Khoong, Y. Wang, and L. Xu, "Influence of periosteal coverage on distraction osteogenesis with dental implant distractors," *Journal of Oral and Maxillofacial Surgery*, vol. 72, no. 10, pp. 1921–1927, 2014.
- [12] G. Augustin, A. Antabak, and S. Davila, "The periosteum. Part I: anatomy, histology and molecular biology," *Injury*, vol. 38, no. 10, pp. 1115–1130, 2007.
- [13] C. A. L. Bassett and T. P. Ruedi, "Transformation of fibrous tissue to bone in vivo," *Nature*, vol. 209, no. 5027, pp. 988–989, 1966.
- [14] T. Kanno, T. Takahashi, W. Ariyoshi, T. Tsujisawa, M. Haga, and T. Nishihara, "Tensile mechanical strain up-regulates Runx2 and osteogenic factor expression in human periosteal cells: implications for distraction osteogenesis," *Journal of Oral and Maxillofacial Surgery*, vol. 63, no. 4, pp. 499–504, 2005.
- [15] L. Kostopoulos and T. Karring, "Role of periosteum in the formation of jaw bone. An experiment in the rat," *Journal of Clinical Periodontology*, vol. 22, no. 3, pp. 247–254, 1995.
- [16] M. M. Stevens, R. P. Marini, D. Schaefer, J. Aronson, R. Langer, and V. P. Shastri, "In vivo engineering of organs: the bone bioreactor," *Proceedings of the National Academy of Sciences of the United States of America*, vol. 102, no. 32, pp. 11450–11455, 2005.
- [17] P. Kessler, L. Bumiller, A. Schlegel, T. Birkholz, F. W. Neukam, and J. Wiltfang, "Dynamic periosteal elevation," *British Journal of Oral and Maxillofacial Surgery*, vol. 45, no. 4, pp. 284–287, 2007.
- [18] M. Sencimen, Y. S. Aydin, K. Ortakoglu, Y. Karslioglu, O. Gunhan, and Y. Gunaydin, "Histomorphometrical analysis of new bone obtained by distraction osteogenesis and osteogenesis by periosteal distraction in rabbits," *International Journal of Oral and Maxillofacial Surgery*, vol. 36, no. 3, pp. 235–242, 2007.
- [19] J. I. C. Estrada, N. Saulacic, L. Vazquez, T. Lombardi, J. U. C. Ramirez, and J. P. Bernard, "Periosteal distraction osteogenesis: preliminary experimental evaluation in rabbits and dogs," *British Journal of Oral and Maxillofacial Surgery*, vol. 45, no. 5, pp. 402–405, 2007.
- [20] K. Yamauchi, T. Takahashi, K. Funaki, and Y. Yamashita, "Periosteal expansion osteogenesis using highly purified beta-tricalcium phosphate blocks: a pilot study in dogs," *Journal of Periodontology*, vol. 79, no. 6, pp. 999–1005, 2008.
- [21] N. Casap, N. B. Venezia, A. Wilensky, and Y. Samuni, "VEGF facilitates periosteal distraction-induced osteogenesis in rabbits: a micro-computerized tomography study," *Tissue Engineering—Part A*, vol. 14, no. 2, pp. 247–253, 2008.
- [22] P. Abrahamsson, S. Isaksson, M. Gordh, and G. Andersson, "Periosteal expansion of rabbit mandible with an osmotic self-inflatable expander," *Scandinavian Journal of Plastic and Reconstructive Surgery and Hand Surgery*, vol. 43, no. 3, pp. 121–125, 2009.
- [23] T. Oda, K. Kinoshita, and M. Ueda, "Effects of cortical bone perforation on periosteal distraction: an experimental study in the rabbit mandible," *Journal of Oral and Maxillofacial Surgery*, vol. 67, no. 7, pp. 1478–1485, 2009.
- [24] B. Lethaus, C. Tudor, L. Bumiller, T. Birkholz, J. Wiltfang, and P. Kessler, "Guided bone regeneration: dynamic procedures versus

- static shielding in an animal model,” *Journal of Biomedical Materials Research Part B: Applied Biomaterials*, vol. 95, no. 1, pp. 126–130, 2010.
- [25] K. Sato, N. Haruyama, Y. Shimizu, J. Hara, and H. Kawamura, “Osteogenesis by gradually expanding the interface between bone surface and periosteum enhanced by bone marrow stem cell administration in rabbits,” *Oral Surgery, Oral Medicine, Oral Pathology, Oral Radiology and Endodontology*, vol. 110, no. 1, pp. 32–40, 2010.
- [26] H. A. Altuğ, Y. S. Aydıntuğ, M. Şençimen et al., “Histomorphometric analysis of different latency periods effect on new bone obtained by periosteal distraction: an experimental study in the rabbit model,” *Oral Surgery, Oral Medicine, Oral Pathology, Oral Radiology and Endodontology*, vol. 111, no. 5, pp. 539–546, 2011.
- [27] O. Zakaria, K. Kon, and S. Kasugai, “Evaluation of a biodegradable novel periosteal distractor,” *Journal of Biomedical Materials Research Part B: Applied Biomaterials*, vol. 100, no. 3, pp. 882–889, 2012.
- [28] O. Zakaria, M. Madi, and S. Kasugai, “Induced osteogenesis using a new periosteal distractor,” *Journal of Oral and Maxillofacial Surgery*, vol. 70, no. 3, pp. e225–e234, 2012.
- [29] N. Saulacic, B. Schaller, T. Iizuka, D. Buser, C. Hug, and D. D. Bosshardt, “Analysis of new bone formation induced by periosteal distraction in a rat calvarium model,” *Clinical Implant Dentistry and Related Research*, vol. 15, no. 2, pp. 283–291, 2013.
- [30] N. Saulacic, C. Hug, D. D. Bosshardt et al., “Relative contributions of osteogenic tissues to new bone formation in periosteal distraction osteogenesis: histological and histomorphometrical evaluation in a rat Calvaria,” *Clinical Implant Dentistry and Related Research*, vol. 15, no. 5, pp. 692–706, 2013.
- [31] K. Yamauchi, T. Takahashi, K. Tanaka et al., “Self-activated mesh device using shape memory alloy for periosteal expansion osteogenesis,” *Journal of Biomedical Materials Research*, vol. 101, no. 5, pp. 736–742, 2013.
- [32] K. Yamauchi, S. Nogami, K. Tanaka et al., “The effect of decortication for periosteal expansion osteogenesis using shape memory alloy mesh device,” *Clinical Implant Dentistry and Related Research*, vol. 17, pp. e376–e384, 2015.
- [33] B. T. Suer, K. Ortakoglu, Y. Gunaydin et al., “Effects of the hyperbaric oxygen on de novo bone formation during periosteal distraction,” *Journal of Craniofacial Surgery*, vol. 25, no. 5, pp. 1740–1745, 2014.
- [34] O. E. Kahraman, O. Erdogan, H. Namlı, and L. Sencar, “Effects of local simvastatin on periosteal distraction osteogenesis in rabbits,” *British Journal of Oral and Maxillofacial Surgery*, vol. 53, no. 4, pp. e18–e22, 2015.
- [35] P. Pripatnanont, F. Balabid, S. Pongpanich, and S. Vongvatcharanon, “Effect of osteogenic periosteal distraction by a modified Hyrax device with and without platelet-rich fibrin on bone formation in a rabbit model: a pilot study,” *International Journal of Oral and Maxillofacial Surgery*, vol. 44, no. 5, pp. 656–663, 2015.
- [36] N. Saulacic, K. Nakahara, T. Iizuka, M. Haga-Tsujimura, W. Hofstetter, and P. Scolozzi, “Comparison of two protocols of periosteal distraction osteogenesis in a rabbit calvaria model,” *Journal of Biomedical Materials Research—Part B Applied Biomaterials*, vol. 104, no. 6, pp. 1121–1131, 2016.
- [37] D. Dziewiecki, S. Van De Loo, F. Gremse et al., “Osteoneogenesis due to periosteal elevation with degradable and nondegradable devices in Göttingen Minipigs,” *Journal of Cranio-Maxillofacial Surgery*, vol. 44, no. 3, pp. 318–324, 2016.
- [38] K. Yamauchi, S. Nogami, G. Martinez-de la Cruz et al., “Timed-release system for periosteal expansion osteogenesis using NiTi mesh and absorbable material in the rabbit calvaria,” *Journal of Cranio-Maxillofacial Surgery*, vol. 44, no. 9, pp. 1366–1372, 2016.
- [39] K. Dhaliwal, R. Kunchur, and R. Farhadieh, “Review of the cellular and biological principles of distraction osteogenesis: an in vivo bioreactor tissue engineering model,” *Journal of Plastic, Reconstructive & Aesthetic Surgery*, vol. 69, no. 2, pp. e19–e26, 2016.
- [40] G. R. Bayar, Y. Gunaydin, K. Ortakoglu, O. Gunhan, Y. S. Aydıntuğ, and M. Sencimen, “Histomorphometric analysis of new bone obtained by osteogenic periosteal distraction in ovariectomized rabbits,” *Oral Surgery, Oral Medicine, Oral Pathology and Oral Radiology*, vol. 113, no. 4, pp. 472–479, 2012.
- [41] C. Tudor, L. Bumiller, T. Birkholz, P. Stockmann, J. Wiltfang, and P. Kessler, “Static and dynamic periosteal elevation: a pilot study in a pig model,” *International Journal of Oral and Maxillofacial Surgery*, vol. 39, no. 9, pp. 897–903, 2010.
- [42] P. Abrahamsson, S. Isaksson, M. Gordh, and G. Andersson, “Onlay bone grafting of the mandible after periosteal expansion with an osmotic tissue expander: an experimental study in rabbits,” *Clinical Oral Implants Research*, vol. 21, no. 12, pp. 1404–1410, 2010.
- [43] P. Abrahamsson, S. Isaksson, and G. Andersson, “Guided bone generation in a rabbit mandible model after periosteal expansion with an osmotic tissue expander,” *Clinical Oral Implants Research*, vol. 22, no. 11, pp. 1282–1288, 2011.
- [44] K. Yamauchi, T. Takahashi, K. Funaki, Y. Hamada, and Y. Yamashita, “Histological and histomorphometrical comparative study of  $\beta$ -tricalcium phosphate block grafts and periosteal expansion osteogenesis for alveolar bone augmentation,” *International Journal of Oral and Maxillofacial Surgery*, vol. 39, no. 10, pp. 1000–1006, 2010.
- [45] K. Yamauchi, T. Takahashi, K. Funaki, I. Miyamoto, and Y. Yamashita, “Implant placement for periosteal expansion osteogenesis using  $\beta$ -tricalcium phosphate block: an experimental study in dogs,” *Oral Surgery, Oral Medicine, Oral Pathology, Oral Radiology and Endodontology*, vol. 108, no. 6, pp. 861–866, 2009.
- [46] A. A. Efunkoya, B. O. Bamgbose, R. A. Adebola, J. B. Adeoye, and I. O. Akpasa, “Maxillomandibular distraction osteogenesis,” *Journal of Craniofacial Surgery*, vol. 25, no. 5, pp. 1787–1792, 2014.
- [47] T. Nakano and H. Yatani, “Bone augmentation of dental implant treatment,” *Clinical Calcium*, vol. 17, no. 2, pp. 256–262, 2007.
- [48] G. Swennen, R. Dempf, and H. Schliephake, “Cranio-facial distraction osteogenesis: a review of the literature. Part II: experimental studies,” *International Journal of Oral and Maxillofacial Surgery*, vol. 31, no. 2, pp. 123–135, 2002.
- [49] Y. Wu, L. Chen, P. G. Scott, and E. E. Tredget, “Mesenchymal stem cells enhance wound healing through differentiation and angiogenesis,” *Stem Cells*, vol. 25, no. 10, pp. 2648–2659, 2007.
- [50] T. Nishisho, K. Yukata, Y. Matsui et al., “Angiogenesis and myogenesis in mouse tibialis anterior muscles during distraction osteogenesis: VEGF, its receptors, and myogenin genes expression,” *Journal of Orthopaedic Research*, vol. 30, no. 11, pp. 1767–1773, 2012.
- [51] J. Hu, S. Zou, J. Li, Y. Chen, D. Wang, and Z. Gao, “Temporoparietal expression of vascular endothelial growth factor and basic fibroblast growth factor during mandibular distraction osteogenesis,” *Journal of Cranio-Maxillofacial Surgery*, vol. 31, no. 4, pp. 238–243, 2003.

- [52] M. H. Bennett, R. Stanford, and R. Turner, "Hyperbaric oxygen therapy for promoting fracture healing and treating fracture non-union," *Cochrane Database of Systematic Reviews*, vol. 11, Article ID CD004712, 2005.
- [53] G. G. Walmsley, A. McArdle, R. Tevlin et al., "Nanotechnology in bone tissue engineering," *Nanomedicine*, vol. 11, no. 5, pp. 1253–1263, 2015.
- [54] M. Izadifar, A. Haddadi, X. Chen, and M. E. Kelly, "Rate-programming of nano-particulate delivery systems for smart bioactive scaffolds in tissue engineering," *Nanotechnology*, vol. 26, no. 1, Article ID 012001, 2015.
- [55] J. W. Lee and D.-W. Cho, "3D printing technology over a drug delivery for tissue engineering," *Current Pharmaceutical Design*, vol. 21, no. 12, pp. 1606–1617, 2015.
- [56] Y. Xu and X. Wang, "Application of 3D biomimetic models in drug delivery and regenerative medicine," *Current Pharmaceutical Design*, vol. 21, no. 12, pp. 1618–1626, 2015.